

PROTON FORM FACTOR RATIO MEASUREMENT WITH BLAST

BY

Adrian Tiberiu Sindile

M.S. in Computer Science, University of New Hampshire, 2005
Diploma of Eng. in Engineering Physics, Bucharest University, Romania, 1995
B.S. in Physics, Bucharest University, Romania, 1995

DISSERTATION

Submitted to the University of New Hampshire
in partial fulfillment of
the requirements for the degree of

Doctor of Philosophy

in

Physics

May 2006

This dissertation has been examined and approved.

Director, J. Calarco
Professor of Physics

W. Hersman
Professor of Physics

S. Beane
Assistant Professor

F. Lee
Research Scientist

R. Milner
Professor of Physics (MIT)

Date

Dedication

This work is dedicated to my parents who taught me how important education is.

Acknowledgments

If I had to name a single person who mattered (and matters) most to my career I would obviously name my wife Claudia, whose support was essential during the long years of graduate school. I really think we worked towards this Ph.D. degree together.

I want to thank my advisor Prof. John Calarco for giving me the opportunity to pursue interesting research while in graduate school. It would be really great if every graduate student could have an advisor as understanding and concerned about their students' career as John. I want to express my gratitude to Prof. Richard Milner, Director of MIT Bates for making this Lab a rewarding research place and for encouraging open discussions at all times in the BLAST collaboration. I am grateful to Tong Lee, who has been acting as my mentor since he became a Research Scientist at UNH - there are no words that can express what Tong's encouragement and help meant to me. Also, I am grateful to Prof. Bill Hersman, who recruited me for graduate studies at UNH and who made this whole experience possible. I would like to thank Prof. Silas Beane for his comments regarding my theory section (and for his patience while waiting to get a first draft of my thesis).

I would like to mention, in chronological order, all persons involved (at some point during my life) in my choosing physics as a career: Prof. Ion Enache from General School No. 3 Pitesti Romania, who really stirred my interest during middle school years and prepared me for my first National Olympics in Physics; Dr. Radu Vasile from the Nuclear Physics Institute Pitesti Romania, who during my high school years really showed me the way physicists think; Dr. Dumitru Dobrea, Dr. Csaba Roth, Dr. Ion Dumitrache and Dr. Victor Raica from the Nuclear Physics Institute Pitesti Romania, from whom I learned that studying never stops and that whatever one does should be done at the highest level.

I would like to mention Prof. Harvey Shepard from UNH whose QED course proved to be the most useful class I have ever taken, as far as this thesis is concerned.

Thanks to the entire MIT Bates Lab personnel, whose dedicated efforts in building, maintaining and running such a sophisticated detector as BLAST made this work possible. Tim Smith was undeniably the software guru of the BLAST project and he spent many hours with me in the early phases of the project, answering all my questions about the daunting tasks at hand. I learned a lot from Ed Six, as we were testing detectors in the Detector Testing Facility at Bates. Karen Dow showed me everything I needed to know about the data acquisition and spent numerous hours explaining the inner works of CODA. Jim Kelsey was probably the guy without whom the BLAST components would have never been put together. When Michael Kohl joined the BLAST project, I think everybody noticed things starting to work better - thanks Michael for always being not only the perfect professional, but also a friendly and approachable scientist. Manouch Farkhondeh was always on top of things related to the accelerator and his sense of humor and openness meant so much to all graduate students. I would like to also mention Hauke Kolster, who proved to be not only the expert we all needed on the ABS target, but also an approachable one - thanks Hauke, I was sad when you had to move on! Although Tancredi Botto left for a job in the oil industry towards the end of the project, I will not hold that against him: I know he has a very good heart and probably recycles too! I also want to mention Genya Tsentalovich, without whom we might have spent many more months troubleshooting the ABS - and I would have probably spent a few more weeks trying to find a software bug! Mentioning the Bates staff would not be complete without naming Ernie Ihloff, whose expertise could always be counted on, or Bill Franklin (the Compton polarimeter guru), Taylan Akdogan or Townsend Zwart. Doug Hasell was not only leading the wire chamber development effort, but was also the coordinator of the whole experiment for most of the running period.

Last but not least, I want to thank my fellow graduate students from UNH, MIT and

ASU for their part in making BLAST a succesful experiment. For more than five years I worked with Peter “Moose” Karpus, from building and testing scintillators to sharing tips on data analysis - Pete, you saved me at least a couple of months with your latex knowledge sharing! Thank you for always being there for me, I was fortunate to have you as my office mate! Tavi Filoti is the guy I started graduate school with and his being around meant a lot to me all these years.

I promised Jason Seely to have a special acknowledgement section just for him: I used his C++ form factor classes without shame and that saved me weeks of code-writing. I also have to admit I have no regrets about it. Jason, thanks for putting together the form factor database and thank you for being the great guy you are - I only regret being too busy and not getting together on a few occasions, especially when you and your wife made it to Durham to visit Pete... well, grad school is over now!

I want to thank Ben Classie for being the nicest shift co-worker and for enduring my questions about Australia - great things, mate! I want to thank Chris Crawford for no specific reason: if I start with the reasons, I will not be able to finish this, Chris is probably one of the few people who can do any task, and run an experiment like BLAST by himself. I want to thank Aaron Maschinot not only for his GEANT codes, but also for the documentation he wrote... have you considered writing a book? Thanks to Adam DeGrush for his wire chamber and high voltage control GUI, to Vitaliy Ziskin for his Mascarad implementation (I have to name only one thing now), to Nick Meitanis for his constant great attitude (man, we thought the same on so many issues regarding our projects!), to Yuan Xiao for the best green tea I had on a shift and to Eugene Geis for giving me a CD with eastern philosophy (sorry I lost it before listening to it, I am sure it was great!). If I left Chi Zhang at the end it is because this way nobody can say I chose a specific order - without Chi, BLAST Monte Carlo would probably be in terrible shape and the wire chamber reconstruction would be years behind. Thank you for writing the best C++ code and for providing the fastest support!

If I forgot anyone, I want to appologize right now - it was a pleasure to be part of the BLAST collaboration. This work has been supported by research grants from the U.S. Department of Energy.

Table of Contents

Dedication	iii
Acknowledgments	iv
ABSTRACT	xx
1 OVERVIEW AND MOTIVATION	1
1.1 Introduction	1
1.2 Existing Data	4
1.2.1 Unpolarized Data - Rosenbluth Separation	4
1.2.2 Polarized Data - Polarization Transfer	6
1.3 Phenomenological Fits	8
1.4 Two-photon Exchange Contributions	10
1.5 Current Experiment	12
2 THEORETICAL FRAMEWORK	14
2.1 Kinematics	14
2.2 Unpolarized Cross Section and Form Factors	15
2.3 Polarized Cross Section	18
2.4 Theoretical Calculations	20
2.4.1 Historical Review of the Proton Structure - the Parton Model	21
2.4.2 Perturbative QCD	22
2.4.3 Lattice QCD	23
2.4.4 Models	25

3	EXPERIMENTAL APPARATUS	31
3.1	The MIT-Bates Linear Accelerator	31
3.1.1	The Polarized Source	32
3.1.2	The Bates South Hall Ring	32
3.1.3	The Compton Polarimeter	34
3.2	Performance of the Electron Beam	35
3.2.1	Beam Current and Lifetime	35
3.2.2	Beam Polarization	37
3.3	The Polarized Internal Target	37
3.3.1	The Atomic Beam Source	38
3.3.2	Target Storage Cell and Scattering Chamber	39
3.4	Performance of the Polarized Target	40
3.4.1	ABS Intensity	40
3.4.2	RF Dissociation and Atomic Fraction	40
3.4.3	Target Polarization	42
3.5	The BLAST Detector	42
3.5.1	The BLAST Toroidal Field	44
3.5.2	Mapping the BLAST Magnetic Field	46
3.5.3	Time-of-Flight Scintillators	47
3.5.4	Time-of-Flight Scintillator Performance	49
3.5.5	Wire Chambers	55
3.5.6	Wire Chamber Performance	58
3.5.7	Čerenkov Detectors	59
3.5.8	Čerenkov Detector Performance	61
3.6	Data Acquisition System	63
3.6.1	BLAST Trigger	63
3.6.2	TDCs and ADCs	65

3.6.3	CODA Data Acquisition Software	67
3.6.4	The BLAST DAQ Performance	67
3.6.5	The BLAST MySQL Database	68
4	DATA ANALYSIS	71
4.1	Event Selection	72
4.1.1	Preliminary Cuts from Reconstruction	72
4.1.2	First Order Cuts	73
4.1.3	Second Order Cuts	80
4.2	Quality of the Data	88
4.3	BLAST Monte Carlo	92
5	RESULTS AND DISCUSSION	94
5.1	The Experimental Beam-Target Asymmetry	94
5.2	Super Ratio Method	96
5.3	Systematic Errors	101
5.3.1	Q^2 Determination	101
5.3.2	Target Spin Angle	103
5.3.3	Tracking	104
5.3.4	False Asymmetries	104
5.3.5	Background Measurement	107
5.3.6	Radiative Corrections	107
5.4	Results Discussion and Outlook	113
	LIST OF REFERENCES	119
	APPENDIX	123

List of Tables

3.1	Characteristics of the Linear Accelerator at MIT-Bates	33
3.2	LIGIT Pressure vs. Operating Mode	36
3.3	Target Polarization Summary - P_z represents vector polarization, P_{zz} represents tensor polarization (for the deuterium target)	42
3.4	Coil specifications	45
3.5	Properties of Bicron BC-408 Organic Plastic Scintillator	49
3.6	BLAST Drift Chamber Reconstruction Resolution	59
3.7	Čerenkov counter specifications	61
3.8	BLAST allows tagging the data with different trigger types. Typical 1st and 2nd level trigger rates are shown in the last column	64
4.1	Conditions for the three data-taking periods of BLAST with the ABS H_2 target	71
5.1	A_{ep} : $\theta_T = 47.1^\circ$, $P_b P_t = 0.52$, Charge = 294 kC	95
5.2	$\mu G_E^p / G_M^p$	100
5.3	The difference in the determination of Q^2 from the electron or proton polar angles for the left and right sectors of BLAST. The largest error is obtained for the second Q^2 point and is conservatively assigned to all other data points when calculating the total systematic errors. The last Q^2 point was only determined from the proton track information, as the BATs are outside wire chamber coverage	104

5.4	Single spin beam asymmetry A^{beam} : $\theta_T = 47.1^\circ$, $P_b P_t = 0.52$, Charge = 294 kC	105
5.5	Single spin target asymmetry A^{target} : $\theta_T = 47.1^\circ$, $P_b P_t = 0.52$, Charge = 294 kC	106
5.6	Unradiated Monte Carlo asymmetries A_{ep} : $\theta_T = 47^\circ$, $P_b P_t = 0.52$. 8M events were generated and reconstructed	111
5.7	Radiated Monte Carlo asymmetries A_{ep} : $\theta_T = 47^\circ$, $P_b P_t = 0.52$. 8M events were generated and reconstructed	111

List of Figures

1-1	Electric form factor - world unpolarized data	5
1-2	Magnetic form factor - world unpolarized data	6
1-3	Form factor ratio - world unpolarized data	7
1-4	Form factor ratio - world data	8
1-5	Form factor ratio - phenomenological fits to world data	9
1-6	Diagrams of e-p scattering amplitudes	11
2-1	Scattering plane conventions	18
2-2	Diagram of the Vector Meson Dominance amplitude	26
2-3	Vector Meson Dominance models and polarized data from Jefferson Lab for the proton form factor ratio $\frac{\mu G_E^p}{G_M^p}$ [1]	26
2-4	Dispersion theory models and polarized data from Jefferson Lab for the proton form factor ratio $\frac{\mu G_E^p}{G_M^p}$ [1]	27
2-5	Constituent quark models and polarized data from Jefferson Lab for the proton form factor ratio $\frac{\mu G_E^p}{G_M^p}$ [1]	29
3-1	Plan View of the MIT-Bates Linac	32
3-2	Beam Current and Lifetime	35
3-3	LIGIT Pressure vs Time	36
3-4	Typical Compton Polarimeter Beam Polarization Data	37
3-5	Hyperfine States of Hydrogen	38
3-6	The BLAST Atomic Beam Source	39
3-7	Hydrogen Atomic Fraction versus Flow Rate and Nozzle Temperature	41

3-8	The BLAST Detector	43
3-9	The scale of the BLAST Detector	43
3-10	The eight copper coils used to produce the toroidal field for BLAST	44
3-11	BLAST Field in 3-D	45
3-12	BLAST Field (downstream view)	46
3-13	BLAST Field Map vs Biot-Savart Calculations for B_y , 500 mm downstream of the target in the midplane	47
3-14	View of BLAST Right Sector TOF System	48
3-15	TOF Efficiency Measurement	50
3-16	TOF Efficiency. All TOFs performed with an efficiency greater than 99%	52
3-17	TOF Time Resolution	52
3-18	TOF Pedestal-Subtracted Gains	53
3-19	TOF Gains: The peak on the low end of the ADC spectrum is due to minimum ionizing electrons, the bump at higher ADC channel is due to protons	54
3-20	TOF Gain and Pedestals vs Run Number: The y-axis is the full scale ADC for the TOF PMTs. The x-axis is run number.	55
3-21	The drift chambers for BLAST are shown here in an overhead view with non-visible lines shown for display purposes	56
3-22	Light cone emitted by excitation of medium atoms when the speed of a charged particle exceeds that of light in the medium. The angle θ is given by equation 3.12	60
3-23	Side view of one of the individual Čerenkov counters used at BLAST within its mounting frame. Note the light box (blue) and the PMTs (yellow). Additional shielding installed to encase the PMTs is not shown here	61
3-24	Čerenkov Detector Efficiency Measurements	62
3-25	BLAST Trigger Electronics	66

3-26	Trigger for Retiming Analysis	68
3-27	Partial Diagram of the Initial BLAST MySQL Database	69
4-1	An application of the Newton-Rhapson method to track fitting.	74
4-2	Reconstructed electron and proton target vertex before any cuts were implemented. The triangular distribution is expected because of the variation of target density which is higher in the middle of the target chamber and lower towards the ends	75
4-3	BLAST angular acceptance distribution. Note most of the electrons scatter at low values of θ while protons scatter at high values of θ . BAT events cannot be seen in this picture, as the number of BAT events is very small compared to the total number of events	76
4-4	BLAST coplanarity of track trajectories	77
4-5	Reconstructed proton mass before any cuts were implemented. Note the big spike due to π^+ events that were later eliminated by cuts	78
4-6	Difference between reconstructed electron momentum and electron momentum calculated from elastic kinematic relations before any cuts were implemented. Inelastic events shown here with lower reconstructed momentum caused mostly by pions are later eliminated by elastic cuts	78
4-7	Invariant Mass	79
4-8	Difference of p_e and p_e calculated from θ_e . This differences was binned and fitted to a Gaussian in each bin, with a mean μ and RMS σ extracted for each bin. These μ and σ values were then fitted to polynomials in θ_e . Left (right) corresponds to electrons scattered in the left (right) and protons scattered in the right (left) sector of BLAST.	81

4-9	Difference of p_p and p_p calculated from θ_p . This difference was binned and fitted to a Gaussian in each bin, with a mean μ and RMS σ extracted for each bin. These μ and σ values were then fitted to polynomials in θ_p . Left (right) corresponds to electrons scattered in the left (right) and protons scattered in the right (left) sector of BLAST.	81
4-10	Difference of θ_p and θ_p calculated from θ_e . This difference was binned and fitted to a Gaussian in each bin, with a mean μ and RMS σ extracted for each bin. These μ and σ values were then fitted to polynomials in θ_e . Left (right) corresponds to electrons scattered in the left (right) and protons scattered in the right (left) sector of BLAST.	82
4-11	Difference of ϕ_p and ϕ_p calculated from ϕ_e . This difference was binned and fitted to a Gaussian in each bin, with a mean μ and RMS σ extracted for each bin. These μ and σ values were then fitted to polynomials in ϕ_e . Left (right) corresponds to electrons scattered in the left (right) and protons scattered in the right (left) sector of BLAST.	82
4-12	Difference z_p and z_e . This difference was binned and fitted to a Gaussian in each bin, with a mean μ and RMS σ extracted for each bin. These μ and σ values were then fitted to polynomials in z_e . Left (right) column of plots corresponds to electrons scattered in the left (right) and protons scattered in the right (left) sector of BLAST.	83
4-13	Example of BAT event information from the TOF and BAT detectors. ADC (first row), time-of-flight (second row) and position information (third row) for the right sector BATs is shown. The last row of plots shows time-of-flight information for the corresponding protons in the forward TOFs of the left sector	84
4-14	Difference of the proton and BAT electron time of flight on a detector pair-by-pair basis, before cuts were applied	85

4-15	Sum of the proton and BAT electron position on a detector pair-by-pair basis, before cuts were applied	86
4-16	Proton β before cuts for BAT events	87
4-17	Proton mass before cuts for BAT events	88
4-18	The measured polar angles θ_R vs. θ_L following implementation of elastic cuts	89
4-19	The measured polar angles θ_R vs. θ_L following implementation of elastic cuts. The red lines represent the proton polar angle as calculated from the electron polar angle $\theta_p(\theta_e)$ using the kinematics of elastic scattering	89
4-20	Difference between reconstructed electron momentum and electron momentum calculated from elastic kinematic relations after elastic cuts were implemented	90
4-21	Reconstructed Elastic Event TOP View	91
4-22	Reconstructed Elastic Event Upstream View	91
4-23	Total yield for each run, normalized by collected beam charge. The yield is plotted after all the elastic cuts were implemented	92
4-24	Comparison between the Monte Carlo TOF and BAT yields (black line) and the corresponding yields for real data. The left sector TOFs and BATs are illustrated by the blue dots, while the red dots depict the right sector TOF and BAT yields. All yields have been normalized to the integral of counts. Note the good agreement between the real data and the Monte Carlo shapes.	93
5-1	The experimental asymmetries measured for electrons scattering into the left and right sectors of BLAST. Each sector was fit to the Hoehler parametrization to extract the product of beam and target polarizations $P_b P_t$, which is consistent in the two sectors. Note the very good χ^2 values of the fit as well	96
5-2	The BLAST Frame	98

5-3	Rotating from the BLAST to Scattering Frame	99
5-4	Rotating from the Scattering Frame to the Q (Physics) Frame	99
5-5	$\frac{\mu_{G_E^p}}{G_M^p}$ as a function of Q^2 . The blue line is the Hoehler parametrization. The last data point was measured using the BATs and was outside of the wire chamber coverage	101
5-6	The difference in the determination of Q^2 from the electron or proton polar angles	102
5-7	Beam single spin asymmetries	105
5-8	Target single spin asymmetries	106
5-9	Comparison between yields as a function of Q^2 for the three cases of real data (black), unradiated Monte Carlo (blue) and radiated Monte Carlo (red)	108
5-10	Invariant mass W spectrum for the three cases of real data (black), unradiated Monte Carlo (blue) and radiated Monte Carlo (red). No cuts are applied here, so there are some inelastic events in the real data spectrum. No momentum corrections are applied to the real data either	108
5-11	Invariant mass W spectrum for the three cases of real data (black), unradiated Monte Carlo (blue) and radiated Monte Carlo (red). Simple acceptance and vertex cuts, as well as momentum corrections, were applied to the real data	109
5-12	Difference between p_e and p_e as calculated from θ_e before (blue) and after (red) momentum corrections	110
5-13	Difference between p_p and p_p as calculated from θ_p before (blue) and after (red) momentum corrections	110
5-14	Comparison between the unradiated Monte Carlo asymmetries (blue) and the radiated Monte Carlo asymmetries (red)	112
5-15	$(A_{radiativeMC} - A_{MC})/A_{MC}$	113

5-16	The BLAST results of $\frac{\mu_{G_E^p}}{G_M^p}$ with systematic errors. The curve is Hoehler's parametrization	114
5-17	The BLAST results of $\frac{\mu_{G_E^p}}{G_M^p}$. Also shown are the world's polarization transfer data and models that reproduce these higher Q^2 data obtained at JLab through the Focal Plane Polarimeter method	114
5-18	The BLAST results of G_E^n . The solid blue curve is Platchkov's fit, the dashed black and red curves are Friederich and Walcher's fit without and with BLAST data on G_E^n respectively	116

ABSTRACT

PROTON FORM FACTOR RATIO MEASUREMENT WITH BLAST

by

Adrian Tiberiu Sindile

University of New Hampshire, May, 2006

The proton electric to magnetic form factor ratio (G_E^P/G_M^P) is related to the underlying electromagnetic structure of the proton. G_E^P/G_M^P is studied through elastic scattering using a longitudinally polarized electron beam with 0.85 GeV energy, a polarized internal hydrogen gas target and the BLAST detector at the MIT Bates Lab. Beam-target spin asymmetries are measured in several bins of Q^2 for both left and right sector of BLAST, the super-ratio of these left/right asymmetries is formed and G_E^P/G_M^P is extracted.

CHAPTER 1

OVERVIEW AND MOTIVATION

1.1 Introduction

In the standard model, the electron is a point spin-1/2 particle that interacts electromagnetically by exchanging virtual photons, as described by Quantum Electrodynamics (QED). Because of the weak coupling constant of the photon ($\alpha \simeq 1/137$), the interaction amplitudes can be calculated by perturbation theory. As a result, QED is very well understood.

By contrast, the proton is 1836 times heavier than the electron and has internal structure. It can naively be described as being composed of three constituent quarks which interact by exchanging virtual gluons, as described by Quantum Chromodynamics (QCD). The coupling constant of gluons α_S varies with the momentum transfer squared Q^2 , so QCD can only be treated perturbatively in the high Q^2 (the so called *asymptotic freedom*) region. A detailed understanding of the nucleon, in general (proton, in particular) is essential in order to provide a stringent test of QCD in the non-perturbative region.

Electromagnetic probing of the atom, nucleus and nucleon has its roots in the early years of modern physics. By studying the scattering cross section through *electron scattering*, information about the structure of the target can be gathered. In particular, the structure of the proton can be studied this way. Since $\alpha \simeq 1/137$ is small, the interaction is dominated by the one-photon-exchange (OPE) amplitude - although it is now believed that two-photon effects are more important than initially thought.

Hofstadter used electron scattering [2] for the first time in 1955 to show that the cross-section for ep elastic scattering supported the idea that the proton had internal structure [3], which had already been shown in 1932 by the experiments of Frisch and Stern [4] measuring the anomalous magnetic moment of the proton.

The ep cross section can be parametrized by two structure functions in the OPE approximation. For the case of elastic scattering, these functions are the *electric and magnetic form factors* G_E and G_M , depending only on the momentum transfer squared Q^2 of the virtual photon.

For a naive picture of the form factors (treated in depth in the next chapter), consider the non-relativistic scattering of plane waves from an extended charge distribution $\rho(\mathbf{x}) = -\nabla^2\phi(\mathbf{x})$, where $\phi(\mathbf{x})$ is the electrostatic potential. The cross section is proportional to the square of the transition amplitude:

$$\langle \mathbf{k}' | \mathbf{H} | \mathbf{k} \rangle = \int d^3\mathbf{x} e^{-i(\mathbf{k}-\mathbf{k}')\cdot\mathbf{x}} \phi(\mathbf{x}) = \frac{\mathbf{F}(\mathbf{q}^2)}{\mathbf{q}^2} \quad (1.1)$$

where $\mathbf{q} = \mathbf{k} - \mathbf{k}'$ is the three-momentum transfer. The form factor

$$F(\mathbf{q}^2) = \int d^3\mathbf{x} e^{-i\mathbf{q}\cdot\mathbf{x}} \rho(\mathbf{x}) = 1 - \frac{1}{6}\langle r^2 \rangle \mathbf{q}^2 + \mathbf{O}(\mathbf{q}^4) + \dots \quad (1.2)$$

is the Fourier transform of $\rho(\mathbf{x})$ normalized such that $F(0) = \int d^3\mathbf{x} \rho(\mathbf{x}) = 1$. The root-mean-square (RMS) charge radius of the proton $r_p = \sqrt{\langle r^2 \rangle}$ is related to the slope of $F(q^2)$ at $q^2 = 0$ through the above Taylor expansion.

The proton has two independent form factors, G_E and G_M , representing the charge and magnetic distributions. G_E and G_M can be extracted from the unpolarized ep elastic cross section by varying the beam energy and electron scattering angle under the constraint of fixed Q^2 . Besides the fact that variation of the beam energy is difficult, the unpolarized ep elastic cross section is dominated by the electric contribution at low Q^2 , making difficult

the extraction of G_M , whereas at high Q^2 it is G_E that is difficult to extract due to the dominant magnetic part.

Relatively new advances in the technology of intense polarized beams and polarized targets have made possible a new generation of experiments relying on spin degrees of freedom. These experiments have increased sensitivity to small effects - for example, while the unpolarized ep elastic cross-section has terms proportional only to G_E^2 and G_M^2 , the polarized ep elastic cross-section has a term proportional to $G_E G_M$. This allows for a direct determination of the form factor ratio $\frac{G_E}{G_M}$. In addition, spin-dependent experiments rely on measurements of helicity and polarization asymmetries, which are independent of the cross section normalization, thus eliminating the effects of detector efficiency, acceptance and luminosity. By measuring ratios of the polarization observables, beam and target polarizations also cancel.

Relatively recent experiments performed at Jefferson Lab [5], [6] using the polarization transfer method deviated dramatically from the unpolarized data. This has renewed the interest in nucleon form factors, both theoretically and experimentally.

The first precision double polarization asymmetry measurement of the proton form factor ratio has been conducted in the South Hall Ring of the MIT-Bates Linear Accelerator Center. The purpose of this experiment was to map out the proton form factor ratio in the low- Q^2 region of the pion cloud. The experiment took advantage of unique features of the setup - intense polarized stored electron beam, an internal polarized gas target and the Bates Large Acceptance Spectrometer Toroid (BLAST) detector - to minimize systematic errors. As the sources of systematic errors are different from those of the polarization transfer measurements, this is an important cross check of the polarized data in the region where the two measurements overlap. The results of the BLAST experiment are presented in this thesis.

1.2 Existing Data

Unpolarized ep cross section measurements have been performed for decades and the individual $G_E(Q^2)$ and $G_M(Q^2)$ form factors have been extracted for a broad Q^2 range. In the last decade the form factor ratio $\left(\frac{G_E}{G_M}\right)$ has been extracted with higher precision in a series of experiments using spin degrees of freedom.

The results of the above mentioned methods are in clear disagreement. The remainder of this section describes these two methods and shows the existing results.

1.2.1 Unpolarized Data - Rosenbluth Separation

The unpolarized ep elastic cross section has the form (see appendix for a detailed discussion):

$$\left(\frac{d\bar{\sigma}}{d\Omega}\right)_{ep \rightarrow ep} = \left(\frac{d\bar{\sigma}}{d\Omega}\right)_{Mott} \left(\frac{G_E^2 + \tau G_M^2}{1 + \tau} + 2\tau G_M^2 \tan^2(\theta/2)\right) \quad (1.3)$$

where

$$\left(\frac{d\bar{\sigma}}{d\Omega}\right)_{Mott} = \frac{\alpha^2}{4E_i^2 \sin^4 \frac{\theta}{2}} \cdot \frac{\cos^2(\theta/2)}{1 + \frac{2E_i}{M} \sin^2(\theta/2)} \quad (1.4)$$

is the cross section given by a point-like spinless target, with α being the fine structure constant (1/137), E_i the initial electron energy, θ the scattering angle in the laboratory frame and $\tau = -q^2/4M_p^2 > 0$. In Mott's formula, $\cos^2(\theta/2)$ and $(1 + \frac{2E_i}{M} \sin^2(\theta/2))^{-1}$ arise from the spin-1/2 of the electron and the recoil of the target proton respectively.

The method of extracting $G_E(Q^2)$ and $G_M(Q^2)$ from the unpolarized ep elastic cross section is by a *Rosenbluth separation* [7]. Keeping Q^2 constant by varying the beam energy and electron angle, the unpolarized cross section is fit as a linear function of $\tan\left(\frac{\theta}{2}\right)$. The slope of the fit yields G_M and then the intercept of the fit yields G_E . The cross section is dominated by G_E at low Q^2 and by G_M at high Q^2 due to the kinematic factor $\tau = -q^2/4M^2$. This is reflected in unpolarized data.

The initial measurements of the form factors performed by Hofstadter at Stanford in the 1950's [3] confirmed the extended structure of the proton. The results were consistent with dipole form factors, corresponding to exponential charge and magnetic distributions. Subsequent Rosenbluth separations [8], [9], [10] of G_E and G_M confirmed the dipole form

$$G_E(Q^2) = \frac{1}{\mu} G_M(Q^2) = G_D(Q^2) \equiv \frac{1}{(1 + Q^2/\Lambda^2)^2} \quad (1.5)$$

where $\Lambda^2 = 0.71 \text{ (GeV/c)}^2$. Normally G_E and G_M are quoted in units of G_D .

A fundamental static property of the proton, besides its magnetic moment, is its RMS

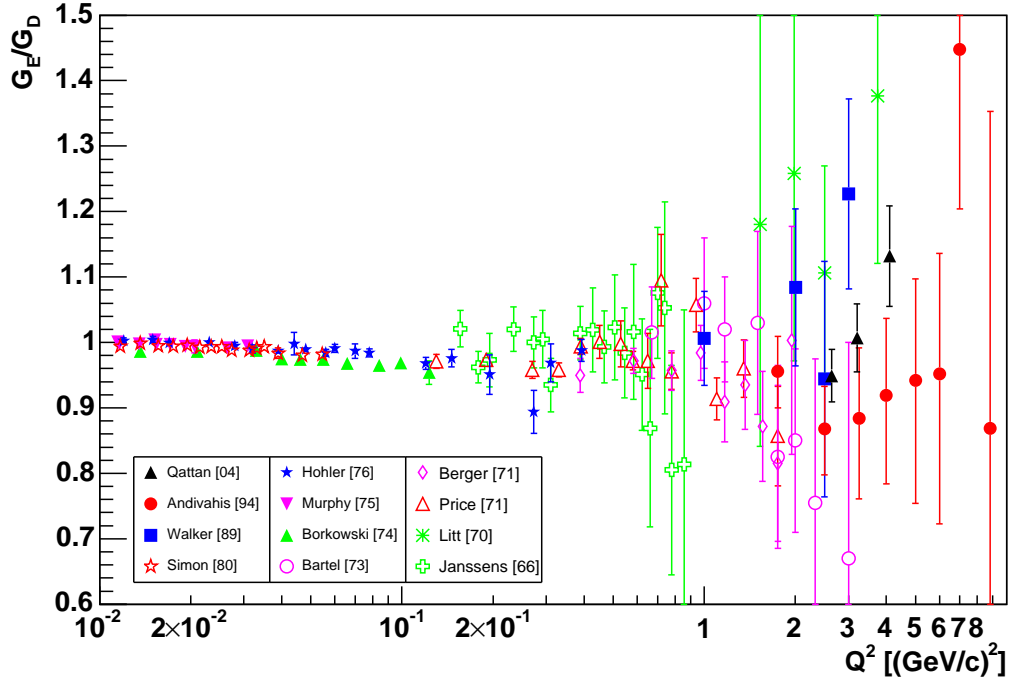


Figure 1-1: Electric form factor - world unpolarized data

charge radius r_p seen in equation 1.2. An early goal of ep elastic scattering experiments [11], [12], [13] was to measure r_p , by doing a Rosenbluth separation of G_E and G_M and

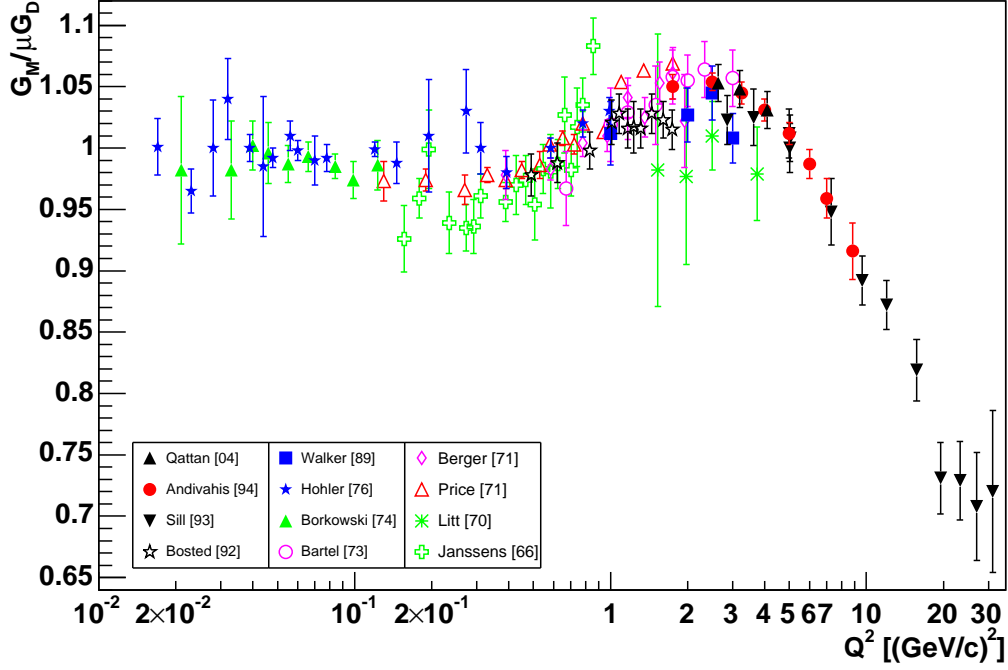


Figure 1-2: Magnetic form factor - world unpolarized data

fitting for the slope of G_E at $Q^2 = 0$ to get r_p . The results of these experiments were close to the currently accepted value of $r_p = 0.875$ fm.

The above mentioned data and other higher Q^2 [14], [15], [16], [17], [18], [19], [20] world unpolarized results for G_E and G_M are shown in Figures 1-1 and 1-2 respectively.

1.2.2 Polarized Data - Polarization Transfer

Recoil polarimetry measurements performed at Bates, Mainz and Jefferson Lab produced $\frac{\mu G_E}{G_M}$ (where μ is the magnetic moment of the proton) as extracted from the ratio of the transverse (P_t) to longitudinal (P_l) polarization of the recoil proton:

$$\frac{G_E}{G_M} = -\frac{P_t}{P_l} \frac{E_i + E_f}{2M} \tan\left(\frac{\theta}{2}\right). \quad (1.6)$$

The recoil proton polarization is measured by a secondary reaction with a carbon analyzer in the focal plane of the polarimeter.

The first extraction of $\frac{\mu G_E}{G_M}$ using a focal plane polarimeter (FPP) was done by Milbrath *et al.* at MIT-Bates [21] for two Q^2 points of 0.35 and 0.5 $(\text{GeV}/c)^2$. Popischil *et al.* followed up with an FPP experiment at Mainz [22] and measured $\frac{\mu G_E}{G_M}$ at $Q^2 = 0.37, 0.40$ and 0.44 $(\text{GeV}/c)^2$. Dietrich *et al.* [23] did an independent measurement at $Q^2 = 0.40$ $(\text{GeV}/c)^2$ using the same FPP as in the Popischil experiment. The results from these experiments agreed with the unpolarized data.

Higher Q^2 FPP measurements were performed at Jefferson Lab by Jones *et al.* [5] and

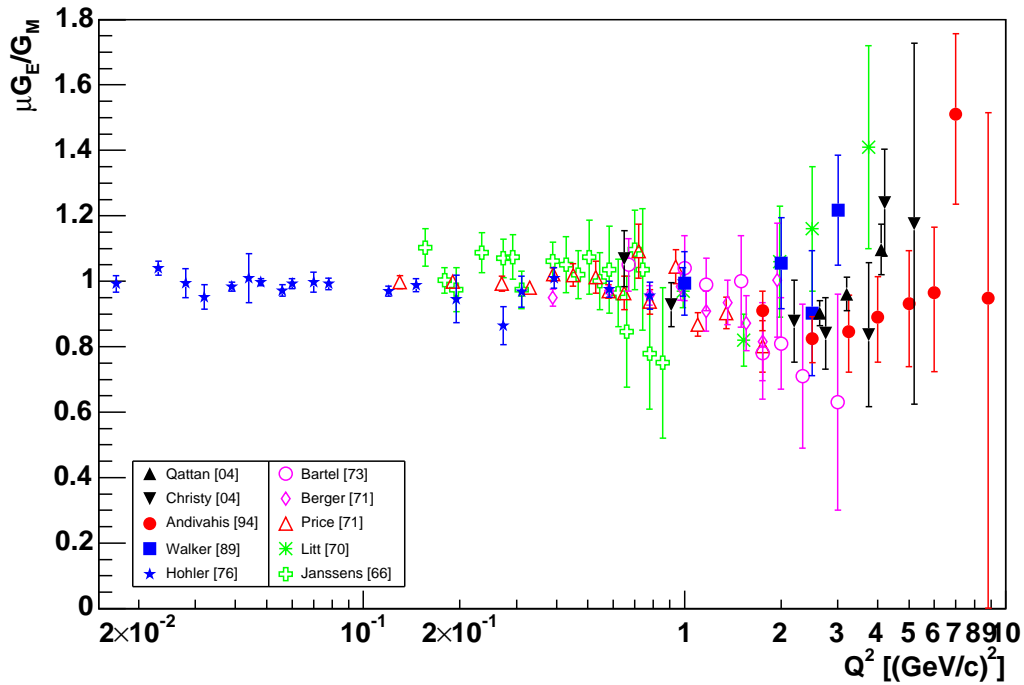


Figure 1-3: Form factor ratio - world unpolarized data

an unexpected drop in $\frac{\mu G_E}{G_M}$ down to 0.6 at $Q^2 = 3.5$ $(\text{GeV}/c)^2$ was observed. Gayou *et al.* extended the measurement to $Q^2 = 5.5$ $(\text{GeV}/c)^2$ [6] and observed the same downward

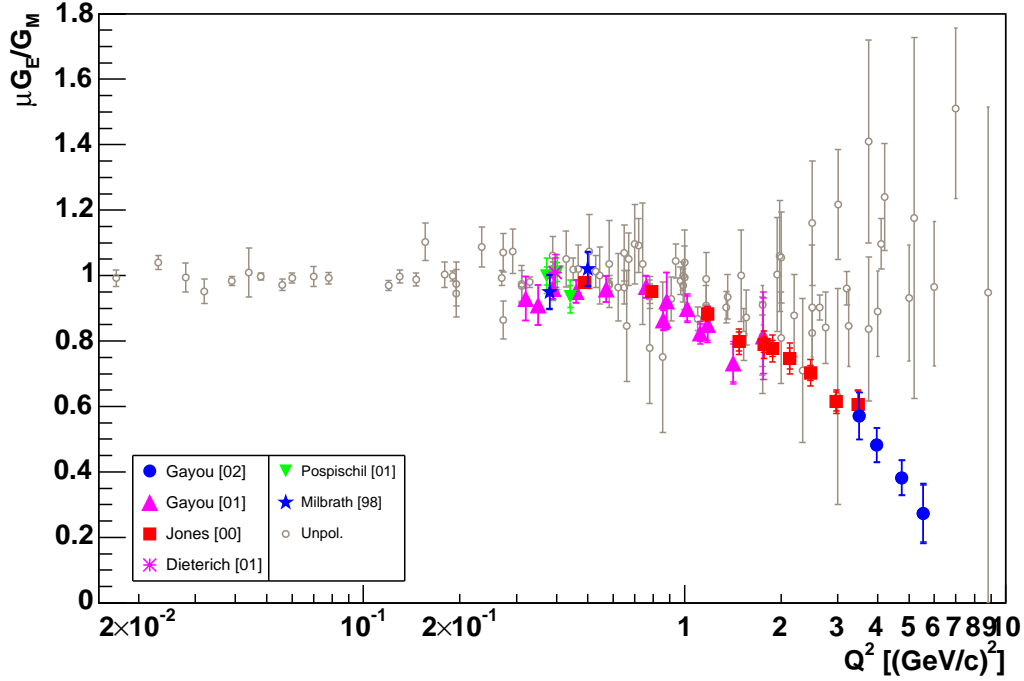


Figure 1-4: Form factor ratio - world data

trend: $\frac{\mu_{G_E}}{G_M}$ continued to decrease linearly down to 0.27 at $Q^2 = 5.5 \text{ (GeV/c)}^2$. Another approved experiment at Jefferson Lab will extend the range to $Q^2 = 9 \text{ (GeV/c)}^2$. The world unpolarized data for $\frac{\mu_{G_E}}{G_M}$ is shown in Figure 1-3. Figure 1-4 shows the world polarized data for $\frac{\mu_{G_E}}{G_M}$ on top of the unpolarized data.

1.3 Phenomenological Fits

Phenomenological fits to the world data have been performed over the decades. Here we present only the most recent ones, as these are the fits that have benefited from knowledge gathered over the years.

In 2003, motivated by the discrepancy between the unpolarized and polarized data, Arrington [24] reanalyzed the unpolarized cross section data, updating radiative corrections and splitting up data sets. He concluded that the unpolarized data set is self-consistent,

although incompatible with the polarized data.

In 2004, Arrington [25] refit the world data including recent Jefferson cross sections [26], [27] and low Q^2 data [11], [12], [13]. He presented a global fit to the world's cross section data and a combined extraction from polarization transfer and cross section data, explaining that the former provides a parametrization of the ep elastic cross section in the OPE approximation, while the latter provides the real form factors.

Also in 2004, Kelly [28] fit both polarized and unpolarized data to simple functions of Q^2 that are consistent with dimensional scaling at high Q^2 , are well behaved as $Q^2 \rightarrow 0$, and require only four parameters each for G_E and G_M .

In 2003, Friedrich and Walcher [29] came up with an ansatz motivated by a bump

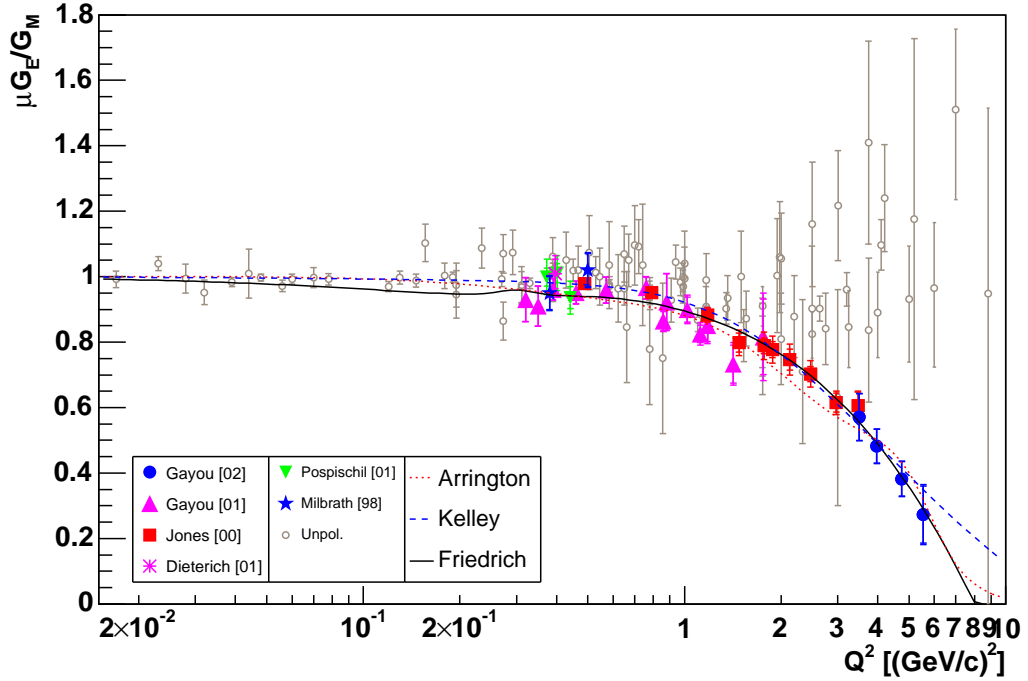


Figure 1-5: Form factor ratio - phenomenological fits to world data

structure at $Q^2 \simeq 0.2-0.3 (\text{GeV}/c)^2$ in the neutron electric form factor. Their model

parametrizes the smooth Q^2 dependence with a pair of dipoles and adds a Gaussian bump at low Q^2 , showing that not only G_E^n , but also G_E^p , G_M^p and G_M^n fit well to this ansatz. Friedrich and Walcher considered the bump to be caused by the nucleon's *pion cloud*, after noting that it has the effect of shifting charge to the outside of the nucleon, 2 fm away from the center of the nucleon. The fits of Arrington, Kelly and Friedrich and Walcher are shown in Figure 1-5, on top of both unpolarized and polarized $\frac{\mu G_E}{G_M}$ world data.

1.4 Two-photon Exchange Contributions

Unpolarized data from many experiments performed at laboratories around the world are consistent with each other. Also, polarization transfer measurements from three different laboratories agree at low Q^2 , while three different experiments performed at Jefferson Lab using different beam energies are also consistent.

So there is an important discrepancy between the form factor ratio $\mu \frac{G_E}{G_M}$ extracted from unpolarized data in the current Born OPE approximation and radiatively corrected within the framework of Mo and Tsai [30], and the extraction from polarization transfer data. Even if the polarization measurements are considered more precise, the ratio still needs to be combined with unpolarized cross sections to extract G_E and G_M individually. This is not reliable if the form factor contributions to the cross section are not understood [25].

The likely solution to the above mentioned discrepancy is the two-photon exchange contribution from the last two diagrams in Figure 1-6 (the first diagram is just the Born amplitude).

Guichon and Vanderhaegen [31] proved that although intrinsically small, of the order of a few percent of the cross section, this two-photon exchange correction is accidentally amplified in the case of the Rosenbluth method. Their analysis found the corrected form factor ratio close to the polarized data, while their correction did not destroy the linearity

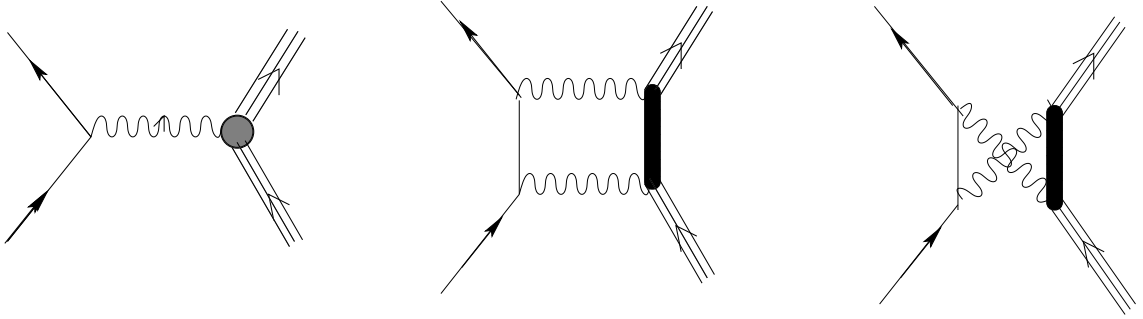


Figure 1-6: Diagrams of e-p scattering amplitudes

of the Rosenbluth plot.

Blunden, Melnitchouk and Tijon [32] evaluated two-photon exchange contributions in a simple hadronic model including the finite size of the proton (first model-dependent calculation of the two-photon effect). The corrections were found to be small in magnitude, but with a strong angular dependence at fixed Q^2 , proving significant for the Rosenbluth extraction at high Q^2 . Their calculation was able to explain about half of the discrepancy between the unpolarized and polarized data.

Chen et al. [33] estimated the two-photon exchange contribution at high Q^2 through the scattering off a parton in the proton. Relating the two-photon exchange amplitude to the generalized parton distributions they found that, using as input the polarization transfer determinations of the form factors, adding the two-photon exchange correction reproduces the Rosenbluth cross section. This work appears to resolve most of the discrepancy between the form factor ratio extracted from polarized and unpolarized data.

In summary, there have been recent attempts to calculate the effect of two-photon exchange. From the existing model-dependent calculations it is believed the discrepancy between polarized and unpolarized data for the form factor ratio is due to interferences between the two photon amplitudes and the Born amplitudes.

1.5 Current Experiment

With BLAST, we have measured double-spin asymmetries of the elastic $\vec{p}(\vec{e}, e'p)$ channel for a Q^2 between 0.15 and 0.85 (GeV/c)². These asymmetries have been used to extract the form factor ratio $\mu G_E^p/G_M^p$ from this reaction.

The purpose of this experiment was to map out the proton form factor ratio in the low- Q^2 region of the pion cloud. This region has not been experimentally verified in as much detail as the asymptotic freedom region of QCD, so high precision data will be very valuable in order to test various theoretical models (see next chapter for a presentation of some of the existing models), as well as *Lattice QCD* calculations in this non-perturbative region, once they are precise enough for comparison. The low energy region is also important for parity violating experiments [34], [35], [36], as proton form factors are used as input for them.

Considering the proton form factor ratio data available from both unpolarized and polarized experiments, the current measurement is an independent method for the extraction of $\mu G_E^p/G_M^p$ in a Q^2 region between the high precision proton charge RMS radius results obtained from unpolarized data and the results obtained from FPP data. As it can be seen in Figure 1-4, the data for Q^2 between 0.15 (GeV/c)² and 0.85 (GeV/c)² (which is the range covered by the current experiment) can surely be improved when compared to the bordering regions.

When taking into account the discrepancy between the unpolarized and FPP data, our measurement can provide an independent verification of the FPP method for the overlap region (although this region is not controversial from the point of view of the discrepancy between the two above methods). As both the FPP and the double-spin asymmetry methods measure the same observable, the fact that the systematic uncertainties are different provides an important cross-check.

Currently, there is a deferred proposal by Zheng, Calarco *et al.* [37] to measure

$\mu G_E^p/G_M^p$ from elastic $\vec{p}(\vec{e}, e'p)$ at JLab in Hall C. Just as FPP measurements were pioneered at MIT-Bates and then repeated at JLab, our experiment may prove useful for future comparison with polarized target experiments at JLab, where the Q^2 range can be extended. Such an extension would also be beneficial as it would allow a direct comparison between the FPP method and the double-polarization method at higher Q^2 .

CHAPTER 2

THEORETICAL FRAMEWORK

2.1 Kinematics

For elastic scattering of an electron with initial four momentum k_i and final four momentum k_f from a proton with initial four momentum P_i and final four momentum P_f , we assume that the target proton is at rest in the lab frame and we can write

$$P_i \rightarrow (M_p, \mathbf{0})$$

If we then define the three-momentum transfer \mathbf{q} and energy, ω , delivered to the target as

$$\mathbf{q} = \mathbf{k}_i - \mathbf{k}_f \tag{2.1}$$

$$\omega = E_i - E_f \tag{2.2}$$

then the four-momentum transfer is

$$q = (\omega, \mathbf{q}) \tag{2.3}$$

which is just the four-momentum of the transferred virtual photon. In the extreme relativistic limit (ERL) where $|\mathbf{k}_i| \gg m_{e^-}$, the four-momentum transfer for electron scattering

is

$$q^2 \simeq -4E_i E_f \sin^2\left(\frac{\theta}{2}\right) \quad (ERL) \quad (2.4)$$

where θ is the angle between \mathbf{k}_i and \mathbf{k}_f . Defining $Q^2 \equiv -q^2$, we have

$$Q^2 \simeq 4E_i E_f \sin^2\left(\frac{\theta}{2}\right) \quad (ERL) \quad (2.5)$$

In the case of elastic scattering, conservation of four-momentum yields

$$Q^2 = 2\omega M_p \quad (2.6)$$

From the above relations, we can now derive the scattered electron energy, E_f , as a function of electron scattering angle θ_e . We find

$$4E_i E_f \sin^2\left(\frac{\theta_e}{2}\right) = 2(E_i - E_f)M_p$$

which yields

$$E_f = \frac{E_i}{\left(1 + \frac{2E_i \sin^2(\theta_e/2)}{M_p}\right)} \quad (2.7)$$

Also in the extreme relativistic limit (ERL), the scattered proton angle can be expressed in terms of the scattered electron angle as

$$\theta_q = \tan^{-1}\left(\frac{E_f \sin(\theta_e)}{E_i - E_f \cos(\theta_e)}\right) \quad (2.8)$$

with E_f given above.

2.2 Unpolarized Cross Section and Form Factors

The squared spin-averaged transition matrix element that describes the transition from initial state i to final state f in the process of electron scattering off a proton is (see

appendix for a complete discussion):

$$|S_{fi}^-|^2 = \frac{1}{4} \sum_{spin} |\bar{u}(p_f, s_f) \gamma^\mu u(p_i, s_i) \frac{4\pi e e_p}{q^2} \bar{u}(P_f, S_f) \left[\gamma_\mu (F_1 + F_2) - \frac{1}{2M_p} (P_f + P_i)_\mu F_2 \right] u(P_i, S_i)|^2 \quad (2.9)$$

where $F_1(q^2), F_2(q^2)$ are unspecified real functions (“form factors”). $F_1(q^2)$ is the *Dirac form factor* and describes an extended spin-1/2 particle and $F_2(q^2)$ is the *Pauli form factor* and accounts for the anomalous magnetic moment of the proton associated with a spin flip. In the above formulae, $u(p_i, s_i)$ and $u(p_f, s_f)$ are the Dirac spinors and $\bar{u}(p_f, s_f) = u^\dagger(p_f, s_f) \gamma^0$ with γ^μ being the Dirac matrices.

The above can be rewritten as

$$|S_{fi}^-|^2 = \frac{e^2 e_p^2 (4\pi)^2}{(q^2)^2} L^{\mu\nu} H_{\mu\nu} \quad (2.10)$$

where $L^{\mu\nu}$ is the *lepton tensor* and $H_{\mu\nu}$ is the *hadron tensor*:

$$L^{\mu\nu} = \frac{1}{2} Tr \left(\frac{\not{p}_f + m_e}{2m_e} \gamma^\mu \frac{\not{p}_i + m_e}{2m_e} \gamma^\nu \right), \quad H_{\mu\nu} = \frac{1}{4M_p^2} \frac{1}{2} Tr K \quad (2.11)$$

where the K matrix is:

$$K = \left[(\not{P}^i + M_p) \left(\gamma_\mu (F_1 + F_2) - \frac{F_2}{2M_p} (P_\mu^f + P_\mu^i) \right) (\not{P}^f + M_p) \left(\gamma_\nu (F_1 + F_2) - \frac{F_2}{2M_p} (P_\nu^f + P_\nu^i) \right) \right] \quad (2.12)$$

with $\not{p} = \gamma^\mu p_\mu$ and $\not{P} = \gamma^\mu P_\mu$. Using the above leptonic and hadronic tensors, we obtain the spin-averaged cross section

$$\frac{d\bar{\sigma}}{d\Omega} = \frac{e^2 e_p^2}{4E_i^2 \sin^4(\frac{\theta}{2}) [1 + \frac{2E_i}{M_p} \sin^2(\frac{\theta}{2})]} \left[\left(F_1^2 - \frac{q^2}{4M_p^2} F_2^2 \right) \cos^2\left(\frac{\theta}{2}\right) - (F_1 + F_2)^2 \frac{q^2}{2M_p^2} \sin^2\left(\frac{\theta}{2}\right) \right] \quad (2.13)$$

The above result is known as *Rosenbluth's formula* [7]. If instead of the functions $F_1(q^2)$ and $F_2(q^2)$ we introduce the so-called electric and magnetic ‘‘Sachs form factors’’

$$G_E(q^2) = F_1(q^2) + \frac{q^2}{4M_p^2} F_2(q^2) \quad (2.14)$$

and

$$G_M(q^2) = F_1(q^2) + F_2(q^2) \quad (2.15)$$

then Rosenbluth's formula becomes

$$\left(\frac{d\bar{\sigma}}{d\Omega}\right)_{ep \rightarrow ep} = \left(\frac{d\bar{\sigma}}{d\Omega}\right)_{Mott} \left(\frac{G_E^2 + \tau G_M^2}{1 + \tau} + 2\tau G_M^2 \tan^2(\theta/2)\right) \quad (2.16)$$

where

$$\left(\frac{d\bar{\sigma}}{d\Omega}\right)_{Mott} = \frac{\alpha^2}{4E_i^2 \sin^4(\theta/2)} \cdot \frac{\cos^2(\theta/2)}{1 + \frac{2E_i}{M_p} \sin^2(\theta/2)} \quad (2.17)$$

is the cross section given by a point-like spinless target, with α being the fine structure constant (1/137), E_i the initial electron energy, θ the scattering angle in the laboratory frame and $\tau = -q^2/4M_p^2 > 0$. In Mott's formula, $\cos^2(\theta/2)$ and $(1 + \frac{2E_i}{M_p} \sin^2(\theta/2))^{-1}$ arise from the spin-1/2 of the electron and the recoil of the target proton respectively.

The measured Q^2 -dependence of the form factors gives us information about the radial charge and magnetic distributions. The limiting case $Q^2 \rightarrow 0$ is particularly important. In this case G_E is the electric charge of the target normalized to the elementary charge e and G_M is the magnetic moment μ of the target, normalized to the nuclear magneton. The limiting values are:

$$G_E^p(Q^2 = 0) = 1 \quad (2.18)$$

$$G_M^p(Q^2 = 0) \simeq 2.79 \quad (2.19)$$

2.3 Polarized Cross Section

In summarizing the formalism of the polarized cross section, we adopt the following conventions for the scattering plane and the reaction plane shown in Figure 2-1. The angles

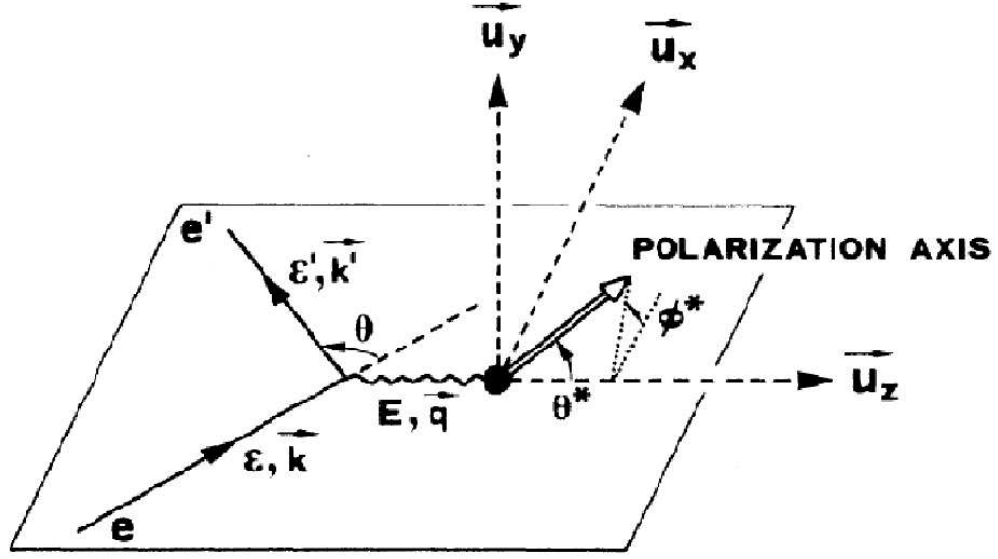


Figure 2-1: Scattering plane conventions

θ^* and ϕ^* are defined as the polar and azimuthal angles between the target polarization vector and the direction of the three-momentum transfer \mathbf{q} .

Following Donnelly and Raskin [38], Rosenbluth's formula can be written in a slightly different form as

$$\frac{d\bar{\sigma}}{d\Omega} = \left(\frac{d\bar{\sigma}}{d\Omega}\right)_{Mott} \left[(1 + \tau)v_L G_E^2 + 2\tau v_T G_M^2 \right] \quad (2.20)$$

The recoil factor is included in the above Mott formula and v_T and v_L are kinematic factors defined as follows:

$$v_L = \frac{Q^4}{|\mathbf{q}|^4} \quad (2.21)$$

$$v_T = \frac{1}{2} \frac{Q^2}{|\mathbf{q}|^2} + \tan^2\left(\frac{\theta}{2}\right) \quad (2.22)$$

In the one-photon-exchange (OPE) Born-approximation the cross section for the scattering of longitudinally polarized electrons from a polarized proton target can be written quite generally as

$$\frac{d\sigma}{d\Omega}(P_b, P_z) = \Sigma + h\Delta \quad (2.23)$$

where P_b is the polarization of the incident electron beam and P_z is the vector polarization of the target. The first term Σ is the unpolarized differential cross section given by Rosenbluth's formula, h is the electron helicity and Δ is the spin-dependent differential cross section given by

$$\Delta = -\left(\frac{d\bar{\sigma}}{d\Omega}\right)_{Mott} \left[2\tau v_{T'} \cos\theta^* G_M^2 - 2\sqrt{2\tau(1+\tau)} v_{TL'} \sin\theta^* \cos\phi^* G_M G_E \right] \quad (2.24)$$

where $v_{T'}$ and $v_{TL'}$ are kinematic factors defined as

$$v_{T'} = \tan\left(\frac{\theta}{2}\right) \sqrt{\frac{Q^2}{|\mathbf{q}|^2} + \tan^2\left(\frac{\theta}{2}\right)} \quad (2.25)$$

$$v_{TL'} = -\frac{1}{\sqrt{2}} \frac{Q^2}{|\mathbf{q}|^2} \tan\left(\frac{\theta}{2}\right) \quad (2.26)$$

From the polarized ep cross section formula we can define the beam-target asymmetry

$$A \equiv \frac{\Delta}{\Sigma} = -\frac{2\tau v_{T'} \cos\theta^* G_M^2 - 2\sqrt{2\tau(1+\tau)} v_{TL'} \sin\theta^* \cos\phi^* G_M G_E}{(1+\tau) v_L G_E^2 + 2\tau v_T G_M^2} \quad (2.27)$$

The experimental asymmetry A_{exp} is related to the above spin-dependent asymmetry by the relation

$$A_{exp} = P_b P_z A \quad (2.28)$$

where P_b and P_z are the beam and target vector polarizations, respectively. Reversing the electron helicity (or the target spin) reverses the sign of the beam (or target) polarization and permits an experimental determination of A_{exp} and hence of A . A determination of the ratio $\frac{G_E^p}{G_M^p}$, independent of the knowledge of the beam and target polarizations, can be precisely obtained by measuring the super ratio

$$R = \frac{A_1}{A_2} = \frac{2\tau v_{T'} \cos\theta_1^* G_M^2 - 2\sqrt{2\tau(1+\tau)} v_{TL'} \sin\theta_1^* \cos\phi_1^* G_M G_E}{2\tau v_{T'} \cos\theta_2^* G_M^2 - 2\sqrt{2\tau(1+\tau)} v_{TL'} \sin\theta_2^* \cos\phi_2^* G_M G_E} \quad (2.29)$$

where A_1 and A_2 are elastic ep scattering asymmetries measured simultaneously at fixed value of Q^2 and at two proton spin orientations corresponding to (θ_1^*, ϕ_1^*) and (θ_2^*, ϕ_2^*) respectively.

For a symmetric detector as in the case of BLAST, A_1 and A_2 can be measured simultaneously by forming two independent beam-target asymmetries in the left and right sectors of the detector, respectively.

2.4 Theoretical Calculations

At the same time with experimental progress towards the goal of measuring the proton form factor ratio with high precision, different theoretical methods for calculating it, and the nucleon electromagnetic structure in general, have been developed. The relatively recent Generalized Parton Distributions (GPDs) [39], [40] connect the nucleon form factors and nucleon structure functions probed in deep inelastic scattering experiments. QCD is the theory of strong interaction and it has been well tested in the high energy (i.e. perturbative) region. Unfortunately, QCD cannot be solved analytically in the non-perturbative regime. Lattice QCD has shown much promise due to both new computer hardware and new algorithms and QCD effective theories also tackle the low energy region. Between the perturbative regime and the low energy range, different phenomenological or QCD-based models exist [1]. The rest of this section gives a quick (mainly historical) review of our

knowledge of the proton structure in terms of *quarks* (and describes the *Parton Model* in the process) and then discusses the various theoretical calculations predicting the proton form factor ratio.

2.4.1 Historical Review of the Proton Structure - the Parton Model

In deep inelastic scattering, two structure functions similar to the form factors F_1 and F_2 (with the difference that now they depend not only on Q^2 , but also on a second parameter like the inelasticity of the process $x = \frac{Q^2}{2M_p\omega}$) are used. Measurements of these structure functions showed that F_2 was almost independent of Q^2 , while the ratio $\left(\frac{2xF_1}{F_2}\right)$ was constant [41]. These results are consistent with a proton made up of point-like particles with spin 1/2 (this can be seen when compared with the cross section obtained in the case of a Dirac, i.e. structureless, proton - see appendix) and they confirmed the partonic structure of the nucleon and the existence of quarks.

The *Parton Model* introduced by Feynman [42] and Bjorken [43] looks at the proton in a fast moving system, so that the transverse momenta and the rest masses of the proton constituents can be neglected. The structure of the proton is thus given in a first approximation by the longitudinal momenta of its constituents. In the *impulse approximation* (in which only one parton takes part in the interaction, while the others are spectators) and considering that $Q^2 \gg M^2$, we obtain a direct interpretation of the inelasticity $x = \frac{Q^2}{2\omega M_p}$ as the fraction of the four-momentum of the proton which is carried by the struck parton [44].

Since nucleons are spin-1/2 particles made up of quarks and quarks are also spin-1/2 particles, it follows that nucleons are built up out of at least three quarks (otherwise spin would not add up). From the fact that the maximum positive charge found in hadrons is two (e.g. Δ^{++}) and the maximum negative charge is one (e.g. Δ^-) the charges of these hadrons are attributed to three u quarks (charge $2e/3$) and three d quarks (charge $-e/3$) respectively. The proton is made up of two u quarks and one d quark, while the neutron

is made up of two d quarks and one u quark, for a total charge of e and 0 respectively.

Besides the three quarks that determine the quantum numbers of the nucleons (called *valence quarks*) virtual quark-antiquark pairs (called *sea quarks*) also exist in the nucleon. However, they carry only very small fractions x of the nucleon's momentum. While s , c , t and b quarks also exist, for the currently attainable Q^2 regions only s quarks can be observed regularly in the nucleon's *sea* due to the large masses of the c , t and b quarks.

The above assumption regarding quark charges was later proven by comparison of the structure functions observed in deep inelastic scattering with charged leptons and with neutrinos:

$$F_2^{e,N}(x) = x \sum_f z_f^2 (q_f(x) + \bar{q}_f(x)) \quad (2.30)$$

$$F_2^{\nu,N}(x) = x \sum_f (q_f(x) + \bar{q}_f(x)) \quad (2.31)$$

where the above structure functions in the parton model are written in terms of the distribution functions of the quark momenta q_f ($q_f(x)dx$ is the expectation value of the number of quarks of type f in the hadron whose momentum fraction x lies within $[x, x + dx]$), weighted by x and the square of the quark charge z_f (the charge enters the cross section formula quadratically). In the above formulae, \bar{q}_f is the momentum of the corresponding antiquark.

Combining the results from the scattering of charged leptons and neutrinos, one also obtains information about the momentum distribution of sea quarks and valence quarks. Integrating over all quark momenta, it is found that roughly half of the nucleon momentum is carried by particles that do not interact electromagnetically or weakly (*gluons*).

2.4.2 Perturbative QCD

Gluons, the field quanta of the strong interaction, can couple to other gluons (they carry *color charge*, unlike the field quanta of QED - the photons - that do not carry charge

and so do not couple to each other). A first order calculation in *Perturbative QCD* yields for the coupling constant of gluons:

$$\alpha_s(Q^2) = \frac{12\pi}{(33 - 2n_f)\ln(Q^2/\Lambda^2)}. \quad (2.32)$$

Here, n_f denotes the number of quark types involved. Since a heavy quark-antiquark pair has a very short lifetime and range, it can be resolved only at very high Q^2 . So n_f (and subsequently α_s) depends on Q^2 . Λ is the only free parameter of QCD and it is determined to be $\Lambda \approx 250$ MeV/c. The perturbative approach is valid in QCD only for $Q^2 \gg \Lambda^2$. In the limit $Q^2 \rightarrow \infty$, quarks can be considered to be “free”; this is called *asymptotic freedom*. By contrast, at low Q^2 , it is impossible to detach individual quarks from hadrons (*confinement*).

Perturbative QCD predicts well the unpolarized data behavior for $\mu G_E^p/G_M^p$ [45], [46], [47] at very high Q^2 , with the Dirac (F_1) and Pauli (F_2) form factors following the scaling law:

$$F_1 \sim (Q^2)^{-2}, F_2 \sim \frac{F_1}{Q^2} \quad (2.33)$$

resulting in $\mu G_E^p/G_M^p = \text{const.}$

Instead of scaling as $\frac{F_2}{F_1} \sim \frac{1}{Q^2}$, the polarized data appears to scale as $\frac{F_2}{F_1} \sim \frac{1}{Q}$. It is believed that taking into account the angular momentum of the quarks L_z explains this behavior [47], [48]. Another possible explanation would be that the Q^2 for the existing polarized data is too low for perturbative QCD calculations in this region.

2.4.3 Lattice QCD

At low momentum transfer, i.e. large distances, QCD cannot be treated analytically due to its non-perturbative nature. *Lattice QCD* promises to calculate numerically the form factors from the QCD Lagrangian with no effective theories or models. Most of the

lattice results obtained so far were carried out in the so called *quenched approximation* in which sea quark contributions are suppressed. As of now, limitations in computing power lead to approximations like the discrete space-time lattice spacing a that must be extrapolated to the continuum limit $a \rightarrow 0$ or the extrapolation to infinite volume that needs to be done since current computing power does not permit large enough lattices to fully contain the pion cloud. Furthermore, the lattice calculations are only practical using large quark masses because of limitations of the current computer power. As in the immediate future complete lattice QCD calculations seem unlikely, the challenge is to find an accurate way of extrapolating the lattice results to the physical quark mass. The linear extrapolation in quark mass gives erroneous results, so model-dependent extrapolations are needed.

Matevosyan et al. [49] explored the possibility of extrapolating the QCD calculations to the physical regime using the *Light Front Cloudy Bag Model* and letting its parameters be analytic functions of the quark mass. These functions were also used to define extrapolations to the physical value of the pion mass, predicting that $\mu G_E^p/G_M^p$ crosses 0 around $Q^2 = 6 \text{ (GeV/c)}^2$.

Ashley et al. [50] proposed a relatively simple approach to the extrapolation of lattice QCD data for the nucleon electromagnetic form factors, by parametrizing the data from the QCDSF collaboration by a simple dipole form, with the dipole mass parameter taken to be a function of the pion mass. They report very good agreement of this empirical model with the proton form factors.

Dunne et al. [51] incorporated the model independent constraints of chiral symmetry, extrapolating the lattice result on the proton RMS charge radius to the physical pion mass.

Rapid progress has been made in the use of sophisticated extrapolation techniques and in computing power. Lattice calculations with smaller and smaller quark masses are constantly underway and will be tested with precision form factor measurements in the low

Q^2 region as they appear.

2.4.4 Models

Besides perturbative QCD which predicts the nucleon form factors (and the behavior of the proton form factor ratio $\frac{\mu G_E^p}{G_M^p}$ in particular) at very large momentum transfer, and lattice QCD which tries to solve the same problem numerically, there are various models treating the electromagnetic structure of the nucleon. However, many of these models are limited by the degrees of freedom they consider, for reasons easy to understand: while an electromagnetic probe at high Q^2 is very likely to address the quark degrees of freedom, in the low Q^2 range it is very likely to probe only the pion cloud. Thus some of the models we present are by design only applicable in a limited energy range.

In our discussion below we try to consider the models that more closely reproduce the polarized data behavior of the proton form factor ratio, which is the approach Gao [1] took when providing a comprehensive review of the nucleon electromagnetic form factors. Also, in our discussion we try to emphasize the low Q^2 region relevant to the current experiment.

Vector Meson Dominance Models

In *Vector Meson Dominance Models* the nuclear structure is described by the exchange of vector mesons, as shown in Figure 2-2. In these models the form factors are approximated by a sum of terms:

$$F(Q^2) = C + \sum_i \frac{C_{\gamma V_i}}{Q^2 + M_{V_i}^2} F_{V_i N}(Q^2) \quad (2.34)$$

where C is chosen to satisfy the normalization at $F(0)$. $F_{V_i N}(Q^2)$ is a simple form factor (usually monopole or dipole) of the bare nucleon (a Dirac particle), and $C_{\gamma V_i}$ is the coupling strength of the virtual photon to a vector meson of mass M_{V_i} .

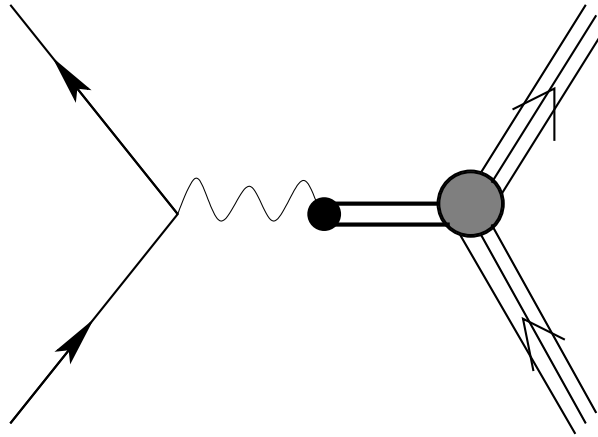


Figure 2-2: Diagram of the Vector Meson Dominance amplitude

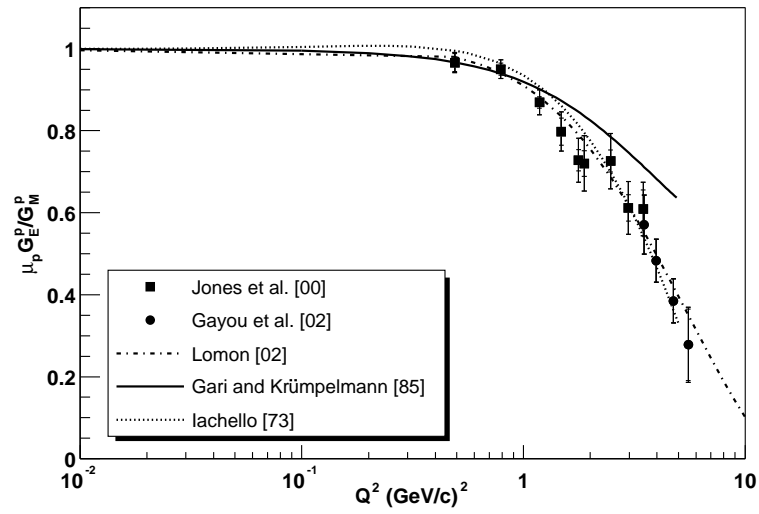


Figure 2-3: Vector Meson Dominance models and polarized data from Jefferson Lab for the proton form factor ratio $\frac{\mu_p G_E^p}{G_M^p}$ [1]

Iachello *et al.* [52] attempted to describe the proton form factors with a VMD model. Gari and Krümpelmann [53] extended the VMD model to include quark dynamics at large Q^2 via perturbative QCD. Lomon [54] extended the Gari and Krümpelmann model by including the width of the ρ meson and higher mass vector meson exchanges. He further enhanced his model [55] to include the $\omega'(1419)$ vector meson in order to describe the polarized data from Jefferson Lab. Figure 2-3 [1] shows the above VMD models on top of the polarized data for $\frac{\mu G_E^p}{G_M^p}$.

Dispersion Theory Models

Höhler *et al.* [56] fit a dispersion ansatz to e - N scattering data. VMD contributions from ρ , ω , ϕ , ρ' and ω' were included. This model was enhanced by Mergell *et al.* [57], accounting for ρ - ω mixing. Hammer *et al.* [58] did a dispersion fit including the available

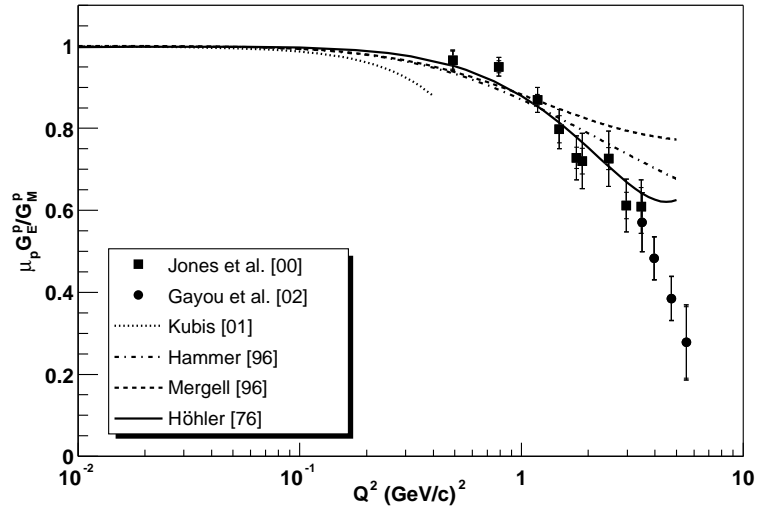


Figure 2-4: Dispersion theory models and polarized data from Jefferson Lab for the proton form factor ratio $\frac{\mu G_E^p}{G_M^p}$ [1]

data on the form factors in the time-like ($Q^2 < 0$) region [59]. Kubis *et al.* [60] used

the accepted proton RMS charge radius of 0.86 fm as a constraint. Kubis' results show a clear departure from the JLab data, decreasing too rapidly as Q^2 increases. Figure 2-4 [1] shows the above dispersion relation models on top of the polarized data for $\frac{\mu G_E^p}{G_M^p}$.

At low Q^2 , with the exceptions of Höhler [56] and Mergell [57] these models are phenomenological fits to the form factors with physical functions and constraints, so comparison with new experimental data have limited meaning.

Constituent Quark Models

As Q^2 increases and the electron starts probing individual partons, there must be models that describe the mechanism to redistribute the momentum among the rest of the nucleon in the case of elastic scattering. *Constituent Quark Models* approximate QCD by combining the gluonic and sea quark degrees of freedom with the valence quarks and treating the nucleon as being composed of just valence quarks, with enlarged masses but unchanged quantum numbers. These “effective valence quarks” are called *constituent quarks*.

Realistic *Constituent Quark Models* must include relativistic effects. There are three classes of Hamiltonian quantum dynamics introduced by Dirac [61]: the instant form, light-front form, and point form, corresponding to particle states being defined on a space-like hyperplane at fixed time, on a tangent to the light cone, or on a Lorentz-invariant hypersurface, respectively.

The *MIT Bag Model* which has three valence quarks confined to a finite spherical well was extended by Lu and Thomas [62] who included a pion cloud in the model and thus reproduced well the low Q^2 behavior of the form factors.

Following an earlier work by Frank, Jennings and Miller [63], Miller [64] recently used light front dynamics modeling the nucleon as a relativistic system of three bound constituent quarks surrounded by a pion cloud, in effect applying the relativistic dynamics of the quarks to the pion cloud of the Cloudy Bag Model to create the so-called *Light*

Front Cloudy Bag Model. His model reproduces the perturbative QCD scaling $\frac{F_2}{F_1} \sim \frac{1}{Q}$ at high Q^2 , while the pion cloud is important for understanding the nucleon structure at low momentum transfer.

Cardarelli *et al.* [65] also did calculations in light front dynamics with a one-gluon exchange potential. Their model also predicted well G_E and G_M for the polarized data.

Ma *et al.* [66] did calculations of a quark-diquark model in light front dynamics while Wagenbrunn *et al.* [67] constructed a model in point form dynamics. Their models are in good agreement with the FPP data from Jefferson Lab.

Li [68] used a relativistic quark model in which symmetry is required in the center-of-mass frame. This has the effect of adding additional terms to the baryon wave function. Taken together with the original terms, these represent the inclusion of the sea quarks. His model preceded the FPP JLab experiments and gives good agreement with the data.

Holzwarth [69] used a soliton model with mesonic degrees of freedom. His results

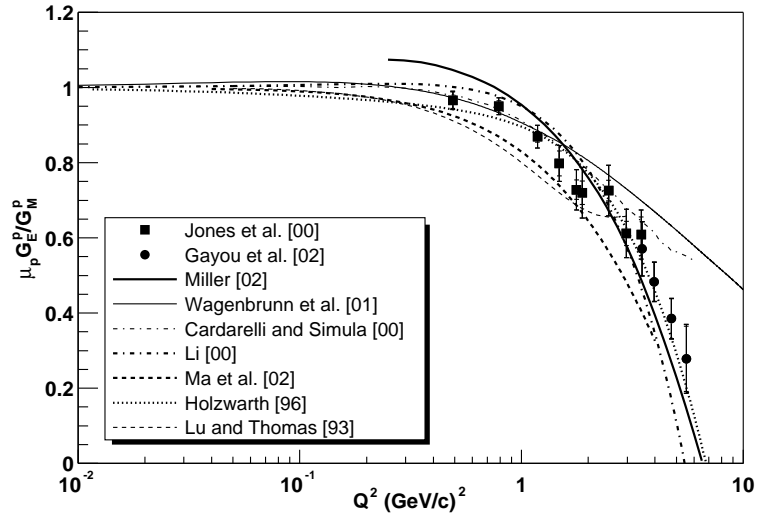


Figure 2-5: Constituent quark models and polarized data from Jefferson Lab for the proton form factor ratio $\frac{\mu_p G_E^p}{G_M^p}$ [1]

agree very well with the Jefferson Lab data. Figure 2-5 [1] shows the above constituent quark models on top of the polarized data for $\frac{\mu G_E^p}{G_M^p}$.

CHAPTER 3

EXPERIMENTAL APPARATUS

The measurement of $\mu G_E^p/G_M^p$ was performed at the William F. Bates Linear Accelerator Center in Middleton, Massachusetts. This facility is funded by the U.S. Department of Energy and operated by the Massachusetts Institute of Technology. The main components of the experiment (polarized beam, polarized target and the detector package) and their performance are described in this chapter.

3.1 The MIT-Bates Linear Accelerator

The MIT-Bates Linear Accelerator delivered a longitudinally polarized electron beam to the BLAST detector. A klystron gallery supplied RF power to resonant cavities which were used to accelerate the low energy polarized electrons up to an energy of 500 MeV and the energy of the beam was increased up to ~ 1 GeV by making a second pass through a recirculator; at this point a switchyard guided the beam to the Bates South Hall Ring (SHR). The beam used for the BLAST experiment had an energy of 850.0 ± 0.8 MeV, as calibrated from a precise field-map of the integrated magnetic field along the dipoles in the ring. The BLAST detector was located in the South Experimental Hall to take advantage of the facility's storage ring. Here the beam would interact with the polarized internal target and particles produced by scattering would then be detected by the BLAST spectrometer.

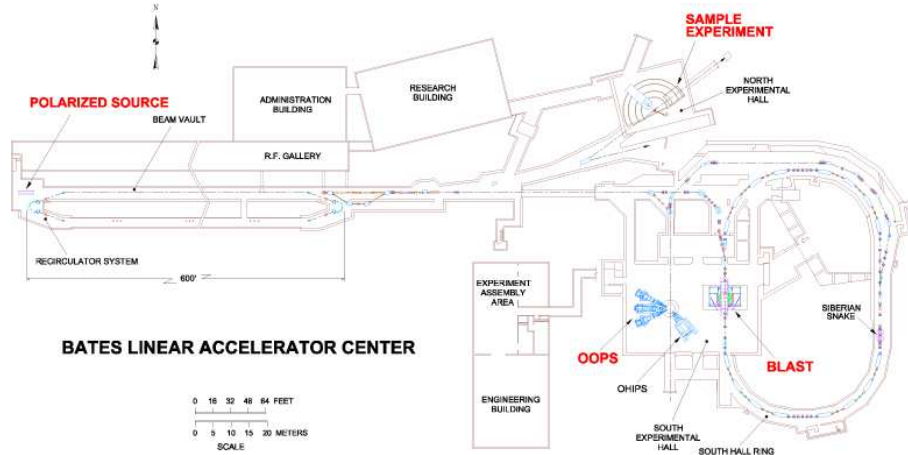


Figure 3-1: Plan View of the MIT-Bates Linac

3.1.1 The Polarized Source

The Bates polarized electron source consists of a gallium arsenide (GaAs) crystal illuminated by circularly polarized laser light which excites the valence electrons to the conduction band. The work function of the GaAs is decreased by building a surface dipole with Cesium. The laser beam is passed through a linear polarizer and a $\lambda/4$ waveplate before being focused on the photo-cathode. The emitted photoelectrons must have their spins polarized in order to satisfy conservation of angular momentum. These electrons, which have an energy of approximately 0.36 MeV [70], are fed into the linac for acceleration to the proper energy of the experiment. The source was able to inject 6 mA into the accelerator. The beam helicity is reversed by the mechanical insertion of a $\lambda/2$ waveplate into the beam.

3.1.2 The Bates South Hall Ring

The BLAST spectrometer and polarized target were installed into the west section of the Bates South Hall Ring. The Bates SHR is designed to operate either in pulse stretcher mode for external targets or as a storage ring for internal targets [70]. The SHR was built with two elongated linear sections and a circumference of 190m. It is equipped with 16

dipole magnets for beam steering and an RF cavity operated at 2.865 GHz. For BLAST, the SHR was operated in its storage mode, in which a long-lifetime continuous wave beam is achieved through gradual stacking of electron pulses from the accelerator. Injected pulses have a peak current of 2mA and are injected with frequency of 20-30Hz for about 20-30 seconds depending on the desired peak current. The beam then circulates in the ring for a period of time until the current falls below a threshold set to optimize beam delivered to the experiment. The current is measured by a parametric current transformer (DCCT) which operates essentially as a pickup coil.

Total Length	190m
Number of Klystrons	12
Number of transmitters	6
RF Pulse Length	0-25 μ s
Accelerator frequency	2.865 GHz
Recirculated Beam Energy MAX	1.06 GeV
Max Beam Duty Cycle	1%
Max Pulse Repetition Rate	1kHz

Table 3.1: Characteristics of the Linear Accelerator at MIT-Bates

In order to prevent de-polarization of the longitudinally polarized beam by spin precession due to the g-2 anomaly [71] after injection in the ring, a *Siberian Snake* system was used. The system is designed to rotate the spin of each electron traversing it by 180 degrees around the snake axis, thus reversing any perturbations due to precession or other processes. By the time electrons circle back to the target, the Snakes orient the spins such that they precess to the desired direction upon reaching the BLAST target. The Siberian Snake system is located in the east section of the South Hall Ring.

VME scaler readbacks from the BLAST wire chambers provide diagnostics of the beam tune. Also, four Beam Quality Monitors (BQMs) were installed to monitor the beam halo. The BQMs are plastic scintillators previously used as beam halo monitors for the SAMPLE

experiment. They were mounted to the beam pipe upstream of the target, gain-matched with a standard source, and connected to readout electronics through RG-58 cables [72].

Four beam blocks (or *slits*) made of 1 cm thick Tungsten material, were installed upstream of the target in order to limit the amount of stray electrons hitting the detectors due to multiple scattering and Coulomb scattering in the beam-pipe. Positioning of the slits depends on the tune of the injection and is established empirically during operation, moving them in to the point of reducing the lifetime of the beam at which point they are withdrawn by 1 mm, cutting away electrons outside of a 6σ beam distribution. The slow controls system Experimental Physics and Industrial Control System (EPICS) provides the means of user interface and controls for much of the beam hardware and diagnostics.

3.1.3 The Compton Polarimeter

The well understood *Compton effect* was used to monitor the polarization of the beam during running. Within the QED framework, the scattering cross-section of polarized photons off polarized electrons depends on the polarization of the electron beam as well as the polarization of the incident laser light [72]. Specifically, by reversing the helicity of the laser with a Pockels Cell, an asymmetry can be measured that describes the intensity of the backscattered photons. This asymmetry is directly proportional to the product of the laser and electron beam polarization. In order to implement this, a Compton polarimeter was placed upstream of the BLAST target area in order to minimize background due to bremsstrahlung radiation. The system consisted of a 5 Watt solid state laser of 532 nm wavelength, an optical transport system, adjustable mirrors and a CsI calorimeter. The laser beam intercepted the electron beam and the backscattered photons were detected by a calibrated calorimeter. A dedicated data acquisition system collected the data and integrated the results with the BLAST data stream. A beam chopper allows for a measurement of background while sweeper magnets ensure that no charged particles reach the calorimeter [72]. Average beam polarization as measured with the Compton Polarimeter

has been $\sim 65\%$.

3.2 Performance of the Electron Beam

3.2.1 Beam Current and Lifetime

Once the ring is filled, the current begins to drop as the beam interacts with the target. This is the dominant effect in limiting the beam lifetime [71]. Collisions with residual gas in the ring can cause the electrons in the beam to be scattered outside of the ring acceptance. Ring electrons can ionize the residual gas and trap these ions in their electrostatic field [71]. This *ion trapping* creates a density of ions in the beam that is the source of the beam halo. A chart from the EPICS system shown in Figure 3-2 displays typical current and lifetime behaviour.

In order to have a good beam lifetime, the halo must be minimized so maintaining a

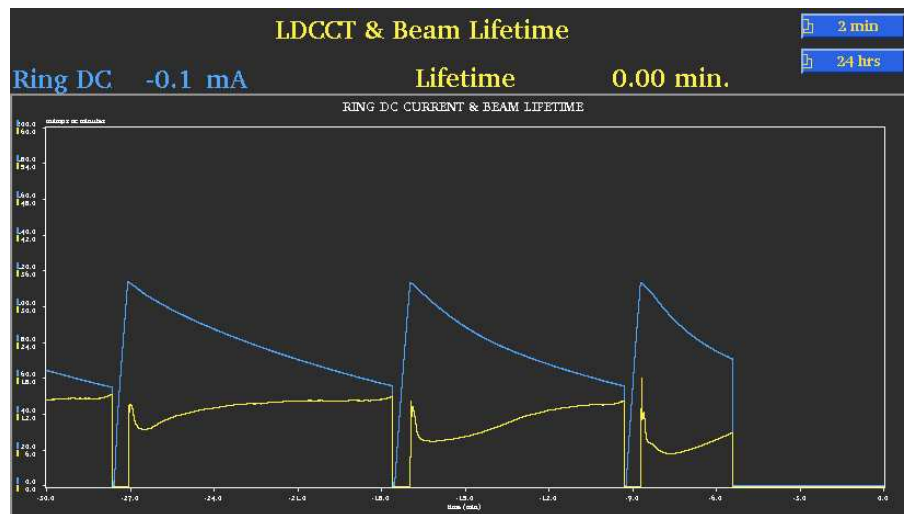


Figure 3-2: Beam Current and Lifetime

good ring vacuum was very important. Table 3.2 summarizes typical pressure in the target region for different operating modes. These pressures were measured by the Lattice Ion

Target Mode	Beam Mode	LIGIT Pressure (Torr)
<i>H</i> ABS	stored	8.8E-08
<i>H</i> ABS	injection	1.2E-07
Empty	stored	8.8E-08
Empty	injection	1.2E-07

Table 3.2: LIGIT Pressure vs. Operating Mode

Gauge Internal Target (LIGIT) located in the region of the scattering chamber. Note the slight increase in LIGIT pressures during injection shown in Figure 3-3 from the EPICS system.

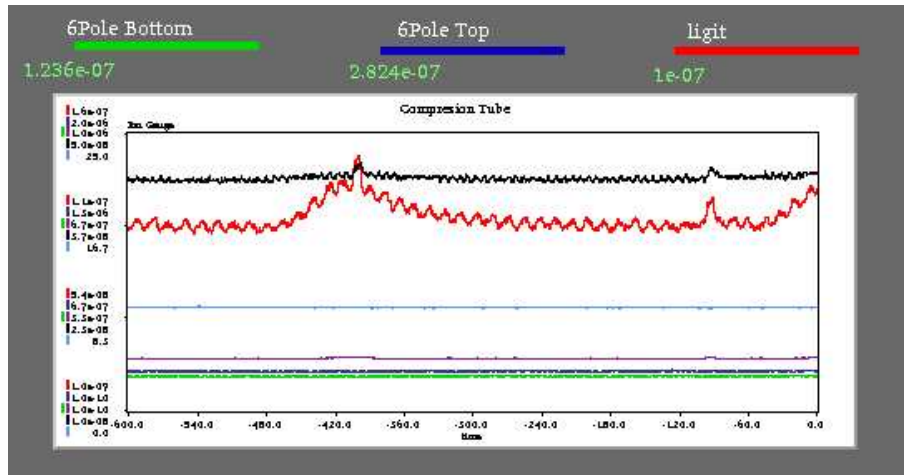


Figure 3-3: LIGIT Pressure vs Time

Injection currents as high as 200 mA with lifetimes on the order of 25 minutes have been achieved with an energy of 850 MeV for the hydrogen internal target thickness required by the experiment.

3.2.2 Beam Polarization

The Compton Polarimeter provided a real time measurement of the beam polarization near the target position. An asymmetry of the backscattered photons from the Compton laser was measured once per fill and beam polarization was found to be 0.6558 ± 0.0007 (stat), ± 0.04 (sys). False asymmetries were also measured to illustrate the effect of background and were found to be less than 4% [73]. This was taken into account in the extraction of the polarization. Typical polarimeter data are shown in Figure 3-4.

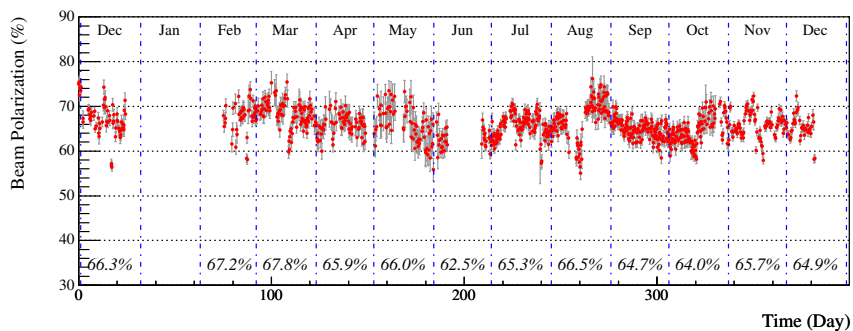


Figure 3-4: Typical Compton Polarimeter Beam Polarization Data

3.3 The Polarized Internal Target

The polarized internal target system at Bates was based on an atomic beam source (ABS) design. The ABS was originally built and employed at NIKHEF and it was moved to Bates after the electron accelerator at NIKHEF was closed. Most of the components were replaced or redesigned to allow the ABS to operate in the large magnetic field of BLAST. The ABS provided an intense polarized atomic beam to a storage cell through which the circulating electrons of the Bates South Hall Ring passed.

3.3.1 The Atomic Beam Source

Molecular hydrogen is dissociated via an RF dissociator. The resulting atomic beam is filtered in the desired spin states through a series of sextupole magnets and RF units by capitalizing on the Zeeman effect [74]. The hyperfine states of hydrogen are shown in Figure 3-5. The BLAST ABS has essentially five stages and is shown schematically

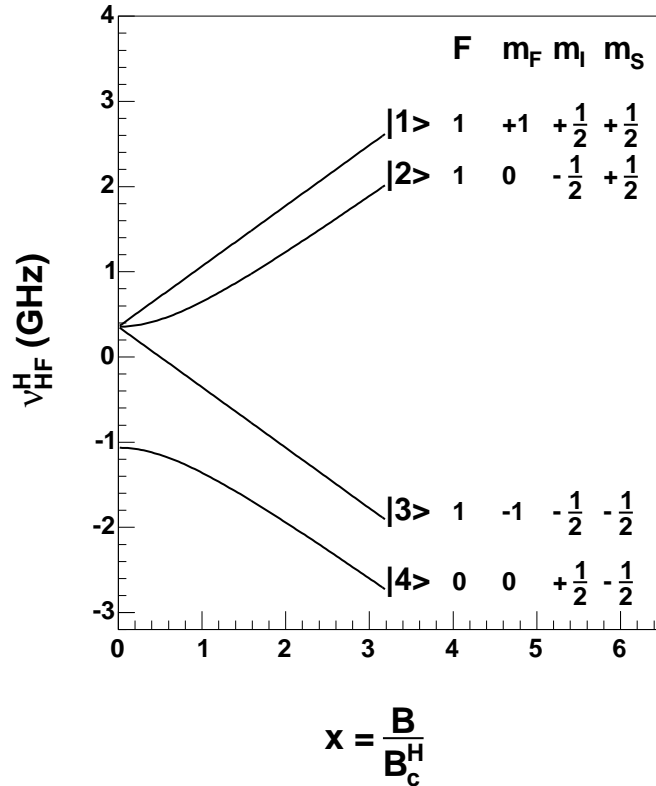


Figure 3-5: Hyperfine States of Hydrogen

in Figure 3-6. After molecular hydrogen is dissociated by the RF field of the dissociator chamber, a cryogenic nozzle forms the atomic beam which is further collimated by a skimmer. The second stage of the ABS contains the first set of sextupole magnets which perform Stern-Gerlach separation of the hyperfine states ($m_s = \pm 1/2$) [74]. In the third

stage, a mean field transition (MFT) flips one of the two hyperfine states left after the sextupole magnets and the fourth stage, which contains the second set of sextupole magnets as well as strong field transition (SFT) and weak field transition (WFT) units, finally selects the required spin state. Only the MFT and WFT were used to polarize hydrogen, while the SFT, MFT and WFT were all used for the BLAST deuterium experiments. In the fifth stage of the ABS, further pumping reduces background in the target cell.

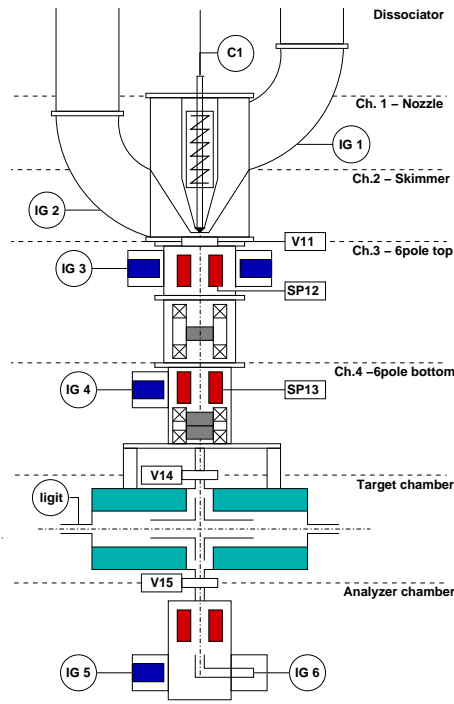


Figure 3-6: The BLAST Atomic Beam Source

3.3.2 Target Storage Cell and Scattering Chamber

The polarized atomic beam is injected into a cylindrical storage cell, effectively increasing the target thickness. The cell temperature is kept around 100 K. Two storage cells were used during the experiment - a 40 cm storage cell was used for the commissioning period,

while the production data were taken with a 60 cm storage cell. A magnetic holding field with longitudinal and transverse components that have magnitudes from 0-50 mT and 0-25 mT respectively was created by longitudinal and transverse coils located above and below the scattering chamber. The holding field defines the orientation of the target spin. In this experiment, the target vector was set to 47° for most of the data taking but some data were also collected for a target spin angle of 32° beam-left in the BLAST xz-plane (parallel to the South Hall floor), mostly for consistency checks regarding the deuterium experiments.

Many factors can influence polarization of the target. Spin exchange reactions through collisions with the cell walls are the main reason for reduced target polarization.

3.4 Performance of the Polarized Target

3.4.1 ABS Intensity

The ABS intensity is defined as

$$I(Q) = I_0 \cdot Q \cdot e^{-Q/Q_0} \quad (3.1)$$

where Q is the flow into the dissociator, I_0 is the intensity in the absence of rest gas scattering, and Q_0 is a factor parameterizing the beam attenuation due to rest gas scattering. An average hydrogen ABS intensity of $\simeq 2.6 \times 10^{16}$ [atoms/sec] was achieved during the course of the experiment. This intensity corresponds to a target thickness of $\simeq 4.5 \times 10^{13}$ [atoms/cm²] [75].

3.4.2 RF Dissociation and Atomic Fraction

The *figure of merit* of the dissociator is given by the population of selected atomic species versus total population in the target. The *atomic fraction* α quantifies this degree

of dissociation as

$$\alpha = \frac{P^a}{P^a + 2\kappa_\nu P^m} \quad (3.2)$$

where P^a and P^m are the partial pressures of the atomic and molecular gases in the target respectively [75]. The factor $\kappa_\nu \simeq 1/\sqrt{2}$ accounts for the different atomic and molecular velocities.

Figure 3-7 shows the dependence of hydrogen atomic fraction on RF power for different flow rates in the dissociator and nozzle temperatures. As the flow rate increases, the atomic

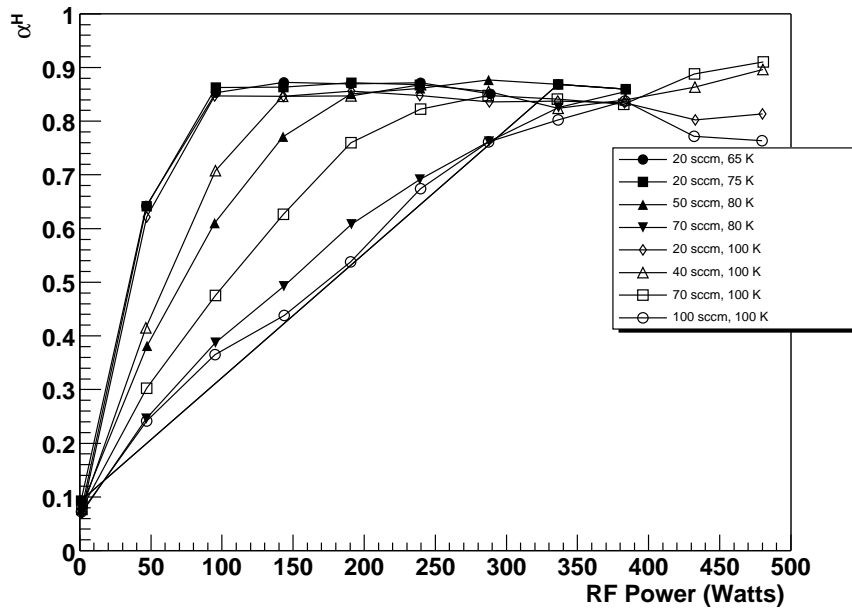


Figure 3-7: Hydrogen Atomic Fraction versus Flow Rate and Nozzle Temperature

fraction decreases - so more RF power is required to obtain the same level of dissociation [75].

Target	Reaction	P_z	P_{zz}
Hydrogen	p(e,e'p)	$80 \pm 4\%$	n/a
Deuterium	d(e,e'p)n, d(e,e'd)	$86 \pm 4\%$	$68 \pm 6\%$

Table 3.3: Target Polarization Summary - P_z represents vector polarization, P_{zz} represents tensor polarization (for the deuterium target)

3.4.3 Target Polarization

Table 3.3 presents the polarizations obtained with the ABS system during the running of both hydrogen and deuterium BLAST experiments. A more in-depth discussion of the hydrogen target polarization is presented in the analysis chapter.

3.5 The BLAST Detector

The Bates Large Acceptance Spectrometer Toroid (BLAST) detector allows the measurement of observables over a broad kinematic range in order to achieve its design goal which is the measurement of double polarization asymmetries. The azimuthal symmetry and two-sector configuration allow for coincidence and super-ratio measurements while its large acceptance makes up for the low luminosity of the internal gas target. The entire detector package consists of individual detector arrays designed and instrumented according to the experiment's requirements of timing resolution, momentum and tracking resolutions as well as particle identification. BLAST has an eight sector copper coil array which produces a toroidal magnetic field, and the two opposing wedge-shaped sectors have wire chambers, scintillation detectors, Čerenkov counters, and neutron detectors.[71]. Although the neutron detectors were not used for the hydrogen target experiments, they are mentioned here for completeness. The BLAST spectrometer and its scale are shown in Figure 3-8 and Figure 3-9.

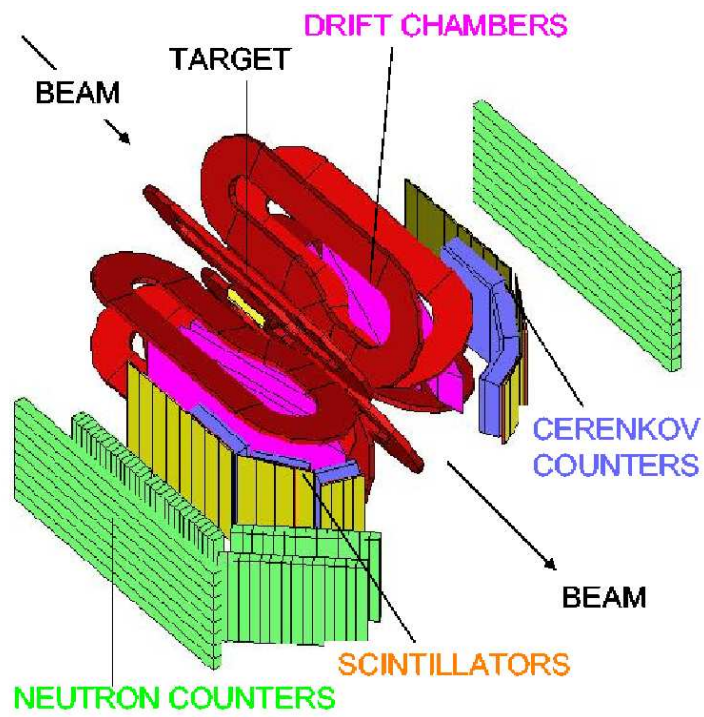


Figure 3-8: The BLAST Detector

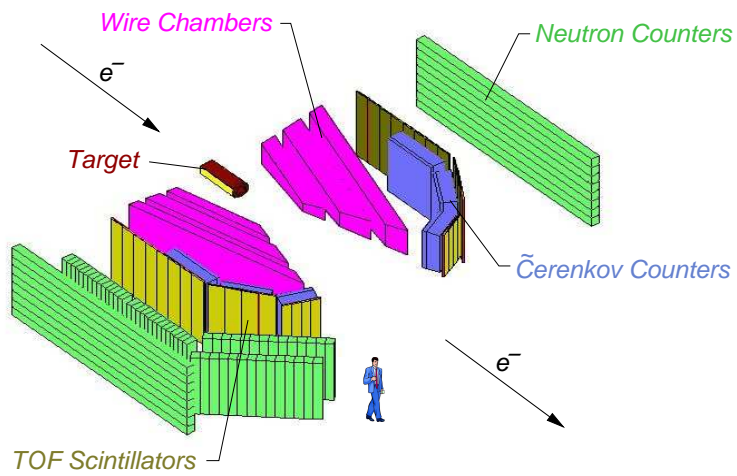


Figure 3-9: The scale of the BLAST Detector

3.5.1 The BLAST Toroidal Field

The toroidal magnetic field used to produce particle tracks was obtained with the 8-coil configuration shown in Figure 3-10. The coils were manufactured by Everson Electric and were integrated with BLAST by mounting them on an aluminum subframe. This allowed for azimuthal symmetry and the installation of the Atomic Beam Source, the drift chambers and other components. Each of the eight coils consisted of 26 turns of cable wrapped around a hollow copper conductor filled with water coolant. A dual-passage water flow system with a nominal velocity of 7.7 ft/sec was used for cooling. Electrical, leakage, insulation and acceptance tests were performed prior to operation. Power to the coils was provided by a BTSPS MON 1 250/7000 C5 power supply from BRUKER, which was installed on the South Hall floor near the BLAST detector and shielded from direct radiation with cement blocks. The maximum current of the supply was 7000A at 250V.

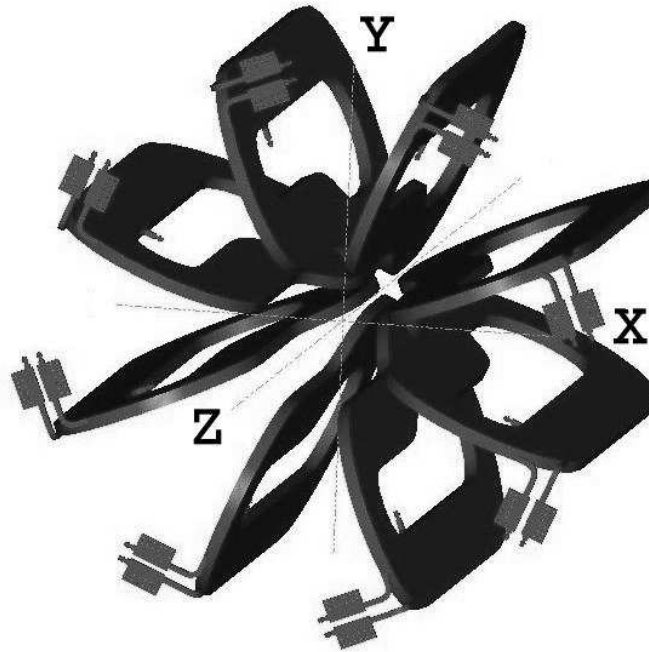


Figure 3-10: The eight copper coils used to produce the toroidal field for BLAST

Number of turns	26
Current per conductor	6730.77A
Area of conductor	1.742in ²
Mean turn length	357.6in
Current Density	3864 A/in ²
Water velocity	7.7ft/sec
Weight of single coil	2380Kg

Table 3.4: Coil specifications

The eight coils arranged symmetrically about the electron beam axis provided a toroidal magnetic field that varied as $B(r) = B_i r_i / r$ where r_i is the inner radius of the torus. A field-free target region was needed so that the target holding field and incident electron beam were not affected. Operating current was calculated to be 6730A for which the coils provided 0.38T maximum field strength. $\int \mathbf{B} \cdot d\ell$ values between 0.2 and 0.6 T-m as well as field gradients less than 0.05 G/cm in the target ± 15 cm region [71] were achieved. Plots of the azimuthal field B_ϕ versus radial and axial distance from the target are shown in Figure 3-11 and Figure 3-12.

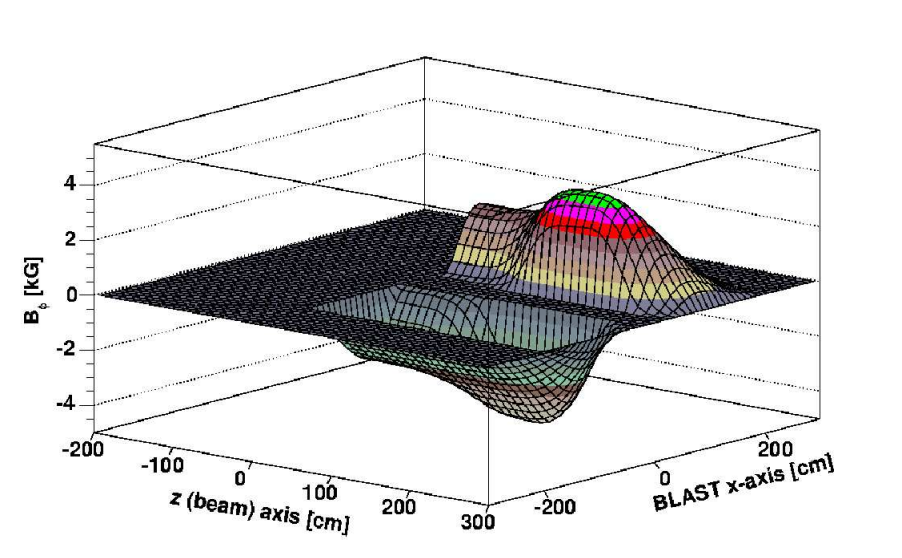


Figure 3-11: BLAST Field in 3-D

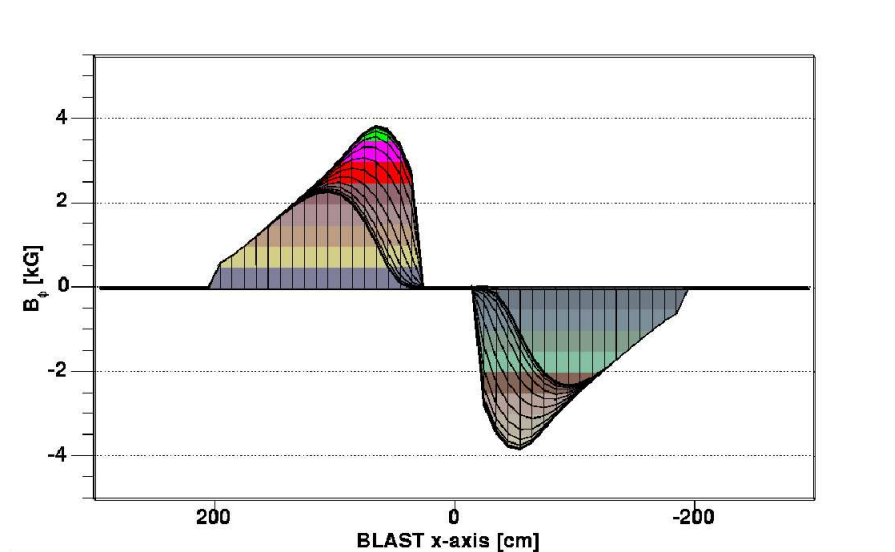


Figure 3-12: BLAST Field (downstream view)

3.5.2 Mapping the BLAST Magnetic Field

The toroidal field was mapped with an EPICS controlled coordinate table with resolution of 0.5mm and two 3-dimensional Hall probes before the beginning of the running. The location of the table was determined by surveying at each new measurement position. The results of the mapping were in good agreement with analytic Biot-Savart calculations as well as TOSCA simulations. The reproducibility of the field and the stability of the configuration were tested by powering the coils to full power. While the subframe remained fixed, the coils proved to move radially inwards by approximately 7-10mm. Additional magnetic shielding of other BLAST components became necessary during running. In order to establish the effect on the field, the field mapping was repeated in June 2005 at the end of the final running period and no considerable misalignments or shifts were observed[76]. Figure 3-13 shows the comparison of the field map with the Biot-Savart calculations for the vertical component of the BLAST field, B_y , along the BLAST x-axis. Minor differences between the mapping and the theoretical calculations are most likely due

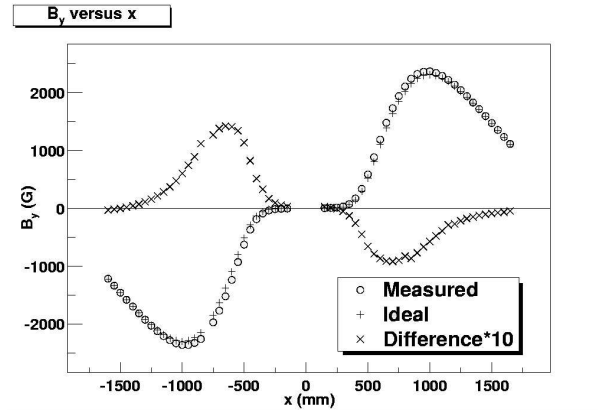


Figure 3-13: BLAST Field Map vs Biot-Savart Calculations for B_y , 500 mm downstream of the target in the midplane

to the presence of extraneous magnetic materials and the real position of the coils which was known to within 1-2 mm [77]. Additionally, the measured coil motion mentioned above was not included in the Biot-Savart calculation shown in Figure 3-13 [77].

3.5.3 Time-of-Flight Scintillators

The BLAST Time-Of-Flight (TOF) system consists of an array of scintillators that provide fast timing information and triggering. In each of the two sectors of BLAST, sixteen TOFs cover a scattering angle range of $20^\circ < \theta < 80^\circ$. Four backward-angle TOFs (BATS) in each sector of BLAST provide additional polar angle coverage outside of the drift chamber acceptance from 90° to 120° . In each sector, the four most forward angle TOFs at $\theta < 40^\circ$ are 119.38 cm in length, 15.24 cm wide, and 2.54 cm thick while the rest of the TOFs at $\theta > 40^\circ$ are 180.00 cm long, 26.2 cm wide, and 2.54 cm thick. The TOFs are made from Bicron¹ BC-408 organic plastic scintillator which was chosen because of its fast response time and long optical attenuation length.

The energy deposited in the scintillators by the moving particles that interact with the plastic material makes the free valence electrons of the scintillator molecules undergo

¹Bicron, 12345 Kinsman Rd, Newbury, OH 44065 USA

transitions to higher states through excitations of the rotational and vibrational modes. When the molecules relax back to their original states light is emitted and lucite light-guides of a geometry designed to minimize the effect of the BLAST magnetic field direct photons through joints made with optical glue to a 3 inch diameter Electron Tubes² 9822 PMT.

The fast timing characteristic of the BLAST TOFs allows the scintillators to handle

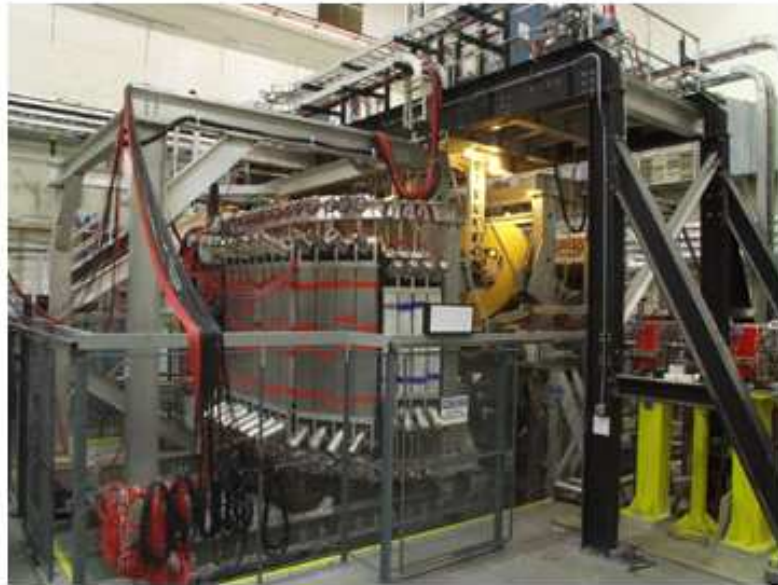


Figure 3-14: View of BLAST Right Sector TOF System

high event rates. The specifications for BC-408 are listed in Table 3.5 [78].

Magnetic shielding (Mu-Metal) is placed around each PMT in order to provide shielding from the BLAST magnetic field. Each plastic TOF bar is wrapped in black kapton in order to prevent light leaks.

The electronic base for each PMT consists of an actively stabilized voltage divider

²Electron Tubes Limited, Bury Street, Ruislip, Middlesex, HA4 7TA, England

Base	Polyvinyltoluene
Refractive Index	1.58
Rise Time (ns)	0.9
Decay Time (ns)	2.1
Pulse Width, FWHM (ns)	~2.5
Attenuation Length (cm)	210
Peak Wavelength (nm)	425

Table 3.5: Properties of Bicron BC-408 Organic Plastic Scintillator

supplying the high voltage to the PMT as well as returning the output signal of the PMT to the data acquisition system [71]. By setting the voltage between the photocathode and the first dynode with a zener diode, the timing is made independent of the tube gain [71].

3.5.4 Time-of-Flight Scintillator Performance

The Time-Of-Flight (TOF) scintillator system was designed, built, tested, commissioned and maintained by the UNH Nuclear Physics Group. It provided triggering and fast timing information to the BLAST data acquisition system.

Pre-commissioning Testing of the Time-of-Flight System

After the TOF system was built at UNH, the scintillators were moved to the William F. Bates Linear Accelerator Center. Prior to installation in the BLAST detector subframes, the detectors were individually gain-matched and tested for efficiency and time resolution in the *Detector Testing Facility* at Bates.

The gains of the TOF PMTs were matched using cosmic rays such that the peak of the ADC spectrum was at a target ADC channel of 1250. The selection of channel 1250 left adequate bandwidth in the ADC spectrum so that the maximum energy lost by protons and deuterons would fall below the maximum ADC channel of 8192. This took into account

that cosmic rays are minimum ionizing particles and when installed in BLAST the same gain would correspond to electrons which lose approximately 2 MeV/cm in organic plastic scintillator material.

The efficiency of each time-of-flight scintillator was measured by placing two small scintillating paddles above and below each TOF and forming a trigger using cosmic rays. Efficiency was defined by the ratio between the number of events detected by the TOF and the number of triggers. Measurements were taken at three positions for each TOF, in the middle of each detector and close to the ends. A schematic of the efficiency setup is shown in Figure 3-15 [79].

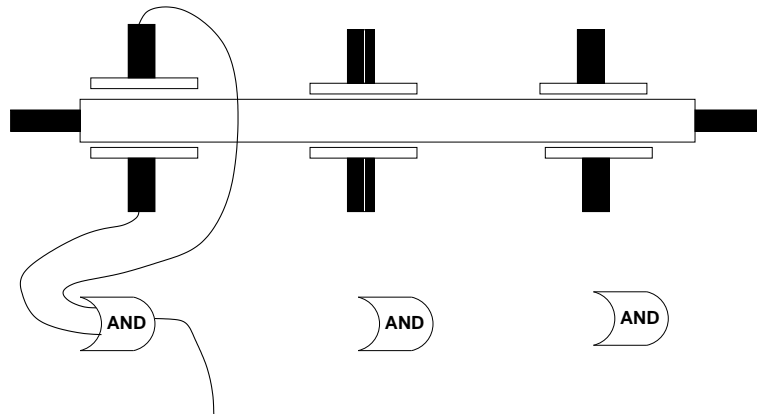


Figure 3-15: TOF Efficiency Measurement

The time resolution of each TOF was measured [80] by placing it in between two reference detectors, which were themselves placed between two small paddles providing positional precision for a coincidence trigger using cosmic rays. If TOFs 1 and 2 are the reference detectors and TOF 3 is the detector for which the time resolution is being measured, we have:

$$t_m = \frac{t_L + t_R}{2} \quad (3.3)$$

the mean time, t_m , for each of the three TOFs, defined as the average time of the two (left and right) PMT channels. If TOF 3 is placed exactly between the reference detectors with respect to the floor, then the difference

$$t_{diff} = \frac{t_{1m} + t_{2m}}{2} - t_{3m} \quad (3.4)$$

should be zero. The time-of-flight between the two reference detectors is

$$t_{tof} = t_{1m} - t_{2m} \quad (3.5)$$

The error on t_{diff} is

$$\sigma_{diff}^2 = \frac{1}{4}\sigma_{1m}^2 + \frac{1}{4}\sigma_{2m}^2 + \sigma_{3m}^2 \quad (3.6)$$

The error on the time-of-flight t_{tof} is

$$\sigma_{tof}^2 = \sigma_{1m}^2 + \sigma_{2m}^2 \quad (3.7)$$

Combining these we can write the error on t_{3m} as

$$\sigma_{3m} = \sqrt{\sigma_{diff}^2 - \frac{1}{4}\sigma_{tof}^2} \quad (3.8)$$

The error σ_{3m} then defines the time resolution of that detector and can be determined by the above formula.

Results of TOF Pre-commissioning Testing

The results of both the efficiency and time-resolution testing are shown in Figure 3-16 and Figure 3-17, as they were presented at the First Joint Meeting of the Nuclear Physicists of the American and Japanese Physical Societies, October 17 - 20, 2001 [81].

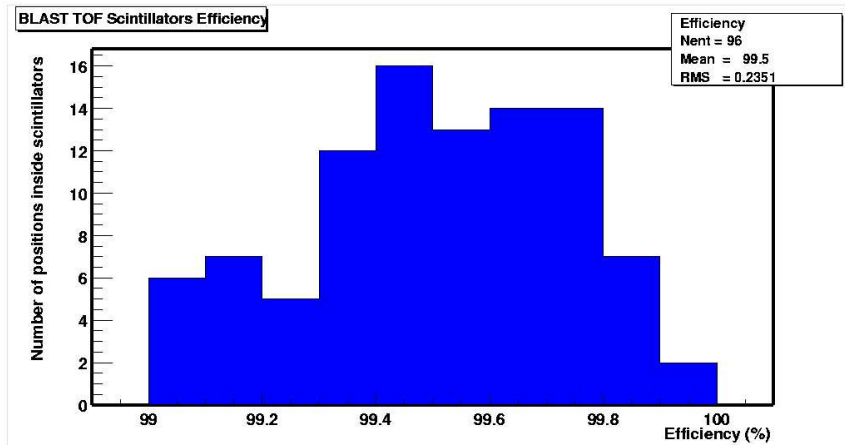


Figure 3-16: TOF Efficiency. All TOFs performed with an efficiency greater than 99%

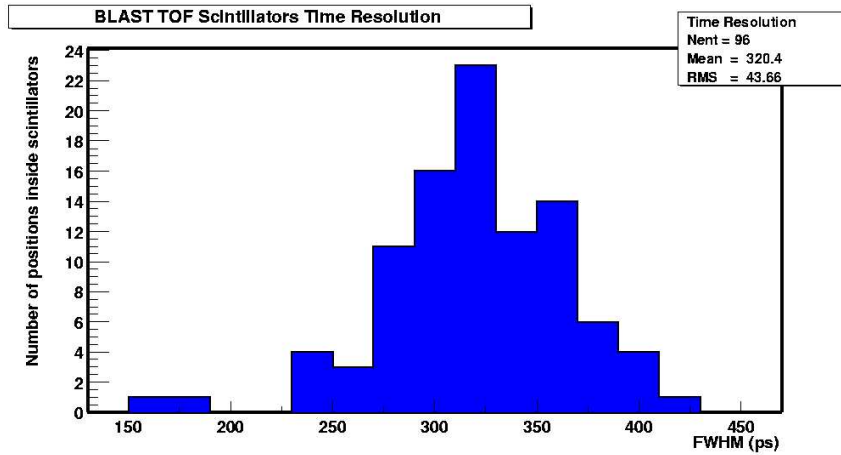


Figure 3-17: TOF Time Resolution

TOF Commissioning and Production Running

During commissioning, TOF gains were measured with pedestal subtraction, refining the gain information of the pre-commissioning period. To determine the pedestal the analysis code demanded that no true TDC signal occurred for a given ADC signal. The pedestal values were determined in this manner for all runs and written to the BLAST MySQL database [82] which supported most of the BLAST control and analysis software. Figure 3-18 displays raw (blue) and pedestal-subtracted (shaded) ADC spectra for one quadrant of BLAST TOF detectors.

The high voltage (HV) settings for the TOF PMTs were set and covered an operating

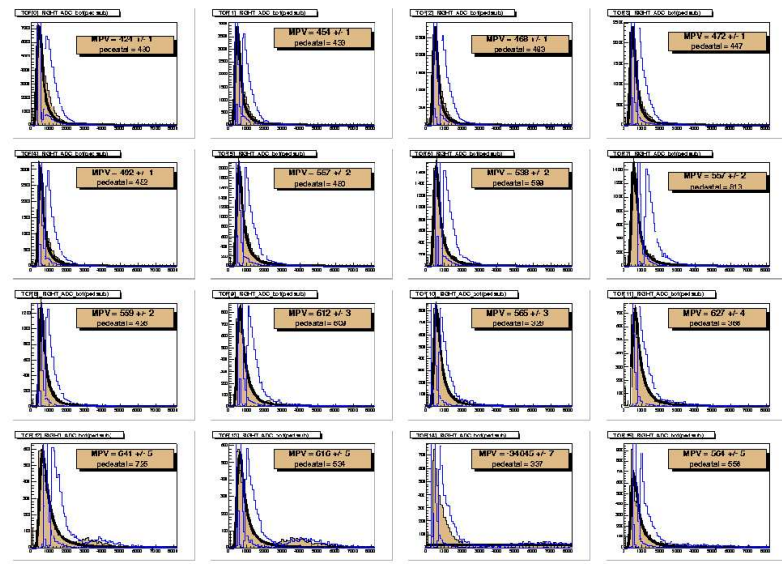


Figure 3-18: TOF Pedestal-Subtracted Gains

range of -1600V to -2400V. Standby voltages were set to -500V for all channels. These values were stored in the BLAST MySQL database [82].

The gains of the TOF PMTs were monitored during running with beam by applying

a Landau fit to the minimum ionizing peak in the TOF ADC spectra for each channel. Figure 3-19 shows this technique for one quadrant of BLAST.

The most probable value (MPV) of the Landau fit was taken as a quantification of

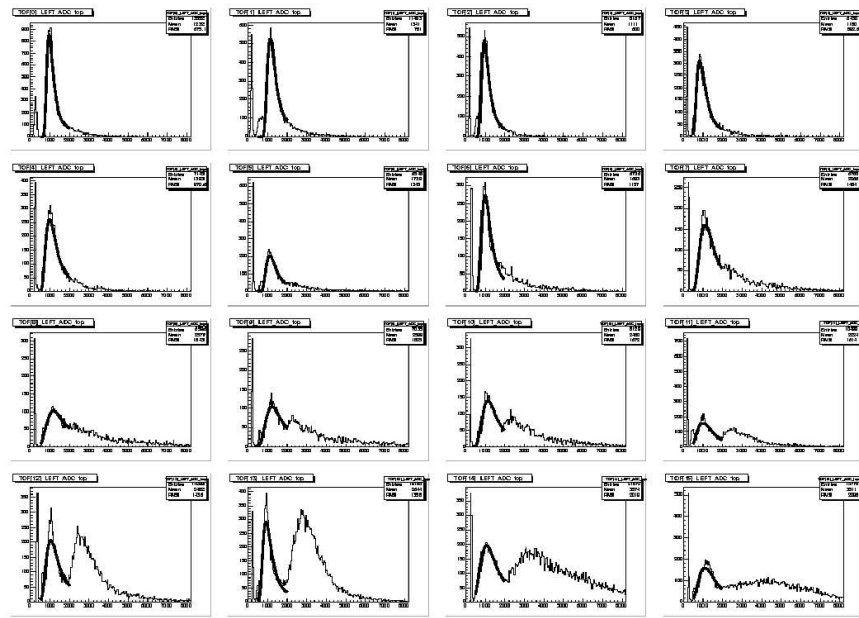


Figure 3-19: TOF Gains: The peak on the low end of the ADC spectrum is due to minimum ionizing electrons, the bump at higher ADC channel is due to protons

TOF gain. This value is plotted versus run number for a typical hydrogen commissioning dataset and is shown in green in Figure 3-20, while the pedestal values are shown in blue and the red represents the target channel which the TOF gains attempt to approach.

During the BLAST commissioning period, the efficiency of the TOFs was checked by placing a small trigger paddle on the outside of each TOF with respect to the beam and a second trigger paddle (*start counter*) along the target scattering chamber. The efficiency was found to still be in agreement with the initial measurements. The optimal CFD threshold setting was determined to be 31.3 mV for all TOF channels.

Due to variations in the BLAST data acquisition TDC electronics as well as cable

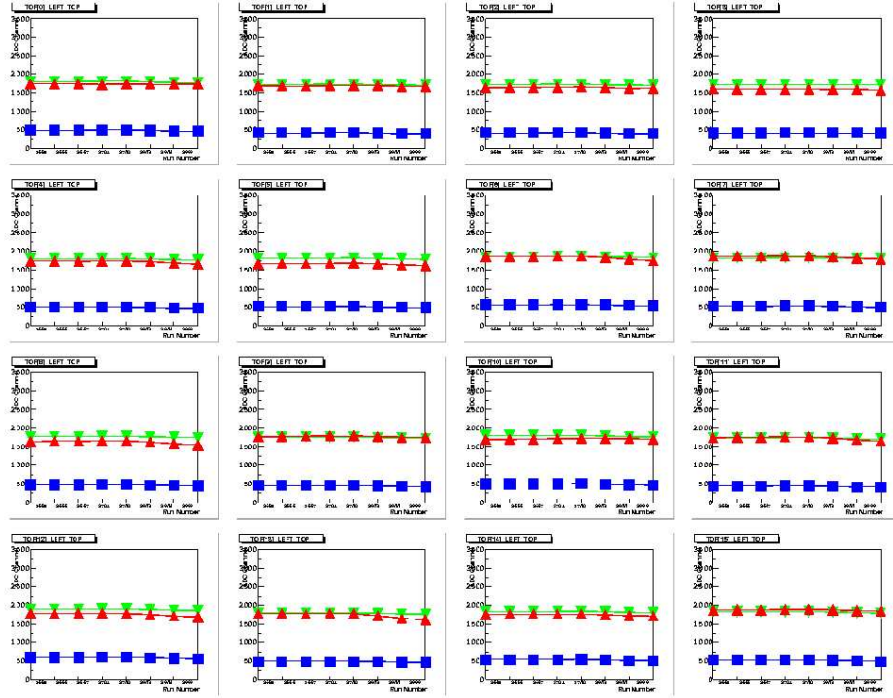


Figure 3-20: TOF Gain and Pedestals vs Run Number: The y-axis is the full scale ADC for the TOF PMTs. The x-axis is run number.

lengths and other inconsistencies there exists an offset in timing for each TOF channel. These offsets were determined using low angle cosmic rays [83] and were also written to the BLAST MySQL database. The low angle cosmic rays, mainly consisting of muons with $\beta \simeq 1$, provided a left-right sector coincidence rate of ~ 1.4 Hz and allowed for timing calibration to be conducted periodically.

3.5.5 Wire Chambers

The BLAST wire chambers (WCs) provided tracking information (such as momentum, scattering vertex position, particle identification etc.) for charged particles and were located between the target and the TOFs. The WCs were fit between two of the field coils in each sector of BLAST and covered a polar range of $20^\circ < \theta < 80^\circ$ and $\pm 17.5^\circ$ in azimuth ϕ . BLAST used six chambers, arranged in groups of three per sector with the smaller

chamber closer to the beamline to form a trapezoidal shape as shown in Figure 3-21. The

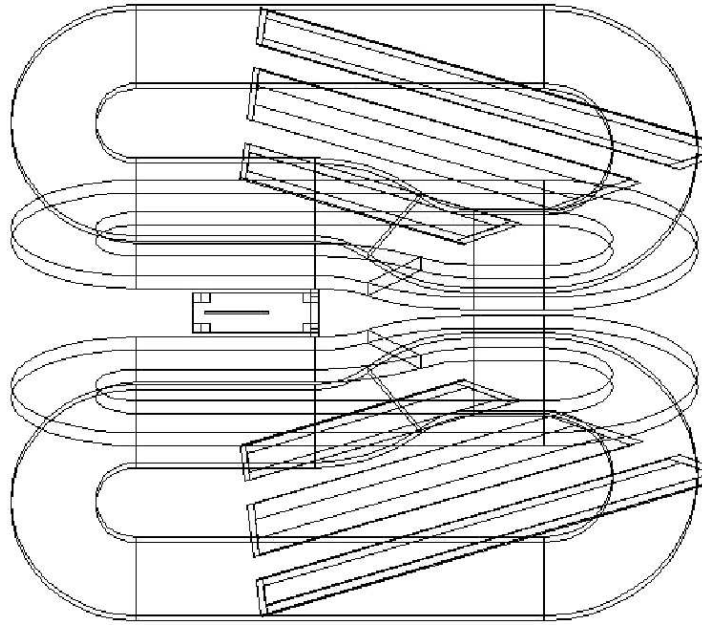


Figure 3-21: The drift chambers for BLAST are shown here in an overhead view with non-visible lines shown for display purposes

geometry was largely determined by space restrictions of the BLAST design. Each chamber consists of individual cells, rectangular arrays of 39 wires with transverse dimensions $4\text{cm}\times 7.8\text{cm}$ [84]. There are three kinds of wires in the cells: *sense* wires, made of tungsten, connected to amplifier-discriminator cards and used for readout, *guard* wires, made of copper, used for gain-matching of the sense wires, and *field* wires, also made of copper, used to shape the electric field in the region.

Allied Electronics delivered the aluminum chassis for the chambers to the MIT campus in 2000 where the individual pieces were assembled and the chambers strung. Then the chambers were transported to MIT-Bates for installation in the South Hall. After installation, electronics (TDC modules for readout, amplifiers, High Voltage crates) were connected to the chamber wires. The intrinsic resolution of the chambers was obtained after calibration by calculating the hit position deviation from a straight line fit for each event and histogramming the results. The BLAST wire-chambers resolution was of the order of $130\mu\text{m}$ [84]. The factors that affected the resolution were time-to-distance conversion uncertainties, electron diffusion and energy loss as well as knowledge of the geometry.

The principle underlying the operation of the chambers is the traveling of charged particles through a gas volume. Electrons produced by ionization of the chamber gas drift toward the sense wires and produce a *hit*. Time-to-distance relationships can be used in order to determine the trajectory of the incident particle through knowledge of the field characteristics and the gas properties.

Each chamber has two superlayers which each contain three layers of sense wires. From *clusters* of hits a so-called *stub* is formed. The sense wires are staggered to discriminate against false stubs. Furthermore, a stereo angle of $\pm 5^\circ$ is alternated every other layer [85]. This allows to intersect stub planes and form *segments*. In this way, hits form clusters, clusters form stubs, stubs form segments, and segments form *tracks*.

Each sector of BLAST has three chambers which share a single gas volume. A dedicated gas flow system was built for operating the BLAST drift chambers. The gas mixture used was 82.3% Helium and 17.7% isobutane. Helium is used as the *ionization gas*, which is essentially the main mechanism for tracking. Isobutane is used as a *quenching gas* in order to absorb photons created by electron recombination. Careful consideration has to be given to the mixture of ionization and quenching gas used in the chambers so that there is no reduction of the tracking efficiency. The entrances of the chambers were composed of two thin sheets of mylar in order to reduce multiple scattering. The gap between the

mylar sheets is purged with nitrogen to protect phototubes on the adjacent detectors from helium poisoning [86]. The exit windows are similarly flushed but also have a thicker acrylic window.

3.5.6 Wire Chamber Performance

In the absence of multiple scattering, the momentum resolution is

$$\frac{\Delta p}{p} = \frac{8p}{0.3L_0} \frac{1}{\int B d\ell} \sqrt{(\epsilon_1/2)^2 + (\epsilon_2/2)^2 + (\epsilon_3/2)^2} \quad (3.9)$$

where $\epsilon_i = \sigma/\sqrt{N}$ with σ being the position resolution for the i^{th} ($i = 1, 2, \text{ or } 3$) cluster measurement of a track stub, N the number of measurements, L_0 the track length and $\int B d\ell$ the integral of the BLAST magnetic field along the path of the particle [75].

The momentum of an ultra-relativistic elastically scattered electron can be expressed as a function of electron scattering angle θ_e .

$$k' = \frac{\epsilon}{\left(1 + \frac{2\epsilon \sin^2(\theta_e/2)}{M_p}\right)} \quad (3.10)$$

The angle of the scattered proton can also be expressed as a function of θ_e

$$\theta_p = \sin^{-1} \left(\frac{1}{1 + \tan^2(\frac{\theta_e}{2}) \left(\frac{\epsilon}{M_p} + 1\right)} \right)^{\frac{1}{2}} \quad (3.11)$$

Also, the azimuth angles ϕ_e and ϕ_p for the electron and proton respectively, are related by coplanarity. Comparing the above calculated variables with those measured by the drift chambers yields a measurement of reconstruction resolution.

Using $130 \mu\text{m}$ as the intrinsic wire resolution and incorporating Monte Carlo studies of multiple scattering, the present BLAST drift chamber reconstruction resolution values, including the vertex resolution Δz_e , are summarized in Table 3.6 [75].

The present measured values are close to those specified in the BLAST Technical Design

Reconstruction Variable	Design Value	Measured Value
$\Delta k'$	2%	3%
$\Delta\theta_e$	0.30°	0.45°
$\Delta\phi_e$	0.50°	0.56°
Δz_e	1.0 cm	1.0 cm

Table 3.6: BLAST Drift Chamber Reconstruction Resolution

Review.

3.5.7 Čerenkov Detectors

BLAST used Čerenkov counters (CCs) in order to distinguish between electrons and negatively charged pions. Wire chamber tracking is not sufficient for this purpose, as the curvature of the trajectory in the magnetic field is similar for electrons and negative pions. Also, electron-pion separation based on timing is difficult in some kinematic regions.

A charged particle traveling in a medium with speed larger than the speed of light in that medium produces atomic excitations which cause light emission in the form of a coherent wavefront at a specific angle with respect to the charged particle's direction of travel. A cone is formed, and its half-angle θ is given by:

$$\theta = \tan^{-1}\left(\sqrt{n^2\frac{v^2}{c^2} - 1}\right) \quad (3.12)$$

Figure 3-22 shows this process.

The design of the Čerenkov counters took into account BLAST's high magnetic field, space restrictions, efficiency and energy loss. BLAST has four Čerenkov boxes in each sector. Each box has a section of optically transparent aerogel³ and a section used for light collection. Low carbon steel was added to cancel the magnetic field from the toroid. The Čerenkov radiation produced in the aerogel is incident upon a diffusively reflective

³Matsushita, Japan

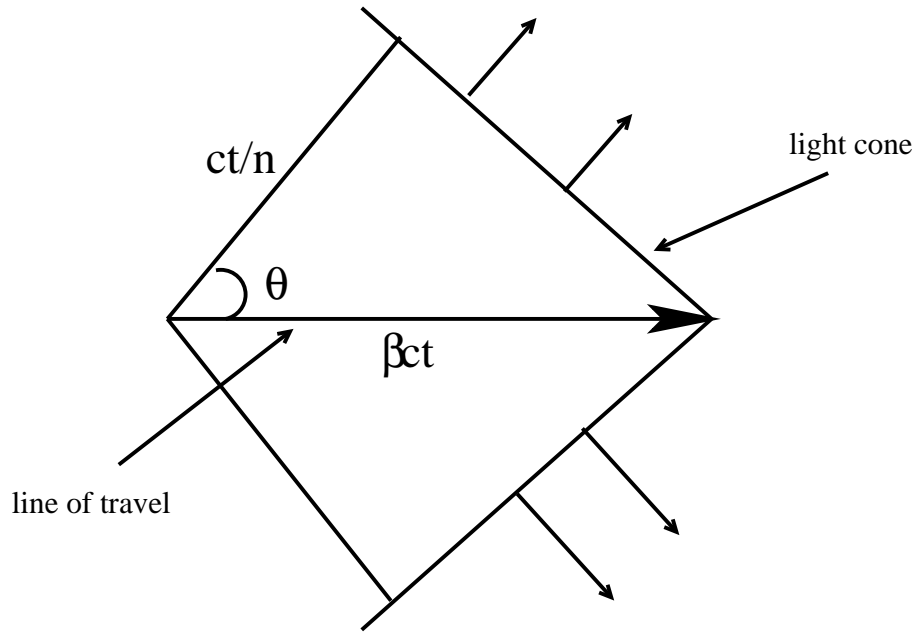


Figure 3-22: Light cone emitted by excitation of medium atoms when the speed of a charged particle exceeds that of light in the medium. The angle θ is given by equation 3.12

surface⁴ and is collected by 5 inch Photonis⁵ phototubes. Figure 3-23 shows one of the Čerenkov boxes.

The choice of the index of refraction n of the aerogel was based on pion momentum thresholds [71] and a choice was made by balancing complete pion rejection and sufficient light output for ultra-relativistic electrons.

The size of the Čerenkov boxes were chosen to match the corresponding TOF lengths because of geometry considerations. The smallest box covers $20^\circ < \theta < 35^\circ$ and contains 6 PMTs, the middle-size box covers $35^\circ < \theta < 50^\circ$ and contains 8 PMTs, and the largest box covers $50^\circ < \theta < 70^\circ$ and contains 12 PMTs [87]. The initial BLAST design called for a Čerenkov box covering the last section of TOFs out to 80° but this box stopped the majority of deuterons in this region and was moved in front of the BATs, where it helped

⁴LabSphere, NH USA

⁵Photonis, Avenue Roger Roncier, Z.I. Beauregard, B.P. 520, 19106 BRIVE Cedex, FRANCE

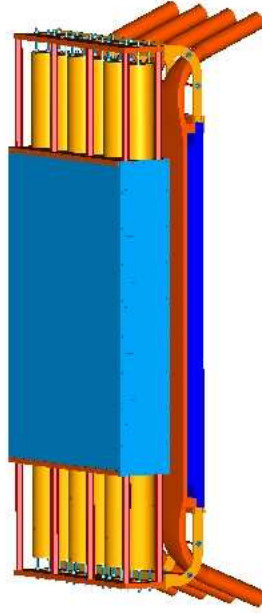


Figure 3-23: Side view of one of the individual Čerenkov counters used at BLAST within its mounting frame. Note the light box (blue) and the PMTs (yellow). Additional shielding installed to encase the PMTs is not shown here

the event selection for the hydrogen experiment. Some of the design characteristics of the counters are listed in Table 3.7.

	Box 1	Box 2	Box 3	Box 4
Number of PMT	6	8	12	12
Angle subtending	$20^\circ - 35^\circ$	$35^\circ - 50^\circ$	$50^\circ - 70^\circ$	$95^\circ - 115^\circ$
Aerogel thickness	7cm	5cm	5cm	5cm
Refraction Index	1.02	1.03	1.03	1.03

Table 3.7: Čerenkov counter specifications

3.5.8 Čerenkov Detector Performance

Because the Čerenkov counters were located between the drift chambers and the time-of-flight scintillators, a coincidence of drift chamber tracks and hits in scintillators provided the trigger in measuring Čerenkov efficiency for six of the eight Čerenkov boxes (the other

two boxes were outside of the wire chambers region, so only pre-commissioning testing indicating similar results were conducted on them). An efficiency of approximately 85 % was measured with some degradation in efficiency toward the backward angle boxes. This was found to be due to edge effects where the downstream curved electron track completed the trigger with the most upstream TOF but missed the corresponding Čerenkov counter [84]. Figure 3-24 summarizes the efficiency of the Čerenkov counters with respect to corresponding TOF detectors.

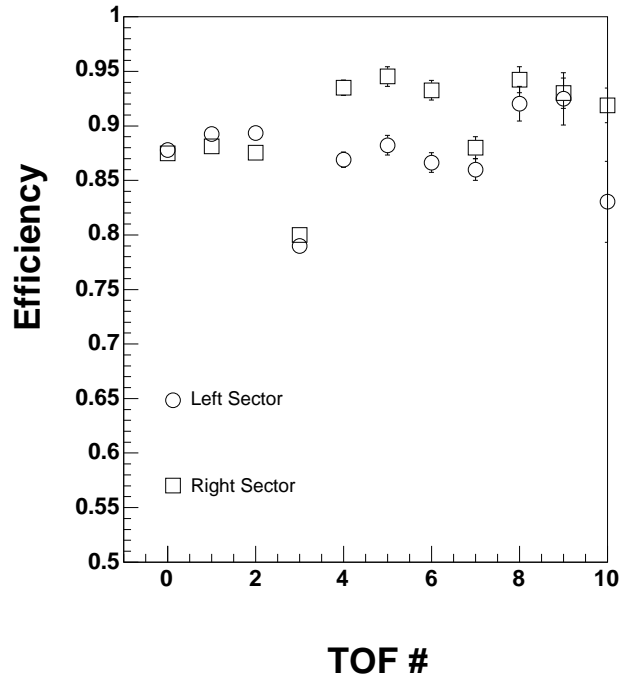


Figure 3-24: Čerenkov Detector Efficiency Measurements

3.6 Data Acquisition System

RG58 coaxial cables take the analog signals from the detectors to the BLAST data acquisition system (DAQ). The first level trigger of BLAST has a LeCroy⁶ CAMAC crate containing various programmable ECL logic modules for each sector of BLAST. Coincidence circuits and scalers for each channel are hosted by a VME crate. The quality of data is improved by a second level trigger requiring good wire chamber tracks, thus greatly reducing background. A trigger supervisor (TS) combines the first and second level trigger and provides gates for analog-to-digital converters (ADCs) and starts for time-to-digital converters (TDCs).

3.6.1 BLAST Trigger

The First Level Trigger

The trigger system can be divided logically into three distinct parts. First, TOF and NC phototube signals are sent through an analog splitter, while the analog signals from the Čerenkov PMTs are combined in a CAEN⁷ N402 analog adder before being split up. After splitting the signal, one part is delayed by 500 ns before being sent to the ADCs while the *prompt* signal is sent directly either to LeCroy constant fraction discriminators (CFDs - in case of the TOFs and CCs) or to LeCroy leading edge discriminators (LEDs - in case of the NCs and LADs). Coincidence, delay and fan-out modules are situated after the CFDs and LEDs, either for the purpose of requiring coincidence between the two photomultipliers of the TOFs, NCs and LADs or for sending signals to TDCs and the VME scalers [77].

Next, the logic signals in each sector go to LeCroy memory look-up units (MLU) where they are correlated.

⁶LeCroy Corporation 700 Chestnut Ridge Road, Chestnut Ridge, NY

⁷CAEN S.p.A. Via Vetraia, 11 55049 - Viareggio (LU) - ITALY

Last, the outputs of both sector MLUs are processed by the cross-sector MLU (XMLU) which is responsible for tagging each event with a trigger type. The ECL output of the XMLU is converted to NIM logic and then enters the trigger supervisor (TS). The TS manages trigger type distribution, prescaling, and busy/inhibit signals [77]. A CAEN mean timer module makes TOF timing independent of the azimuthal angle ϕ . A LeCroy 4564 OR module provides a common strobe to the TS and - after all the TOF scintillators had been timed up, see subsection 4.6.4 on trigger timing - ensures TOF timing independence of the individual detector firing and thus of the path length from the target to the TOFs.

Trigger types

Since the BLAST experimental program was developed to collect data in various channels simultaneously, the trigger was designed to collect the data while assigning a trigger type to every event, depending on the combination of detectors that fire. Despite the low rate of physical processes at the BLAST beam energy, high background rates in some trigger types caused the data acquisition rate to exceed the maximum handled by the system, resulting in significant *deadtime*. To limit the computer deadtime, less important triggers with high background were prescaled.

trigger	prescale	configuration	rates [Hz]
1	1	One TOF in each sector	$\sim 32/2$
2	1	One TOF in each sector, NC in the other	$\sim 1100/66$
3	10	Two TOF in single sector, with Čerenkov	$\sim 87/5$
4	100	Two TOF in single sector	$\sim 235/14$
5	1	One TOF in one sector, BATS in the other	$\sim 16/1$
6	1000	One backward TOF in single sector	$\sim 760/46$
7	3	One TOF in single sector, with Čerenkov	$\sim 3200/92$
8	1	Flasher trigger	$\sim 3/(n/a)$

Table 3.8: BLAST allows tagging the data with different trigger types. Typical 1st and 2nd level trigger rates are shown in the last column

The Second Level Trigger

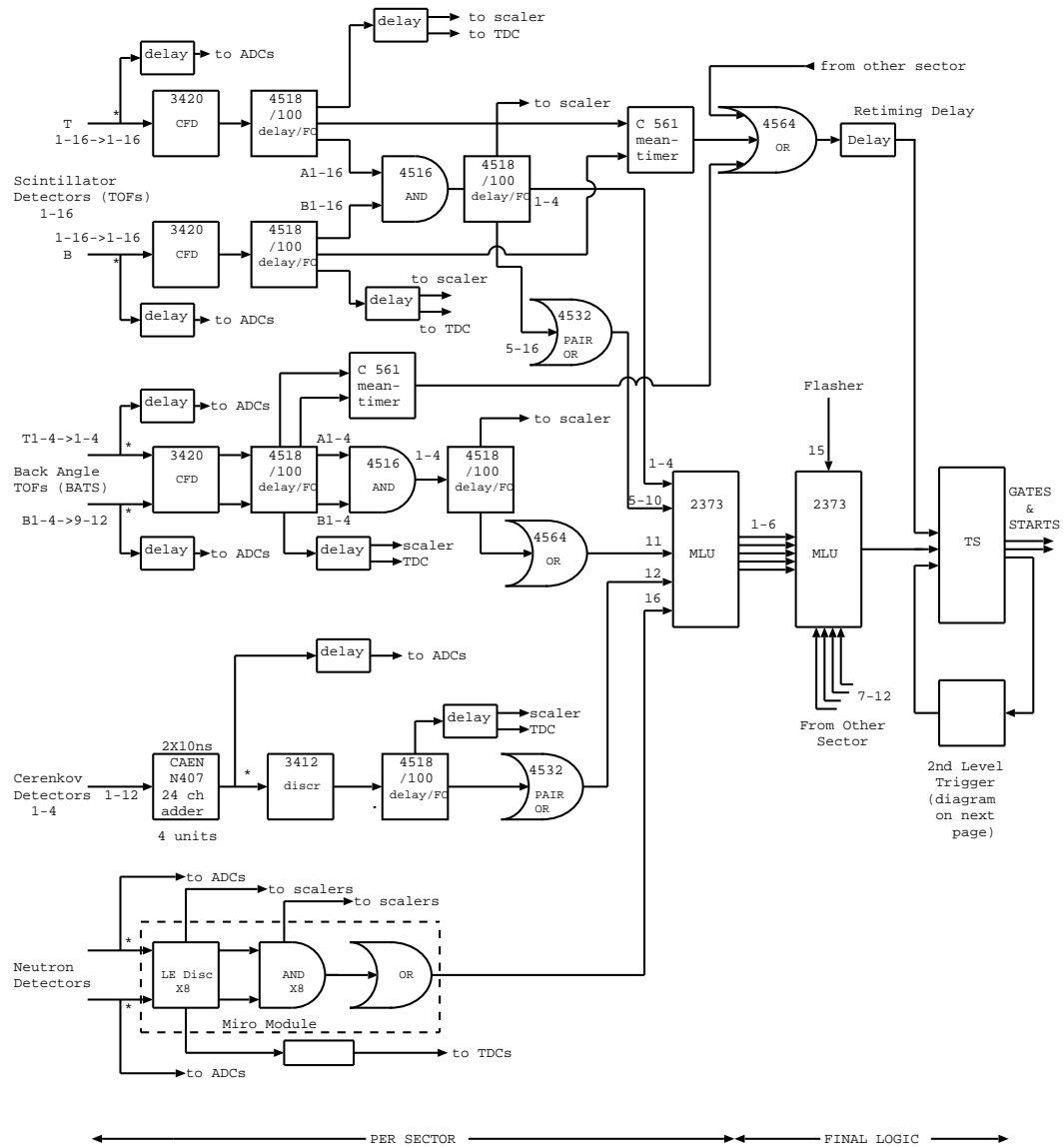
A *good sector WC hit* is defined as a hit in the inner, middle, and outer chamber of the sector. Custom built boards provide a TTL logic signal for groups of sixteen wires. The two sectors can go through an OR or an AND logic and TTL output for a good WC hit is converted to NIM before entering a NIM AND module with a first level trigger signal from the trigger supervisor. The second level trigger increased the fraction of good recorded data by a factor of ten [77].

The Trigger Software

The trigger control software implements the logical diagram using the corresponding hardware, while allowing the user to configure, save and download different settings through its graphical user interface (GUI). The *trigger map* is the link between hardware and software and converts the logic into hardware locations. Book-keeping of the trigger maps, like for all other maps, was done with the help of the BLAST MySQL database [82], as these configuration files had to be updated whenever hardware changes were made.

3.6.2 TDCs and ADCs

LeCroy 1801M ADCs and 1875a TDCs for all detectors except the wire chambers were provided with gates and common starts respectively by the trigger supervisor. A common stop was provided for the LeCroy 1877 WC TDCs. During the time the 400 ns ADC gate was open, charge was integrated with a calibration of 50 fC/ch. The calibration for the TDCs was 50 ps/ch. Struck Fastbus crates hosted the TDCs and ADCs for each of the two BLAST sectors. A Struck Fastbus Interface (SFI) held the two Motorola MV162 single-board computers that served as readout controllers (ROCs). Each ROC had an IP address and could be accessed over a LAN by the ethernet protocol.



note: * all analog signal division in matched impedance passive splitters

Figure 3-25: BLAST Trigger Electronics

3.6.3 CODA Data Acquisition Software

The CEBAF Online Data Acquisition (CODA) software framework was used to collect and record detector information at BLAST. CODA allows various data acquisition systems to be built, depending on the individual needs of an experiment. At BLAST, the embedded readout controllers (ROCs) collected the data in a buffer to reduce protocol overhead before sending it over the network. The various data streams are collected, merged, and formatted by the Event Builder (EB). The EB passes the data to the Event Transport (ET) System which allows for other data streams (e.g. scaler or EPICS data) to be added to the physics data. Then an event recorder (ER) function stores the data in the required format and location. The BLAST CODA uses information stored in an mysql database.

3.6.4 The BLAST DAQ Performance

Trigger Deadtime

To avoid any potential bias in the process of data collection process, the possibility that deadtime may be trigger dependent was investigated. In order to do this, scaler information per trigger type was compared to what is actually recorded in the datastream. At BLAST, there was no significant deadtime variation with trigger type, so trigger types may be combined by correcting only for the prescaling. The overall deadtime was $\sim 15\%$ [75].

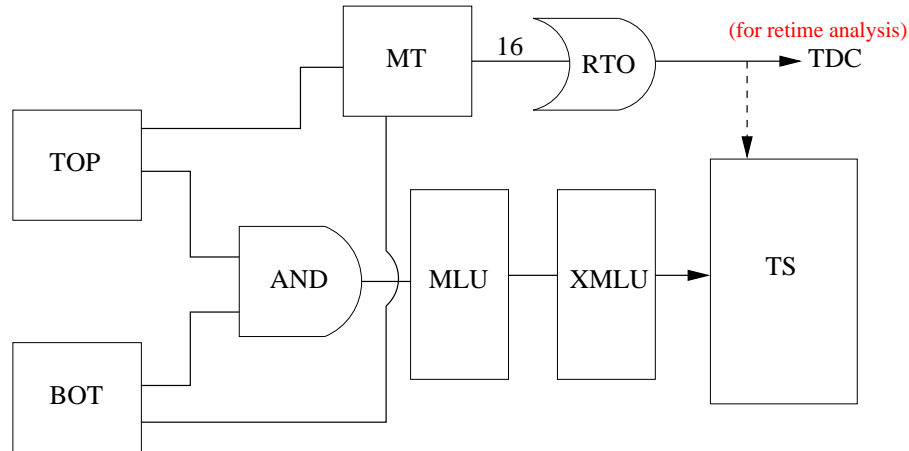
Trigger timing

The 4518 programmable delay modules just downstream of the 3420 CFDs were set so that the signals coming out of the LeCroy 4564 OR module providing the common strobe to the trigger supervisor were synchronized.

The trigger retiming was conducted using a *start counter* which was a scintillator placed just outside the scattering chamber. For this procedure, the TS was run in non-strobed

mode requiring a TRUE signal from the XMLU, as shown in Figure 3-26. Measurements were done for each sector recording coincidence events between the start counter and each TOF in that sector.

The delay of each channel was set so that all the channels were found to be within



MEAN TIMER (MT): MAKES TRIGGER INDEPENDENT OF AZIMUTH

RETIMING OR (RTO): MAKES TRIGGER INDEPENDENT OF PATH LENGTH

Figure 3-26: Trigger for Retiming Analysis

2 nsec of each other. 2 nsec was the lower limit of the 4518 programmable delays. This procedure ensured that the time of flight of electrons (which would provide the start) was independent of the individual TOF detector (and so of the scattering angle θ), thus simplifying the WC reconstruction.

3.6.5 The BLAST MySQL Database

In the early stages of BLAST, the need for a robust framework that would underlie all the software required for controlling the experiment, book-keeping the hardware and analyzing data was recognized.

MySQL was chosen and the BLAST database was implemented, making sure its design

complied with the first four *normal forms* (NF) from the theory of relational databases [88]. A partial view of the initial BLAST MySQL database logic is shown in Figure 3-27. As BLAST evolved, more information was added to the database (as tables or columns).

By the end of the experiment, the BLAST MySQL database had 51 tables, with some

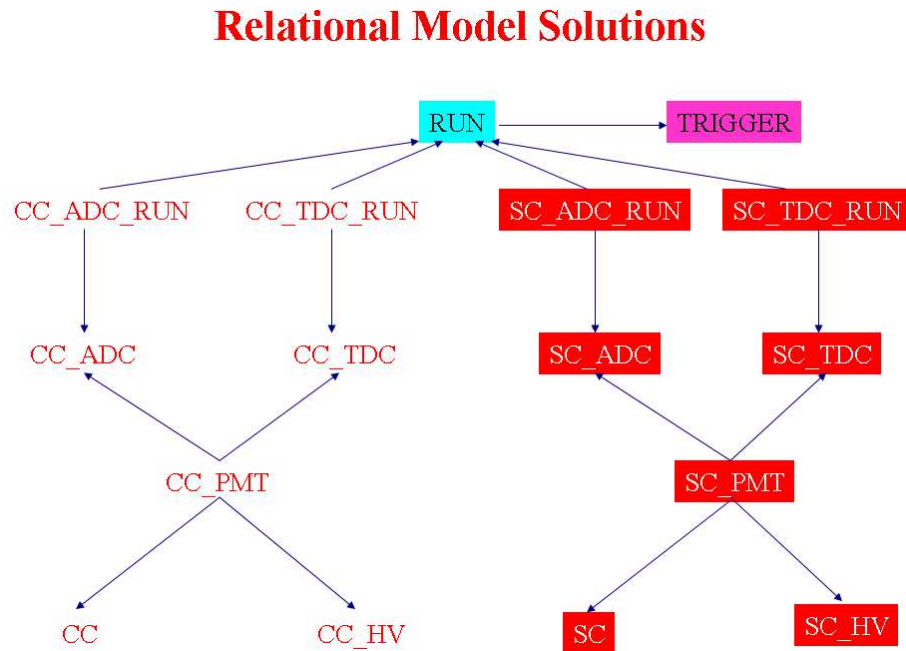


Figure 3-27: Partial Diagram of the Initial BLAST MySQL Database

of the tables holding up to 12M entries. The database proved to be especially useful for recording the ADC pedestals and TDC offsets used by data analysis.

ADC Pedestals

The Fastbus ADC begins integrating current when it receives a gate regardless of a particular PMT generating a signal in response to a true event or not. Even in the absence of a true event, usually there is a DC offset that is internal to the ADC. During each 400 ns ADC gate, that spectrum is recorded and reflects the DC offset. This spectrum

is called a pedestal. To obtain an absolute ADC measurement of a real event the pedestal needs to be subtracted. It was found during BLAST operation that these ADC pedestals varied slightly from run to run. The MySQL database proved very useful in keeping track of the millions of pedestal entries.

TDC Offsets

Due to variations in the BLAST data acquisition TDC electronics as well as cable lengths and other inconsistencies there exists an offset in timing for each TOF channel. These offsets were determined using low angle cosmic rays [83] and were also written to the BLAST MySQL database.

CHAPTER 4

DATA ANALYSIS

Commissioning of the BLAST experiment was done between May 2002 and November 2003. The first polarized ABS hydrogen data were taken in December 2003, with two more periods of hydrogen data taking in April 2004 and November-December 2004. The rest of 2004 and the first half of 2005 were used for the BLAST deuterium program. Information about the three hydrogen data taking periods is shown in Table 4.1. In addition to these running periods where the BLAST target spin angle was set at 47.1° , some hydrogen data was taken in February 2005 with the BLAST target spin angle set at 32° . This was mainly done for consistency checks with the deuterium program that used a target angle of 32° . The first running period of December 2003 used a reversed BLAST magnetic

running period	December 2003	April 2004	November-December 2004
run number range	3787-4744	6273-7001	12184-13266
beam charge	26 kC	52 kC	294 kC
target length	40 cm	40 cm	60 cm
beam polarization	0.65	0.65	0.65
target polarization	0.42	0.37	0.80
target thickness [cm^{-2}]	2.7×10^{13}	2.7×10^{13}	4.9×10^{13}
target spin angle	47.1°	47.1°	47.1°
BLAST field polarity	reversed	nominal	nominal

Table 4.1: Conditions for the three data-taking periods of BLAST with the ABS H_2 target

field (electrons out-bending), in order to have higher rates at lower Q^2 and thus measure the target polarization in less time. The ABS target performance was greatly improved

between April 2004 and November 2004. The 40 cm target cell was also replaced with a 60 cm target cell in order to improve target thickness. These improvements are reflected in the target polarization and target thickness numbers of Table 4.1. For the scope of this thesis, only results from the third running period are presented. Because of the improved target conditions, this running period yielded more than 13 times the statistics of the first two running periods combined.

4.1 Event Selection

Preliminary event selection was done by the reconstruction code, requiring at least one track in each sector with different curvatures (to ensure different charge) or at least one track in each sector regardless of the curvature in case the momentum was greater than 0.7 GeV/c. This last condition was imposed in order to avoid missing events with very high momentum, where the tracks are almost straight.

BAT events were defined by asking for a hit in the BATs and a proton track in the opposite sector, isolating e-p elastic events in the high Q^2 region.

The rest of the cuts described in this section were applied using either track and timing information for BAT events or the two tracks in opposite sectors having the best χ^2 . The analysis used the reconstructed *ep-skim* Data Summary Tape (DST), which was written specifically for the e-p elastic analysis and was based on the Object Oriented Database [89] framework offered by ROOT [90], capitalizing on ROOT's Tree data structures.

4.1.1 Preliminary Cuts from Reconstruction

The wire chambers provide a precise measurement of the scattering angle θ , the azimuthal angle about the beam ϕ and momentum p .

A particle of charge q and mass m moving in a magnetic field \mathbf{B} with a velocity \mathbf{v} will

experience a force $q\mathbf{v} \times \mathbf{B}$. The radius of the particle's trajectory has the expression:

$$r = \frac{p}{qB} \quad (4.1)$$

where p is the momentum of the particle. Knowledge of the BLAST magnetic field along a charged particle's trajectory and the solution to a fit of that trajectory allows the determination of the particle's momentum - this is how the reconstruction of particle momenta is done using BLAST wire chamber information.

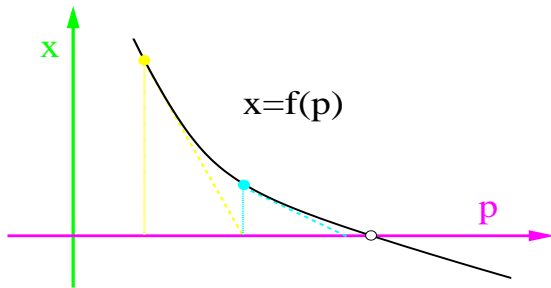
As described in section 3.5.5, three segments form a track in the wire chambers. A first pass fit of these segments is made with the assumption that the track is circular. This initial fast fitting iteratively eliminates bad track candidates.

Once tracks are initially linked, fitting is done numerically by finding the roots of $\mathbf{p} = \mathbf{f}^{-1}(x_0)$ where $\mathbf{p} = (p, \theta, \phi, z)$ and \mathbf{x}_0 contains the coordinates of the track hits. The roots $\mathbf{x} = \mathbf{f}(\mathbf{p})$ are obtained using a modified version of the Newton-Rhapson method [83]. This method is summarized in Figures 4-1(a), 4-1(b), 4-1(c), 4-1(d).

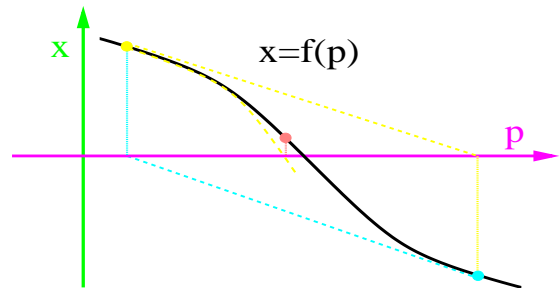
By choosing the two tracks in opposite sectors of BLAST with the best χ^2 (or in the case of a BAT event, the track with the best χ^2 in the opposite sector of a firing BAT), a 0-th order event selection is made. The preliminary reconstruction cuts help eliminate single-track events. Events with multiple tracks in only one sector of BLAST and no BAT hits or with BAT hits and no corresponding proton track in the opposite sector are also eliminated this way.

4.1.2 First Order Cuts

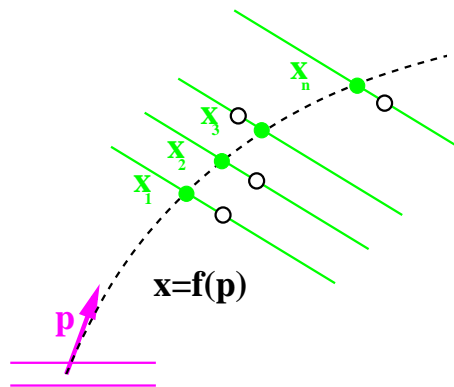
Prior to applying specific elastic cuts, general event selection criteria were imposed in order to reject undesired events. Data passing these cuts were then subjected to more stringent kinematic and timing cuts for selection of elastic e-p events.



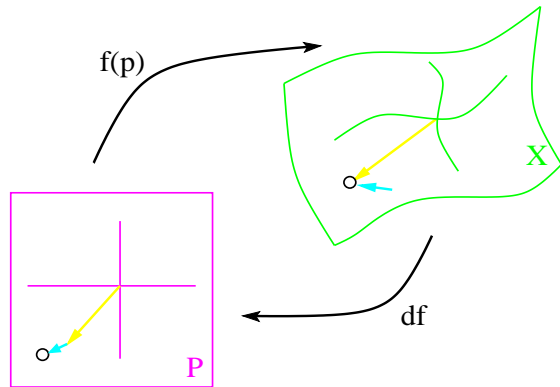
(a) In one dimension, the derivative of f maps the deviation dx from the initial guess to the adjustment dp , and so forth.



(b) In some cases the Newton method may fail to converge, and it is necessary to backtrack to a smaller correction dp .



(c) For track fitting, the function f maps the 4-dimensional track trajectory \mathbf{p} to the 18-dimensional vector of wire hits \mathbf{x} .



(d) In each iteration the trajectory \mathbf{p} is corrected by $d\mathbf{p} = \mathbf{J}^{-1}d\mathbf{x}$, where J is the Jacobian derivative and $d\mathbf{x}$ is the deviation of the simulated track from the wire hits.

Figure 4-1: An application of the Newton-Rhapson method to track fitting.

Vertex Cut

The vertex z of the interaction for each event is obtained from drift chamber reconstruction. A general vertex cut is made to ensure that the observed tracks originate in the target region.

Although the target cell was 60 cm in length over the course of the running period we discuss, the interaction range was assumed to be between $z = -20$ and $+20$ cm. This was chosen as the target holding field was limited beyond this range and was causing deviations in the target spin angle. Figure 4-2 depicts the reconstructed electron and proton vertices before any cuts were implemented. It shows a roughly triangular distribution, as expected from the variation of target density which is higher in the middle of the target chamber and lower towards the ends. The vertex cut eliminated a good part of the unphysical

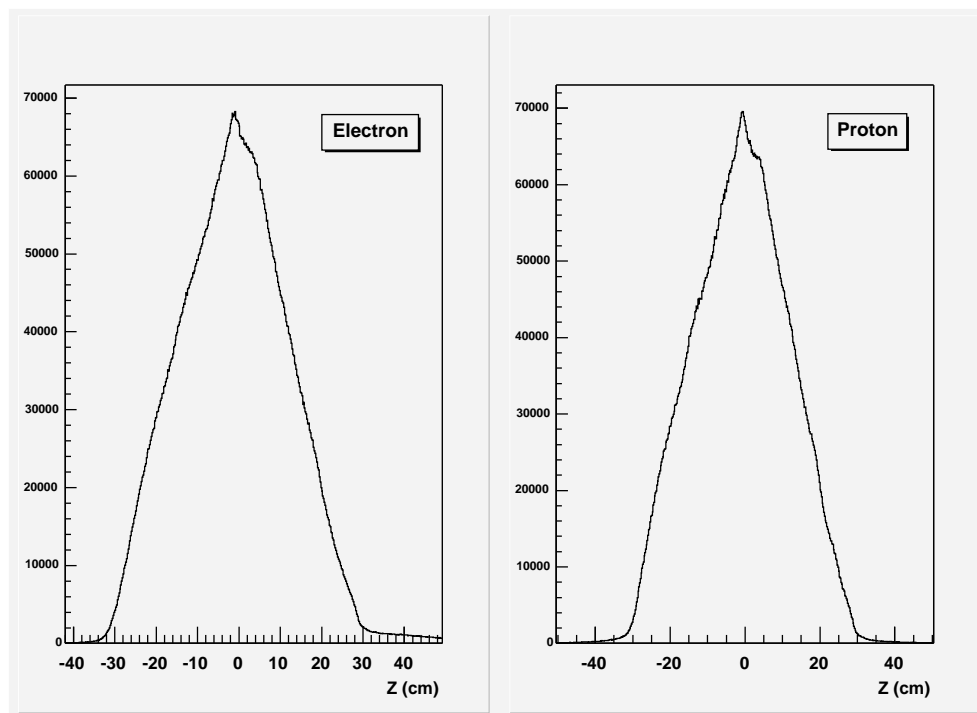


Figure 4-2: Reconstructed electron and proton target vertex before any cuts were implemented. The triangular distribution is expected because of the variation of target density which is higher in the middle of the target chamber and lower towards the ends

events caused by the beam halo striking a collimator upstream of the target.

Coarse Acceptance and Kinematic Cuts

The kinematic range of BLAST is shown in Figure 4-3. Certain global cuts were

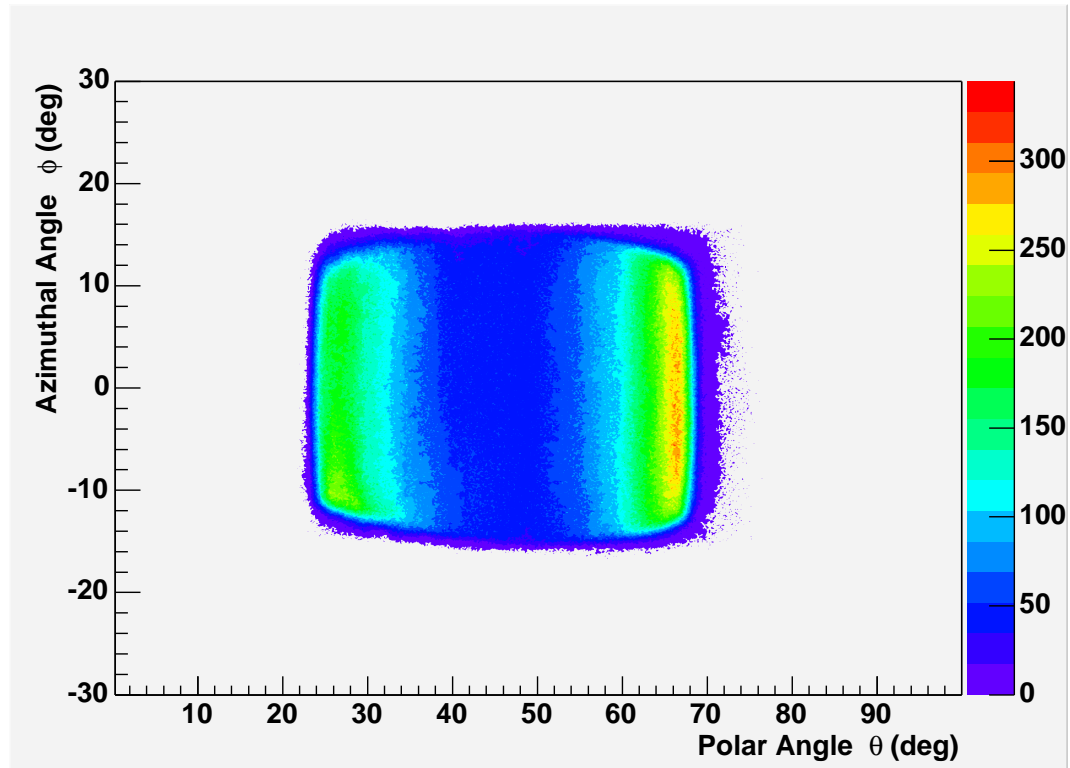


Figure 4-3: BLAST angular acceptance distribution. Note most of the electrons scatter at low values of θ while protons scatter at high values of θ . BAT events cannot be seen in this picture, as the number of BAT events is very small compared to the total number of events

placed in order to eliminate events that physically should be either outside of the BLAST acceptance or clearly outside the kinematic range of the elastic e-p scattering.

In the case of regular (not BAT) events, this meant limiting the polar angle of the observed electrons to be within the range $23^\circ < \theta_e < 73^\circ$, while the polar angle of the observed protons was limited to $35^\circ < \theta_p < 69^\circ$. The azimuthal angle was limited to the range $-14^\circ < \phi < +14^\circ$. Figure 4-4 shows the correlation of the BLAST reconstructed

electron and proton azimuthal angles for a sample of the candidate events. This correlation comes from the fact that after the elastic scattering process the electron and proton trajectories are coplanar due to conservation of momentum.

A cut on the reconstructed proton mass of $M_p > 0.2(\text{GeV}/c^2)$ eliminated π^+ events.

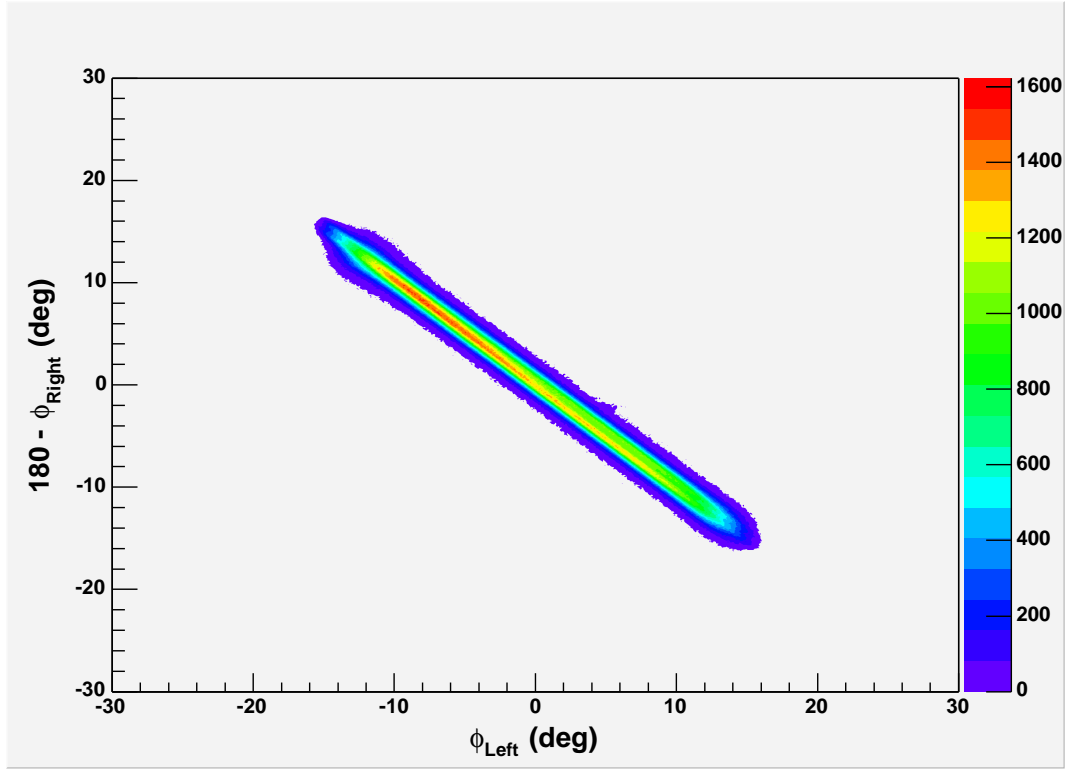


Figure 4-4: BLAST coplanarity of track trajectories

Figure 4-5 shows the reconstructed proton mass before any cuts. Proton time of flight, path length and momentum information are used to determine the reconstructed mass, so a stricter cut could not be safely imposed due to unknown momentum corrections at this preliminary stage.

Figure 4-6 shows the difference between the reconstructed electron momentum and the electron momentum calculated using electron polar angle θ_e track information, also before any cuts were applied.

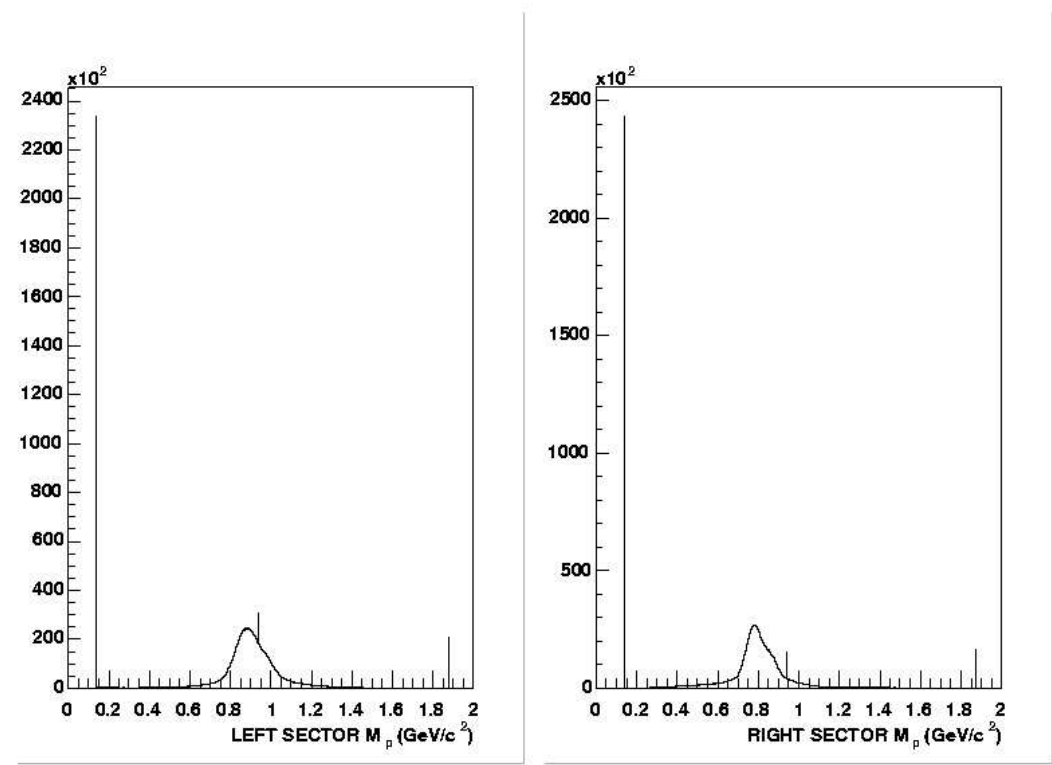


Figure 4-5: Reconstructed proton mass before any cuts were implemented. Note the big spike due to π^+ events that were later eliminated by cuts

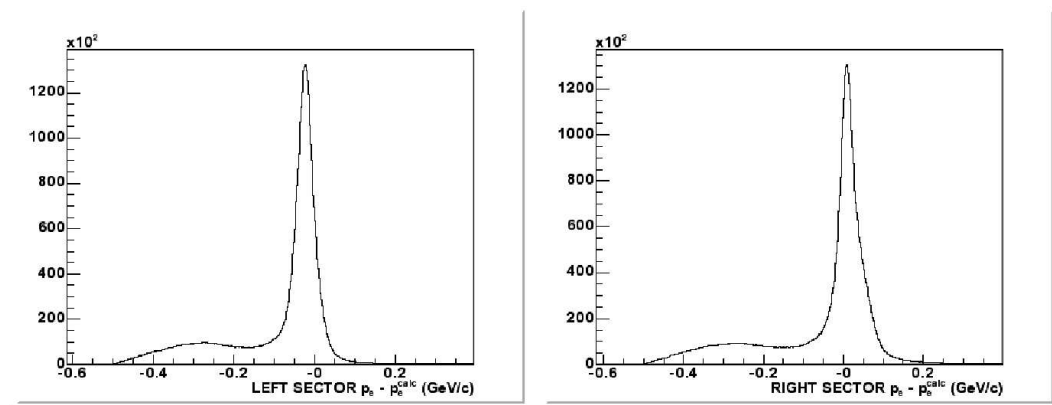
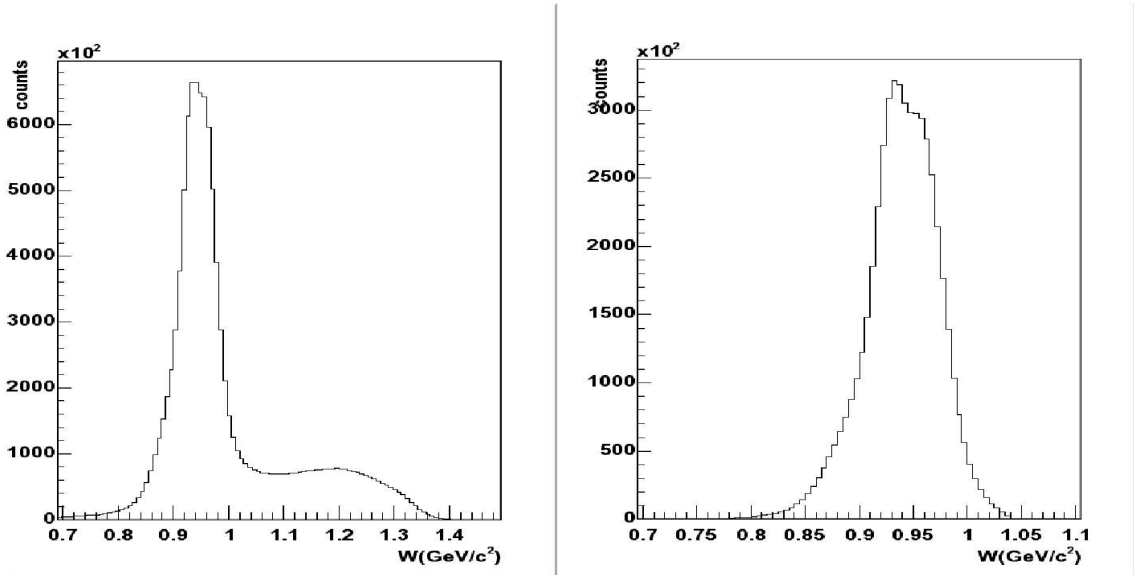


Figure 4-6: Difference between reconstructed electron momentum and electron momentum calculated from elastic kinematic relations before any cuts were implemented. Inelastic events shown here with lower reconstructed momentum caused mostly by pions are later eliminated by elastic cuts

An additional loose, preliminary cut on the invariant mass $W = \sqrt{M_p^2 + 2M_p\omega - Q^2}$, requiring $0.78 (GeV/c^2) < W < 1.04 (GeV/c^2)$ eliminated other undesired events that were still not rejected at this point. Figure 4-7(a) shows the invariant mass spectrum before any cuts whereas Figure 4-7(b) shows, for comparison, the invariant mass spectrum after the elastic cuts described in the next subsection. The above preliminary W cut was looser than a 3σ cut on the spectrum. A trigger type 1 requiring one TOF detector to fire in each sector was also imposed on the regular (not BAT) events.

For the BAT events, preliminary cuts consisted of requiring the polar angle of the



(a) Invariant Mass W spectrum before any cuts. Inelastic events caused mostly by pions are later eliminated by elastic cuts

(b) Invariant Mass W spectrum after all cuts

Figure 4-7: Invariant Mass

observed protons to be $\theta_p < 26^\circ$, in combination with a very loose proton momentum cut of $p_p > 0.75 GeV/c$. A Čerenkov proton veto and an additional cut on the reconstructed proton mass of $M_p > 0.15(GeV/c^2)$ were also used, together with requiring a trigger type

5 (defined by one TOF firing in one sector and the BATs firing in the other sector) and a Čerenkov signal for the electron hitting the BATs. The goal of these cuts was to reflect the kinematic region of interest and reduce background for the timing cuts that followed.

All above coarse cuts were a pre-requisite for the more refined kinematic and timing cuts described in the next subsection, ensuring edge effects did not hinder the polynomial fitting of kinematical variables.

4.1.3 Second Order Cuts

Once the data had been screened for clearly undesired events like π^+ or those originating outside the target region, outside the BLAST acceptance or outside the kinematic region of interest, tighter kinematic constraints were placed in order to further isolate the elastically scattered electron-proton pairs.

Polynomial Kinematic Wire Chamber Cuts

The over-determined e-p elastic kinematic relations were used in order to place cuts. Reconstructed electron momentum can be compared with electron momentum calculated from electron polar angle by forming the variable $(p_e - p_e(\theta_e))$. The same can be done for the reconstructed proton momentum compared with the proton momentum calculated from proton polar angle $(p_p - p_p(\theta_p))$, the reconstructed proton polar angle compared with the proton polar angle calculated from the electron polar angle $(\theta_p - \theta_p(\theta_e))$, the reconstructed proton azimuthal angle compared with the proton azimuthal angle calculated from the electron azimuthal angle $(\phi_p - \phi_p(\phi_e))$ and the proton vertex compared with the electron vertex $(z_p - z_p(z_e))$. While in the case of elastic scattering the above variables are used for event selection, in the case of other reaction channels they can also be used for momentum correction calculations. Figures 4-8, 4-9, 4-10, 4-11 and 4-12 show these quantities histogrammed as functions of θ_e , θ_p , θ_e , ϕ_e and z_e respectively and binned in increments of 1° for the angles and 1 cm for the vertex z_e . Each of the five

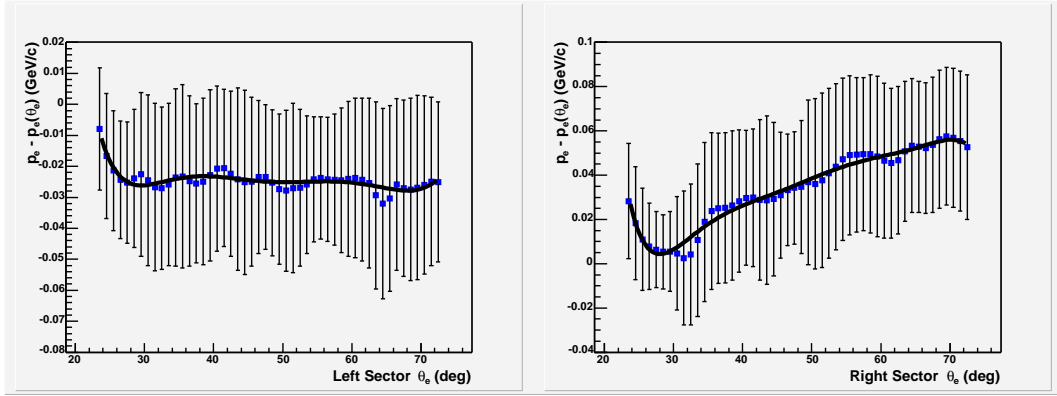


Figure 4-8: Difference of p_e and p_e calculated from θ_e . This differences was binned and fitted to a Gaussian in each bin, with a mean μ and RMS σ extracted for each bin. These μ and σ values were then fitted to polynomials in θ_e . Left (right) corresponds to electrons scattered in the left (right) and protons scattered in the right (left) sector of BLAST.

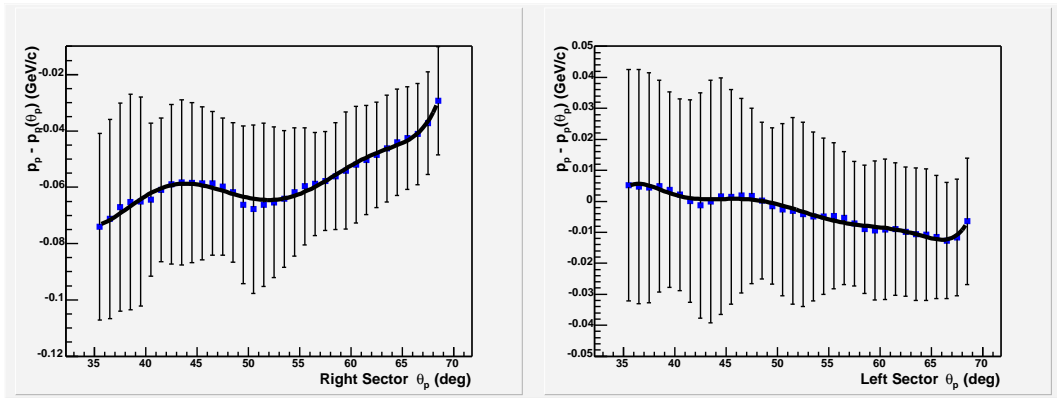


Figure 4-9: Difference of p_p and p_p calculated from θ_p . This difference was binned and fitted to a Gaussian in each bin, with a mean μ and RMS σ extracted for each bin. These μ and σ values were then fitted to polynomials in θ_p . Left (right) corresponds to electrons scattered in the left (right) and protons scattered in the right (left) sector of BLAST.

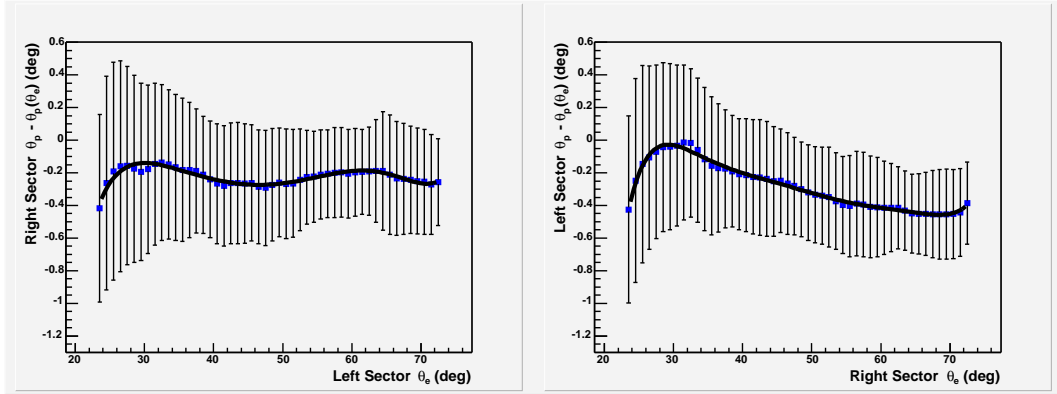


Figure 4-10: Difference of θ_p and θ_e calculated from θ_e . This difference was binned and fitted to a Gaussian in each bin, with a mean μ and RMS σ extracted for each bin. These μ and σ values were then fitted to polynomials in θ_e . Left (right) corresponds to electrons scattered in the left (right) and protons scattered in the right (left) sector of BLAST.

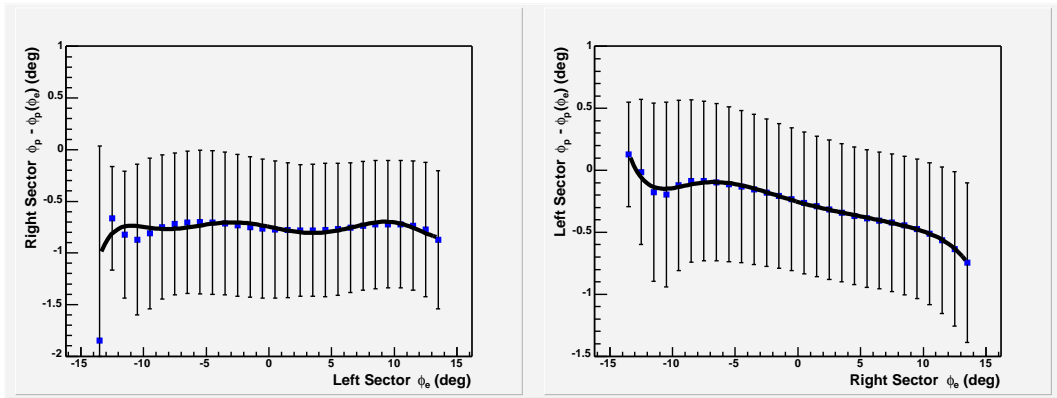


Figure 4-11: Difference of ϕ_p and ϕ_e calculated from ϕ_e . This difference was binned and fitted to a Gaussian in each bin, with a mean μ and RMS σ extracted for each bin. These μ and σ values were then fitted to polynomials in ϕ_e . Left (right) corresponds to electrons scattered in the left (right) and protons scattered in the right (left) sector of BLAST.

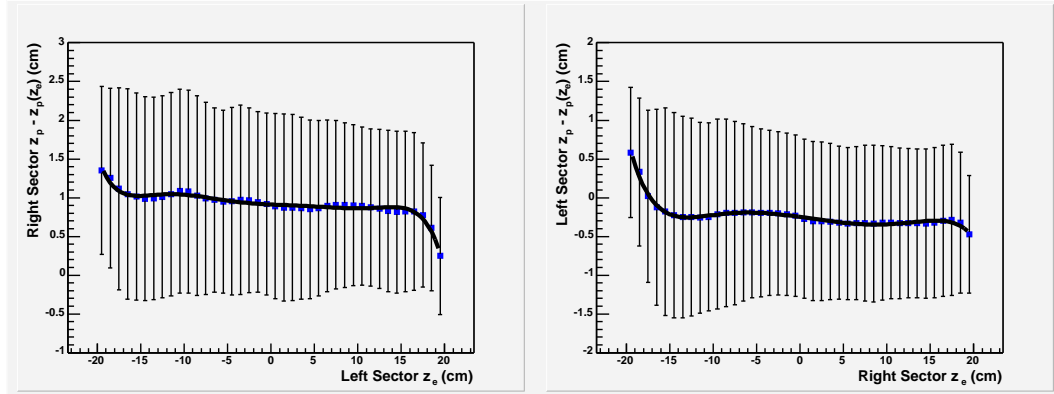


Figure 4-12: Difference z_p and z_e . This difference was binned and fitted to a Gaussian in each bin, with a mean μ and RMS σ extracted for each bin. These μ and σ values were then fitted to polynomials in z_e . Left (right) column of plots corresponds to electrons scattered in the left (right) and protons scattered in the right (left) sector of BLAST.

variables formed above was fitted to a Gaussian in each bin, and a mean μ and RMS σ was extracted for each bin. These μ and σ values were then fitted to polynomials in θ_e , θ_p , θ_e , ϕ_e and z_e respectively. A few polynomials of different degrees were tried with little variation in results. In the above figures 7th degree polynomials were used (shown as the black curves passing through the blue dots representing the μ values, with the σ magnitudes represented by the vertical bars). Rejecting events more than 2σ or 3σ away from the interpolated μ values made little difference. A 3σ cut was used for the final analysis.

Čerenkov and Timing Cuts

Čerenkov cuts simply require the Čerenkov box in front of the firing time-of-flight detector to fire as well. While Čerenkov cuts had basically no impact in the wire chamber region where a very good event selection had already been done by the polynomial kinematic cuts described in the previous subsection, they proved to be very helpful in the BAT region, differentiating between π^- and electrons. Čerenkov cuts were thus only used for the two boxes on which the BATs were mounted.

Timing cuts based on time-of-flight and coplanarity of e-p elastic events can be inferred

from the TOF scintillator information like that shown in Figure 4-13 for the case of BAT events. For each pair of TOFs (or, in case of a BAT event, a TOF and a BAT) firing, we

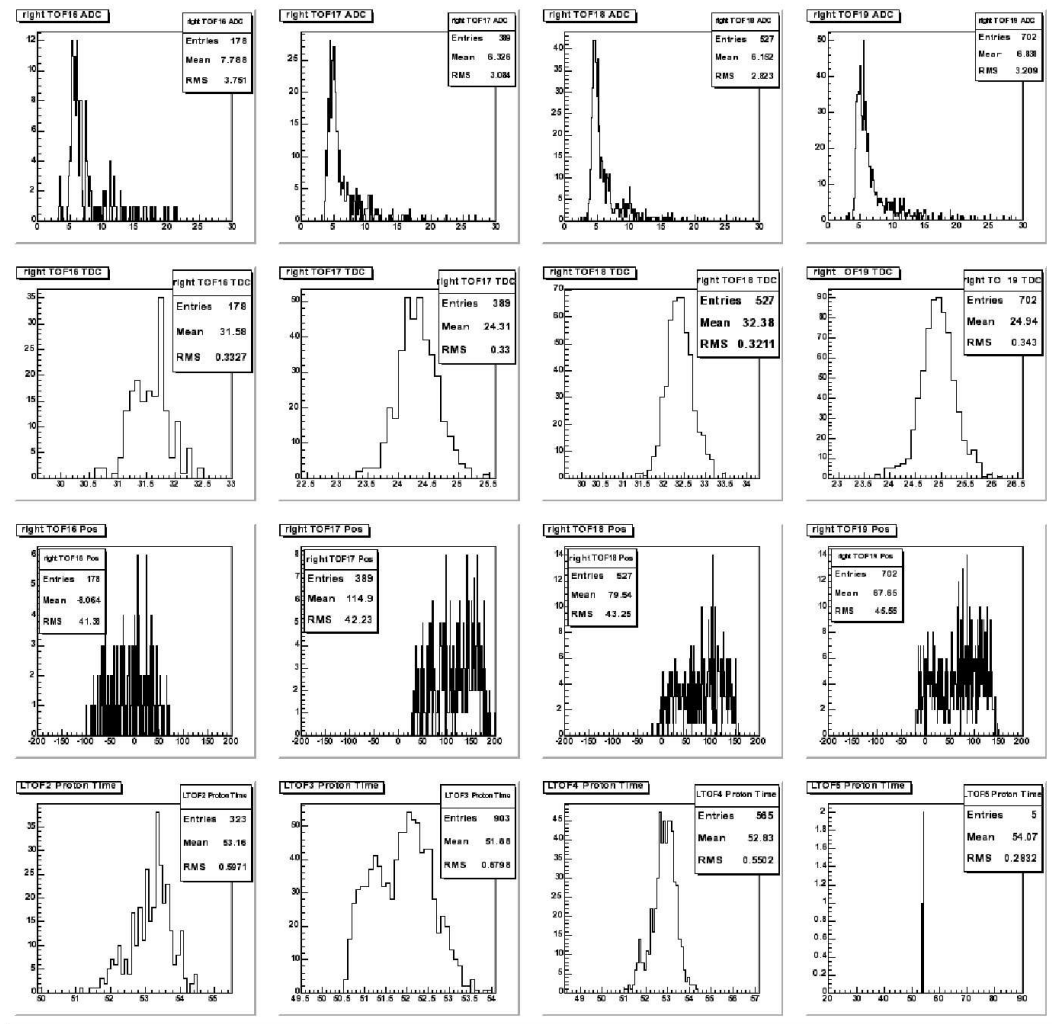


Figure 4-13: Example of BAT event information from the TOF and BAT detectors. ADC (first row), time-of-flight (second row) and position information (third row) for the right sector BATs is shown. The last row of plots shows time-of-flight information for the corresponding protons in the forward TOFs of the left sector

can form the TDC combinations

$$TOF = \frac{Left_{TOP} + Left_{BOTTOM}}{2} - \frac{Right_{TOP} + Right_{BOTTOM}}{2} \quad (4.2)$$

and

$$POS = (Left_{TOP} - Left_{BOTTOM}) + (Right_{TOP} - Right_{BOTTOM}) \quad (4.3)$$

representing the proton timing and coplanarity information respectively.

It was noted that once the polynomial kinematic wire chamber cuts from the previous

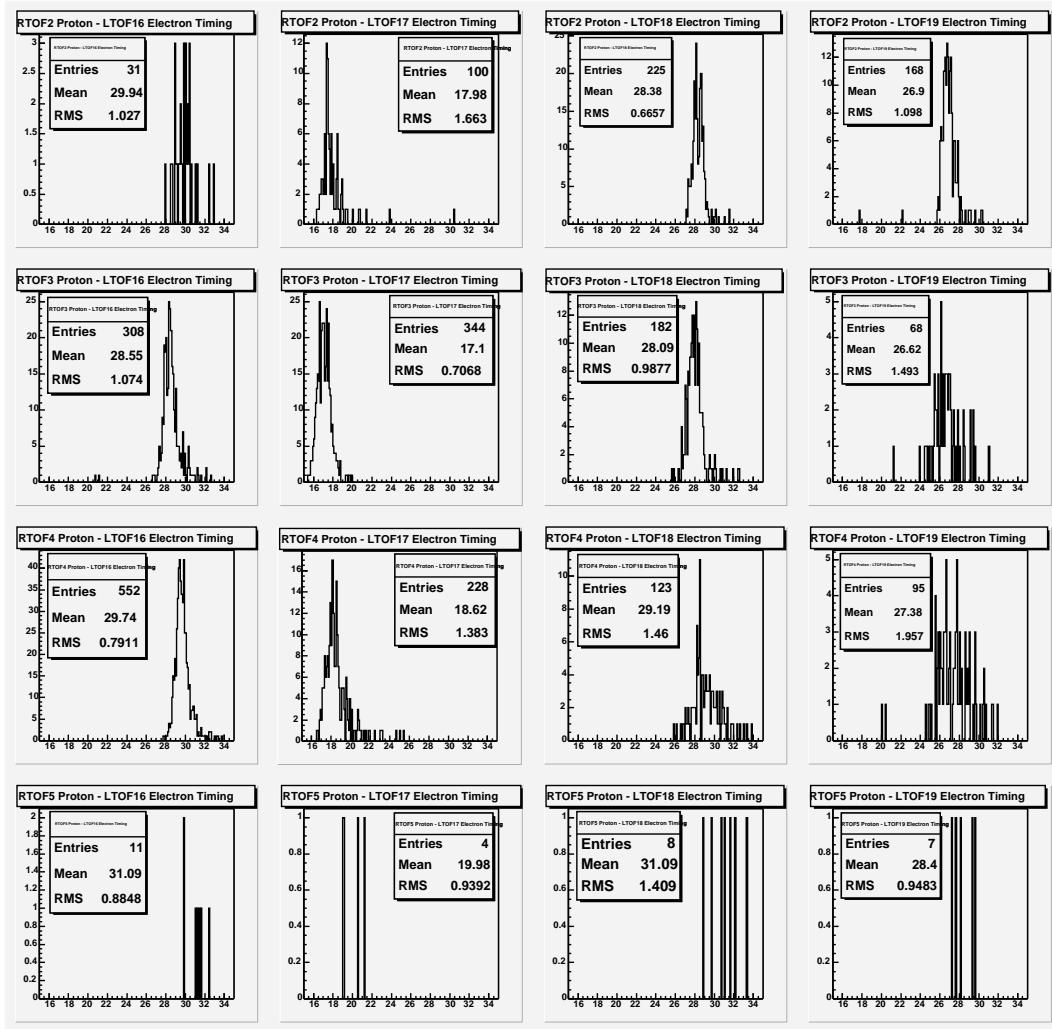


Figure 4-14: Difference of the proton and BAT electron time of flight on a detector pair-by-pair basis, before cuts were applied

paragraph were defined, the timing cuts in the region covered by the wire chambers made

basically no difference so they were not used in the final analysis. This is consistent with the design of BLAST, where the triggering purpose of the TOF system was just to provide the wire chambers with a proton timing independent of the flight path.

Timing cuts in the BAT region (outside the wire chamber acceptance) proved to be

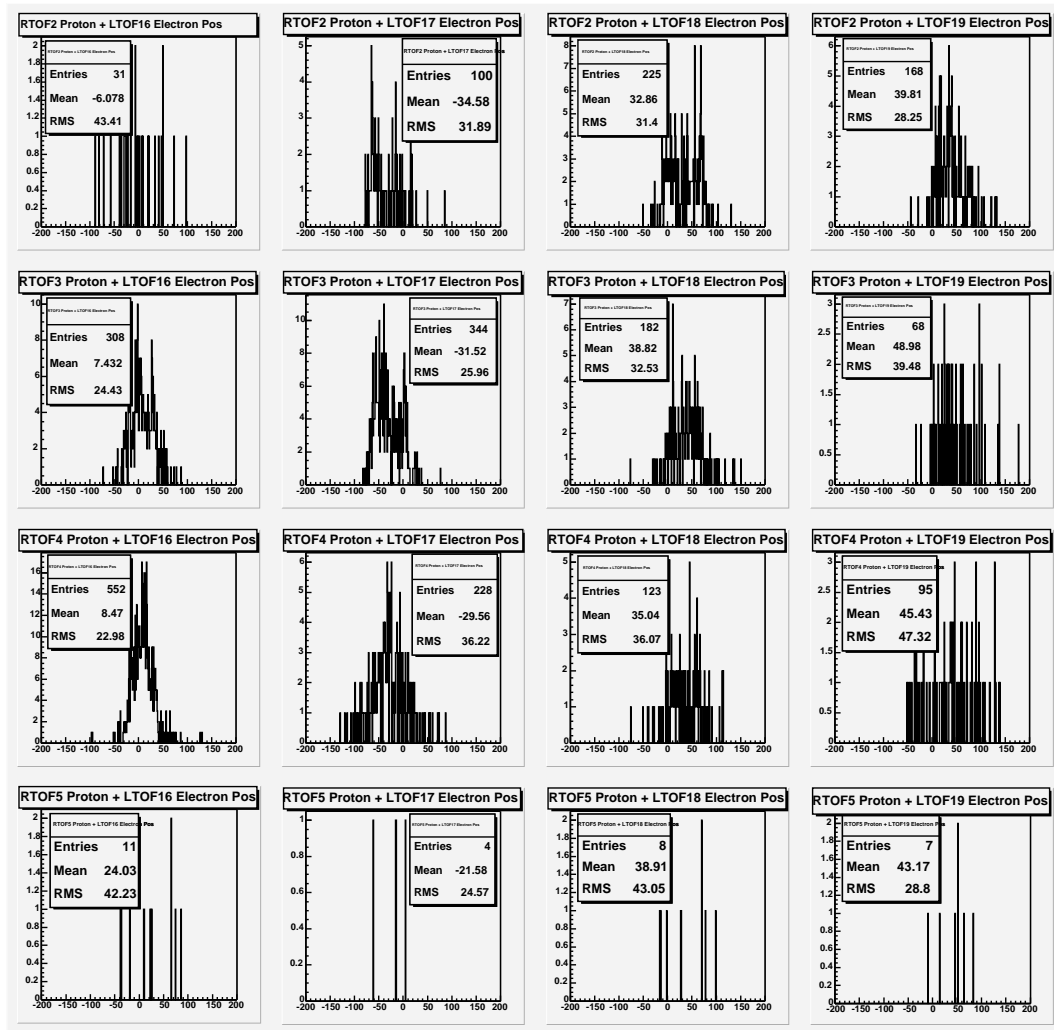


Figure 4-15: Sum of the proton and BAT electron position on a detector pair-by-pair basis, before cuts were applied

very important, as only proton track information was available in this case. A selection equivalent to a 2σ cut on the above *TOF* and *POS* variables defined for corresponding

TOF-BAT pairs was used for the BAT analysis.

The difference between the proton time-of-flight and corresponding BAT electron time-of-flight described by the above TOF variable is shown on a detector pair-by-pair basis in Figure 4-14. The different values of these differences are due to different offsets for individual TDC channels. The proton and corresponding BAT electron position information described by the above POS variable is shown on a detector pair-by-pair basis in Figure 4-15. At the time of this writing, a BAT recalibration is being performed and a new version of the ep_skim data summary tape with improved BAT time-of-flight and position information is being created. This will help BAT event selection and might help avoid the Čerenkov cuts, which drastically reduce the number of BAT events (almost by a factor of 4).

Other BAT Cuts

For the BAT events, a 2σ cut on the proton β (which comes from time-of-flight information) was further applied for both sectors. Figure 4-16 shows the reconstructed

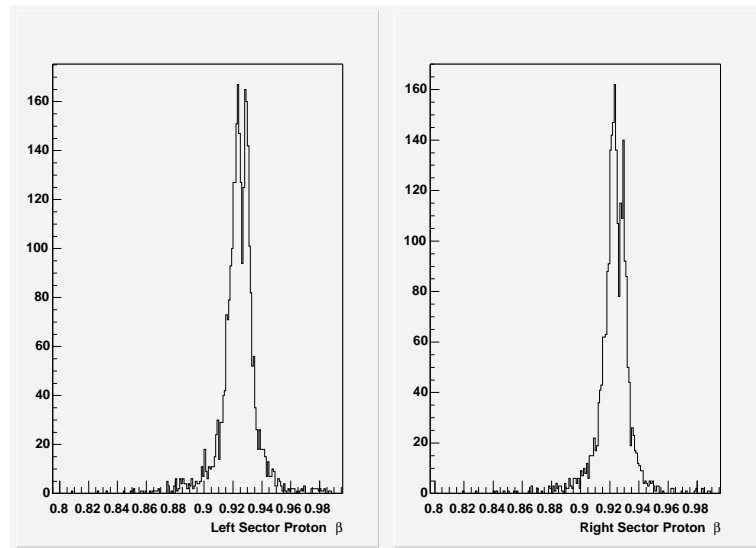


Figure 4-16: Proton β before cuts for BAT events

proton β before any BAT cuts were implemented.

A cut on the reconstructed proton mass $0.28(\text{GeV}/c^2) < M_p < 0.52(\text{GeV}/c^2)$ was

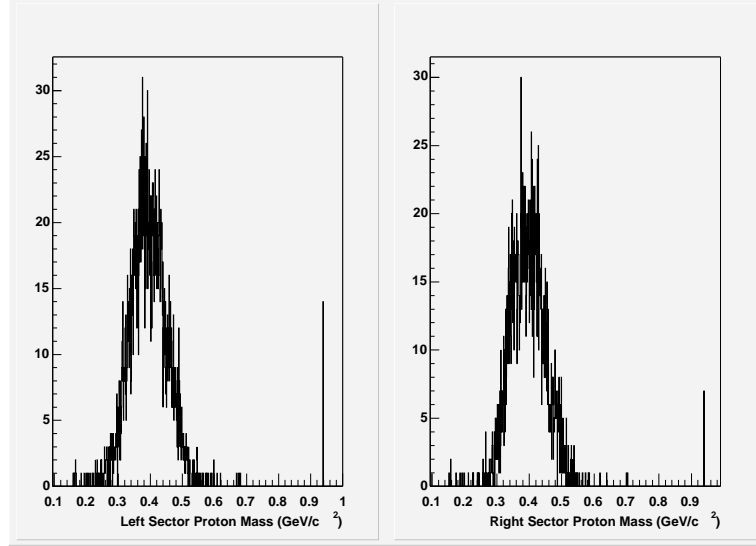


Figure 4-17: Proton mass before cuts for BAT events

also required. This was equivalent to a 2σ cut on the reconstructed proton mass, which contains time-of-flight, path length and momentum information. The range of the reconstructed proton mass reflects the fact these were fast protons corresponding to the high Q^2 region of the BATs. Figure 4-17 shows the reconstructed proton mass before these cuts were implemented.

4.2 Quality of the Data

Those events that survive all of the aforementioned cuts are used in a check of the data quality. The final number of elastic events was 5,143,070, out of which 2,451 were BAT events. In Figure 4-7(b) we see the invariant mass spectrum after all the elastic cuts. The gaussian distribution roughly centers on $M_p = 0.938\text{GeV}/c^2$ and gives confidence that a

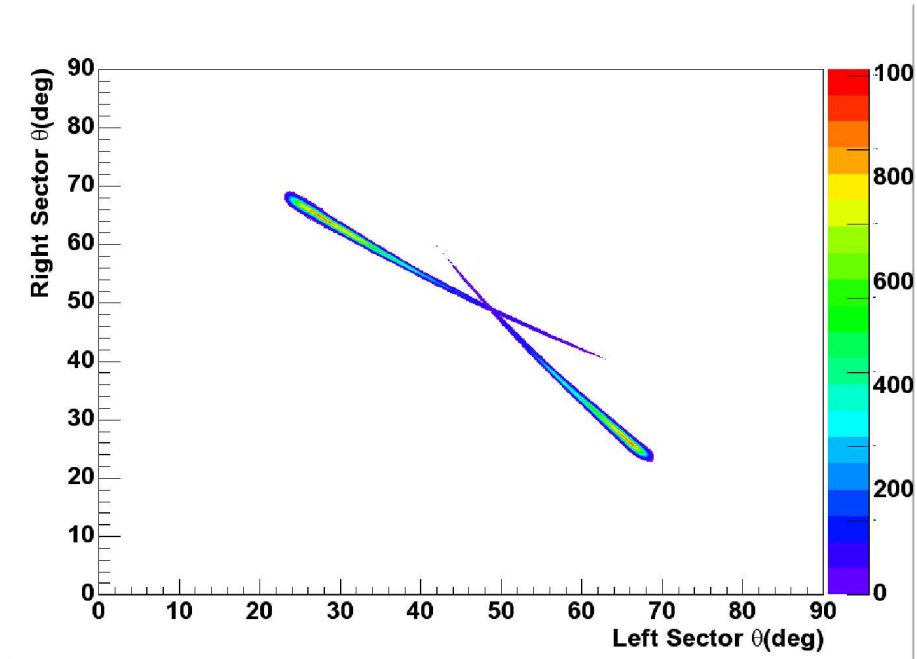


Figure 4-18: The measured polar angles θ_R vs. θ_L following implementation of elastic cuts

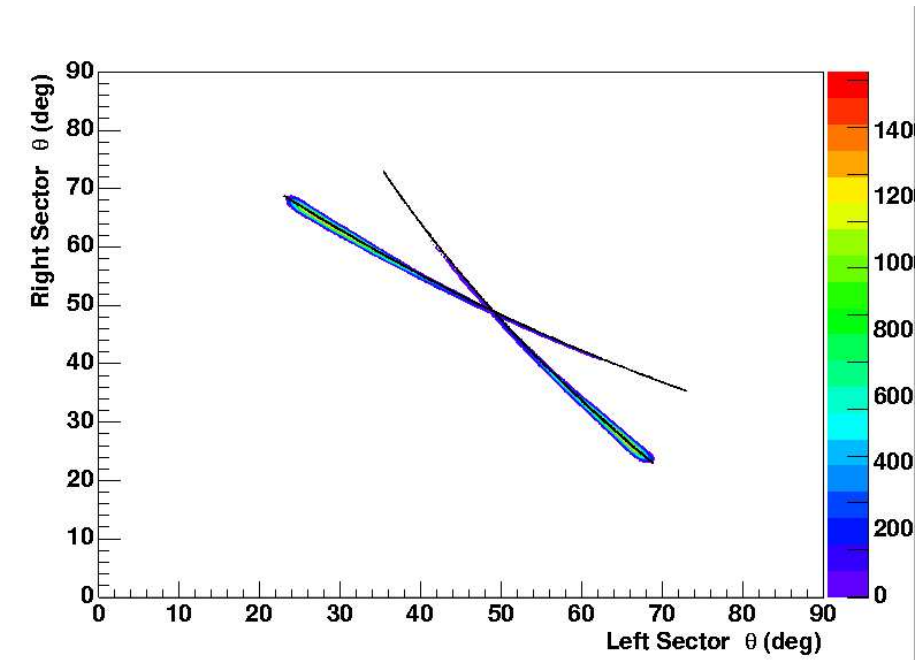


Figure 4-19: The measured polar angles θ_R vs. θ_L following implementation of elastic cuts. The red lines represent the proton polar angle as calculated from the electron polar angle $\theta_p(\theta_e)$ using the kinematics of elastic scattering

good selection of elastic events has been made. This is further reinforced by the good agreement of the predicted measured polar angles θ_L and θ_R for particles entering the left and right sector of BLAST respectively. Measured values of θ_R versus θ_L are shown in Figure 4-18. Figure 4-19 shows the same measured values of θ_R versus θ_L superimposed on the proton polar angle as calculated from the electron polar angle $\theta_p(\theta_e)$ using the kinematics of elastic scattering.

Figure 4-20 (to be compared with Figure 4-6 produced before any cuts were applied) shows the difference between the reconstructed electron momentum and the electron momentum calculated using electron polar angle θ track information after all elastic cuts were implemented.

An example of a reconstructed elastic event is shown in Figure 4-21. The common

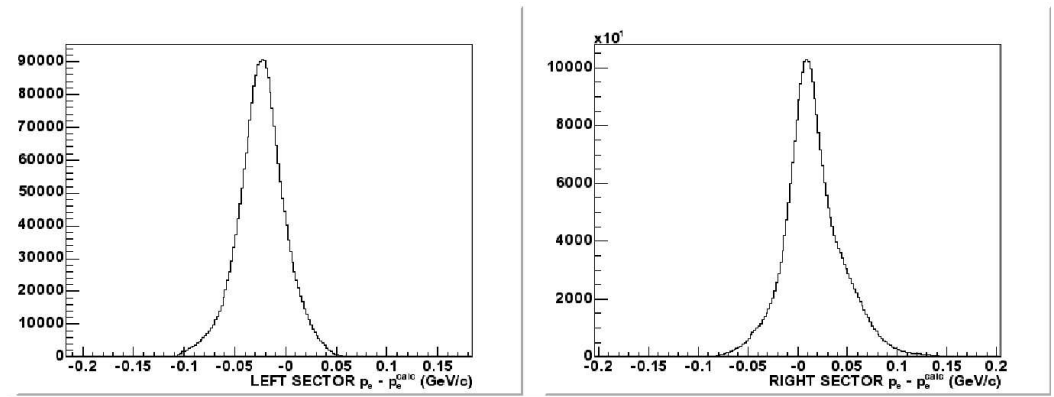


Figure 4-20: Difference between reconstructed electron momentum and electron momentum calculated from elastic kinematic relations after elastic cuts were implemented

vertex and correlation of forward and backward angles with the charge of the particles are characteristic of an elastic event. The inbending track in the forward angle is the electron. Note that the Čerenkov box corresponding to this track has fired. The backward angle track that is outbending is the proton. Figure 4-22 shows the upstream view of the same event. One can see in this picture that the tracks are nearly coplanar.

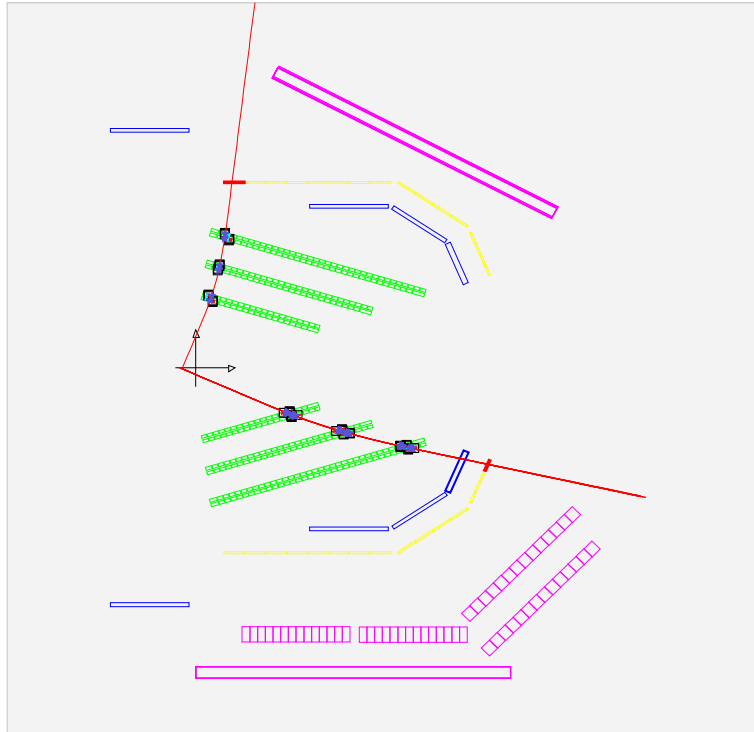


Figure 4-21: Reconstructed Elastic Event TOP View

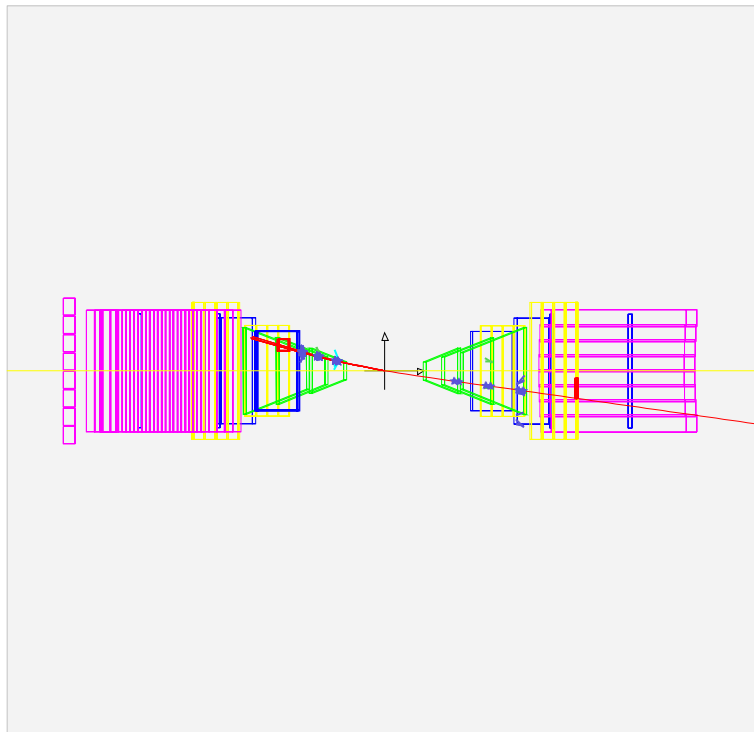


Figure 4-22: Reconstructed Elastic Event Upstream View

The total yield for each run normalized to the collected beam charge is shown in Figure 4-23. The small variations reflect changes in the thickness of the ABS target.

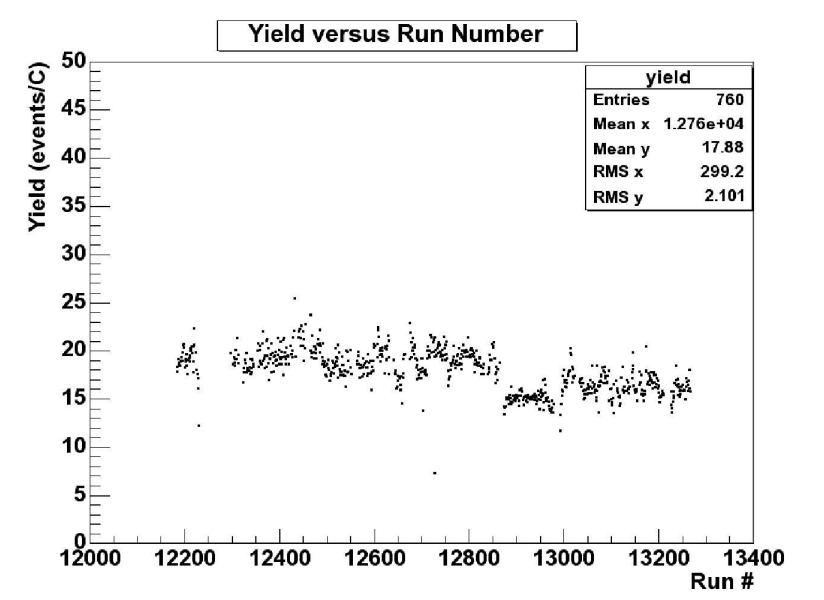


Figure 4-23: Total yield for each run, normalized by collected beam charge. The yield is plotted after all the elastic cuts were implemented

4.3 BLAST Monte Carlo

Monte Carlo simulations of elastic electron-proton events in the BLAST detector were created with the code *blastmc* which was based on GEANT 3.21 written in Fortran. An event generator, *DGen*, which was written in C++ for both the hydrogen and deuterium experiments, simulated various electron scattering processes including the e-p elastic channel. These simulations accounted for energy loss and multiple scattering of the scattered particles. The Hoehler parametrization [56] of the world data on the proton elastic form factors $G_E(Q^2)$ and $G_M(Q^2)$ was used as the input to the elastic cross section.

The simulated events were written to a CODA format file and the Monte Carlo data

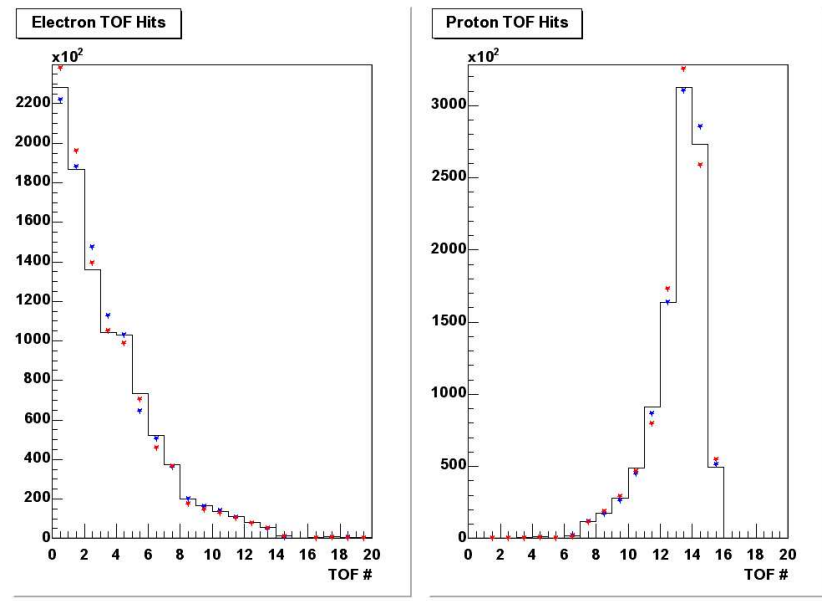


Figure 4-24: Comparison between the Monte Carlo TOF and BAT yields (black line) and the corresponding yields for real data. The left sector TOFs and BATs are illustrated by the blue dots, while the red dots depict the right sector TOF and BAT yields. All yields have been normalized to the integral of counts. Note the good agreement between the real data and the Monte Carlo shapes.

were analyzed in the same manner as the real data. The vertex was generated with a triangular distribution function to follow the measured target density distribution [75]. In our analysis eight million Monte Carlo events were generated.

Figure 4-24 shows a comparison between the Monte Carlo TOF and BAT yields and the corresponding yields for real data. Note the good agreement between the real data and the Monte Carlo shapes. The small differences between the left and right sectors can be explained by variations of the detectors' efficiency.

CHAPTER 5

RESULTS AND DISCUSSION

5.1 The Experimental Beam-Target Asymmetry

Beam helicity, flipped once per fill (10-15 minutes), and target state, which was changed several times per fill (every 5 minutes), were digitized on an event by event basis [75]. These data were also written to scalers along with the accumulated beam-charge collected for each state.

One can form a beam-target asymmetry A_{ep} from the above states in terms of the cross section measured for each combination of beam and target polarization. The four possible cross sections $\sigma(b, t)$ are summed to yield the total cross section σ_0 .

$$\sigma_0 = \sigma(+, +) + \sigma(-, +) + \sigma(+, -) + \sigma(-, -) \quad (5.1)$$

The beam-target vector asymmetry is

$$A_{ep} = \frac{1}{P_b P_t} \frac{1}{\sigma_0} [\sigma(+, +) - \sigma(-, +) - \sigma(+, -) + \sigma(-, -)] \quad (5.2)$$

where P_t is the polarization of the target defined by

$$P_t = n_+ - n_- \quad (5.3)$$

where n_{\pm} are the numbers of protons in the state \pm . In practice, it is number of counts and not a pure cross section that is measured. To ensure proper normalization by charge, we define

$$\sigma_i(b, t) \equiv N_i \frac{\bar{q}}{q_i} \quad (5.4)$$

where N_i and q_i are the number of counts and the collected charge in state i and \bar{q} is the average charge for each state.

$$\bar{q} \equiv \sum_i^4 \frac{q_i}{4} \quad (5.5)$$

Fast reversal of the target spin minimizes systematic errors in the asymmetries that might come from slow drifts of the beam and target polarizations, or detector response. Reversing both beam and target polarizations allows for cross-checks of systematics.

The beam-target asymmetries for the left and right BLAST sectors are shown in Table 5.1. Figure 5-1 also shows the experimental asymmetries measured for electrons scat-

$Q^2 \left[\frac{\text{GeV}}{c} \right]^2$	A_{LEFT}^{ep}	$\delta A_{LEFT} (stat.)$	A_{RIGHT}^{ep}	$\delta A_{RIGHT} (stat.)$
0.162	-0.0822439	0.00156608	-0.103906	0.00139950
0.191	-0.0977354	0.00145642	-0.119737	0.00145171
0.232	-0.1139630	0.00169117	-0.142963	0.00167611
0.282	-0.1371850	0.00221724	-0.176246	0.00200366
0.344	-0.1683840	0.00267666	-0.208463	0.00251477
0.420	-0.1992540	0.00318846	-0.240358	0.00326356
0.498	-0.2284040	0.00400841	-0.266641	0.00403819
0.586	-0.2555280	0.00592675	-0.292102	0.00551783
0.836	-0.2855730	0.02947970	-0.320605	0.02539450

Table 5.1: A_{ep} : $\theta_T = 47.1^\circ$, $P_b P_t = 0.52$, Charge = 294 kC

tered into the left and right sectors of BLAST, respectively. Each sector was fit to the Hoehler parametrization to extract the product of beam and target polarizations $P_b P_t$ (so called *dilution factor*). The very good agreement of the determination of the dilution

factor in the two sectors gives confidence in the measurement of the target holding field. The Hoehler parametrization was selected because it was the best parametrization of the

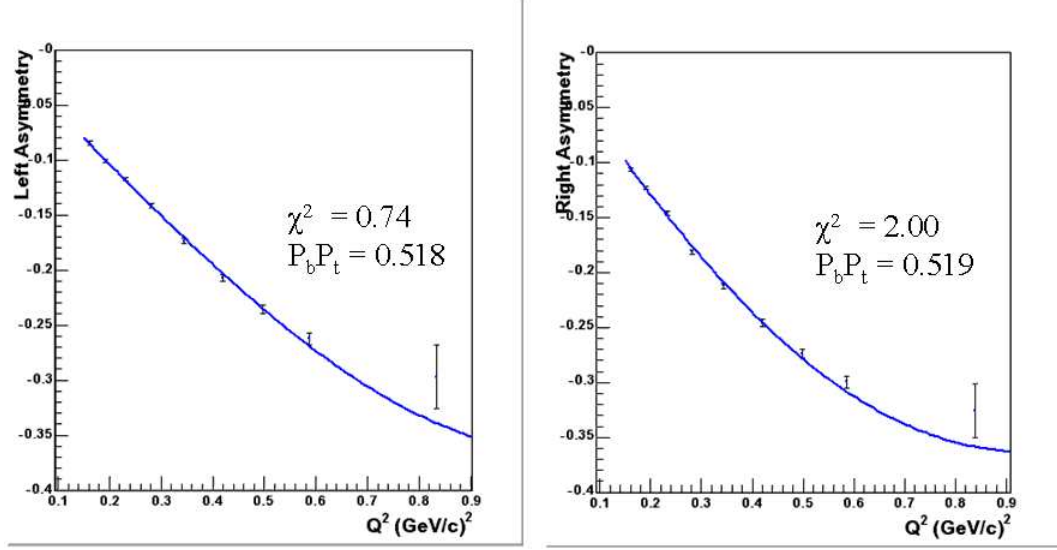


Figure 5-1: The experimental asymmetries measured for electrons scattering into the left and right sectors of BLAST. Each sector was fit to the Hoehler parametrization to extract the product of beam and target polarizations $P_b P_t$, which is consistent in the two sectors. Note the very good χ^2 values of the fit as well

form factors in the Q^2 region of our experiment. After Hoehler's parametrization in 1976, most of the world's data was taken at higher Q^2 . However, this parametrization was used just as a systematic check of the data so its impact on our analysis is minimal.

5.2 Super Ratio Method

A determination of the ratio $\frac{\mu G_E^p}{G_M^p}$, independent of the knowledge of the beam and target polarizations can be precisely obtained by measuring the super ratio

$$R = \frac{A_L}{A_R} = \frac{2\tau v_{T'} \cos\theta_1^* G_M^2 - 2\sqrt{2\tau(1+\tau)} v_{TL'} \sin\theta_1^* \cos\phi_1^* G_M G_E}{2\tau v_{T'} \cos\theta_2^* G_M^2 - 2\sqrt{2\tau(1+\tau)} v_{TL'} \sin\theta_2^* \cos\phi_2^* G_M G_E} \quad (5.6)$$

where $v_{T'}$ and $v_{TL'}$ are kinematic factors defined as

$$v_{T'} = \tan\left(\frac{\theta}{2}\right) \sqrt{\frac{Q^2}{|\mathbf{q}|^2} + \tan^2\left(\frac{\theta}{2}\right)} \quad (5.7)$$

$$v_{TL'} = -\frac{1}{\sqrt{2}} \frac{Q^2}{|\mathbf{q}|^2} \tan\left(\frac{\theta}{2}\right) \quad (5.8)$$

and A_L and A_R are the elastic ep scattering asymmetries measured in the left and right sectors of BLAST respectively, as described in the previous section. From the above formula, the form factor ratio $\frac{\mu G_E^p}{G_M^p}$ can be extracted, after calculating the corresponding kinematic factors and the angles θ^* and ϕ^* for each data point.

To obtain θ^* and ϕ^* for the extraction of the form factor ratio, two rotations in 3-space must be conducted [79]. To illustrate this consider the target spin unit vector in the BLAST frame, \hat{S}^B , as shown in Figure 5-2.

$$\hat{S}^B = \begin{pmatrix} \hat{x}^B \\ \hat{y}^B \\ \hat{z}^B \end{pmatrix} \rightarrow \begin{pmatrix} \sin \theta_T \\ 0 \\ \cos \theta_T \end{pmatrix} \quad (5.9)$$

The scattering frame has the x and z axes coplanar with the beam axis, the scattered electron momentum vector, and the three momentum vector \mathbf{q} . To transform from the BLAST frame to the scattering frame we rotate about the z-axis (i.e. the beam axis) by the angle of azimuth ϕ_e with the matrix

$$R_z^{SC}(\phi_e) = \begin{pmatrix} \cos \phi_e & \sin \phi_e & 0 \\ -\sin \phi_e & \cos \phi_e & 0 \\ 0 & 0 & 1 \end{pmatrix} \quad (5.10)$$

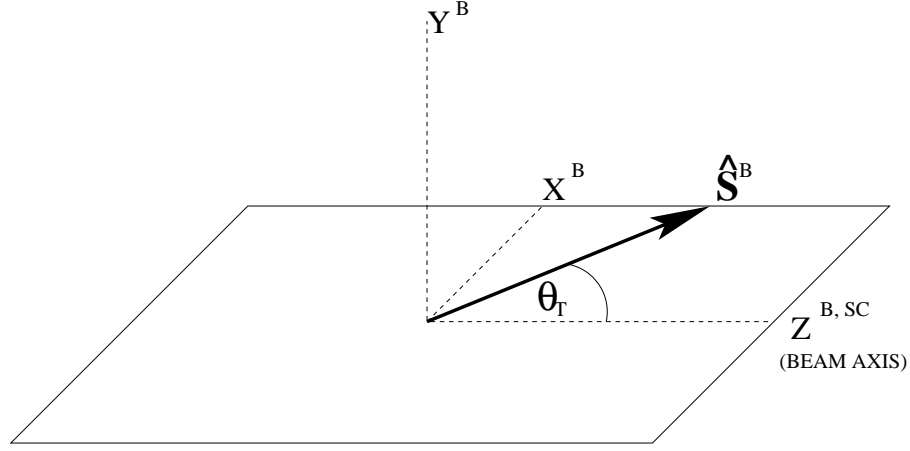


Figure 5-2: The BLAST Frame

As shown in Figure 5-3, the spin vector in the scattering frame is then

$$\hat{S}^{SC} = R_z^{SC}(\phi_e)\hat{S}^B = \begin{pmatrix} \cos \phi_e \sin \theta_T \\ \sin \phi_e \sin \theta_T \\ \cos \theta_T \end{pmatrix} \quad (5.11)$$

To go from the scattering frame to the physics (or Q) frame one needs a rotation around the y-axis of the scattering frame by the angle θ_q aligning the z-axis with the \mathbf{q} -vector. This is shown in Figure 5-4.

$$\hat{S}^Q = R_y^Q(\theta_q)\hat{S}^{SC} = \begin{pmatrix} \cos \theta_q \cos \phi_e \sin \theta_T + \sin \theta_q \cos \theta_T \\ -\sin \phi_e \sin \theta_T \\ -\sin \theta_q \cos \phi_e \sin \theta_T + \cos \theta_q \cos \theta_T \end{pmatrix} = \begin{pmatrix} \hat{S}_x^Q \\ \hat{S}_y^Q \\ \hat{S}_z^Q \end{pmatrix} \quad (5.12)$$

From Figure 2-1 we see that we can write

$$\begin{pmatrix} \hat{S}_x^Q \\ \hat{S}_y^Q \\ \hat{S}_z^Q \end{pmatrix} = \begin{pmatrix} |\hat{S}^Q| \sin \theta^* \cos \phi^* \\ |\hat{S}^Q| \sin \theta^* \sin \phi^* \\ |\hat{S}^Q| \cos \theta^* \end{pmatrix} \quad (5.13)$$

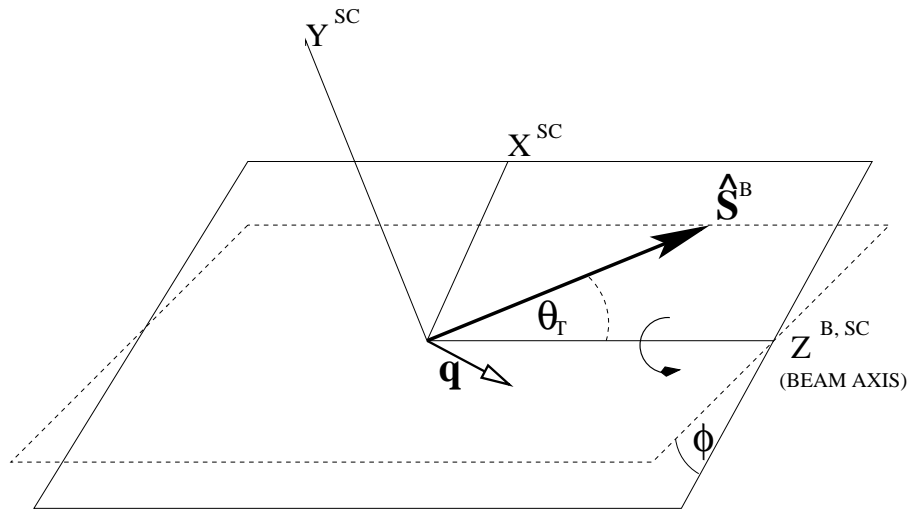


Figure 5-3: Rotating from the BLAST to Scattering Frame

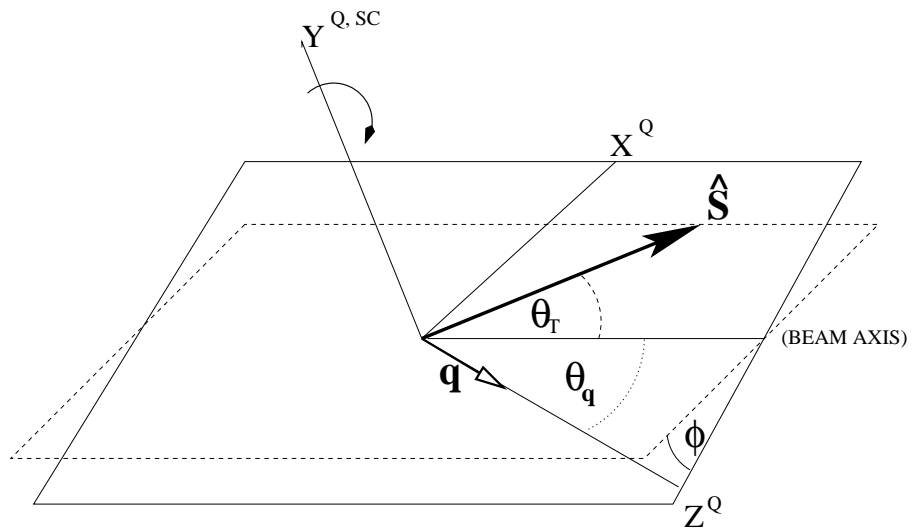


Figure 5-4: Rotating from the Scattering Frame to the Q (Physics) Frame

From this we can obtain θ^* and ϕ^* in terms of BLAST variables:

$$\theta^* = \cos^{-1} \left(\frac{S_z^Q}{|\hat{S}^Q|} \right) = \cos^{-1}(\cos \theta_{\mathbf{q}} \cos \theta_T - \sin \theta_{\mathbf{q}} \cos \phi_e \sin \theta_T) \quad (5.14)$$

$$\phi^* = \sin^{-1} \left(\frac{S_y^Q}{|\hat{S}^Q| \sin \theta^*} \right) = \sin^{-1} \left(\frac{-\sin \phi_e \sin \theta_T}{\sin \theta^*} \right) \quad (5.15)$$

For the case of elastic scattering, $\theta_{\mathbf{q}}$ is given in terms of θ_e by equations 2.7 and 2.8. Once the mean value of Q^2 was determined for each bin, θ^* was calculated using 5.14 based on this mean value of Q^2 . The angle ϕ^* was then obtained using this value of θ^* as well as the mean value of the azimuthal angle ϕ_e .

From the formula of the super ratio, $\frac{G_E^p}{G_M^p}$ is obtained:

$$\frac{G_E^p}{G_M^p} = \frac{\tau v_{T'} \cos \theta_2^* A_L - \tau v_{T'} \cos \theta_1^* A_R}{A_L \sqrt{2\tau(1+\tau)} v_{TL'} \sin \theta_2^* \cos \phi_2^* - A_R \sqrt{2\tau(1+\tau)} v_{TL'} \sin \theta_1^* \cos \phi_1^*} \quad (5.16)$$

The results for the form factor ratio $\frac{\mu G_E^p}{G_M^p}$ are shown in Table 5.2. Figure 5-5 also shows

$Q^2 \left[\frac{\text{GeV}}{c} \right]^2$	$\mu G_E^p / G_M^p$	$\delta \mu G_E^p / G_M^p$ (stat.)
0.162	0.975	0.022
0.191	1.007	0.019
0.232	0.989	0.017
0.282	0.949	0.017
0.344	0.968	0.017
0.420	0.967	0.018
0.498	0.976	0.021
0.586	0.943	0.028
0.836	0.871	0.159

Table 5.2: $\mu G_E^p / G_M^p$

the form factor ratio $\frac{\mu G_E^p}{G_M^p}$ obtained by the super-ratio method.

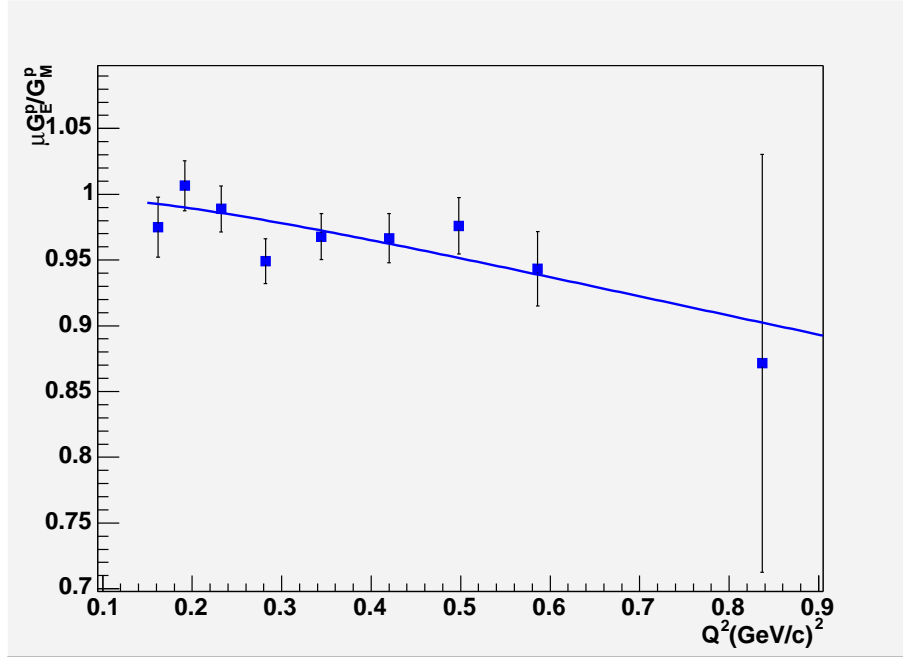


Figure 5-5: $\frac{\mu_{G_E^p}}{G_M^p}$ as a function of Q^2 . The blue line is the Hoehler parametrization. The last data point was measured using the BATs and was outside of the wire chamber coverage

5.3 Systematic Errors

The biggest contributions to the systematic errors come from the determination of Q^2 and of the target spin angle β . At the time of writing this thesis, a more thorough attempt of improving these uncertainties by new calibrations and measurements is being made. These systematic checks are described in this section.

5.3.1 Q^2 Determination

In an e-p elastic reaction, there are four independent ways of determining Q^2 , using either the polar angles θ_e or θ_p of the electron or proton respectively, or either one of their momenta (p_e or p_p). Because the angle resolution provided by the wire chambers was much better than the momentum resolution, only the polar angles were used to determine Q^2 for the present work. As seen in Figure 5-6, there is a slight discrepancy in the determination of Q^2 by using θ_e or θ_p . The average of the two Q^2 values histogrammed in both sectors

at the same time was used in our final analysis.

The error in the form factor ratio is obtained by comparing extractions of $\mu G_E^p/G_M^p$

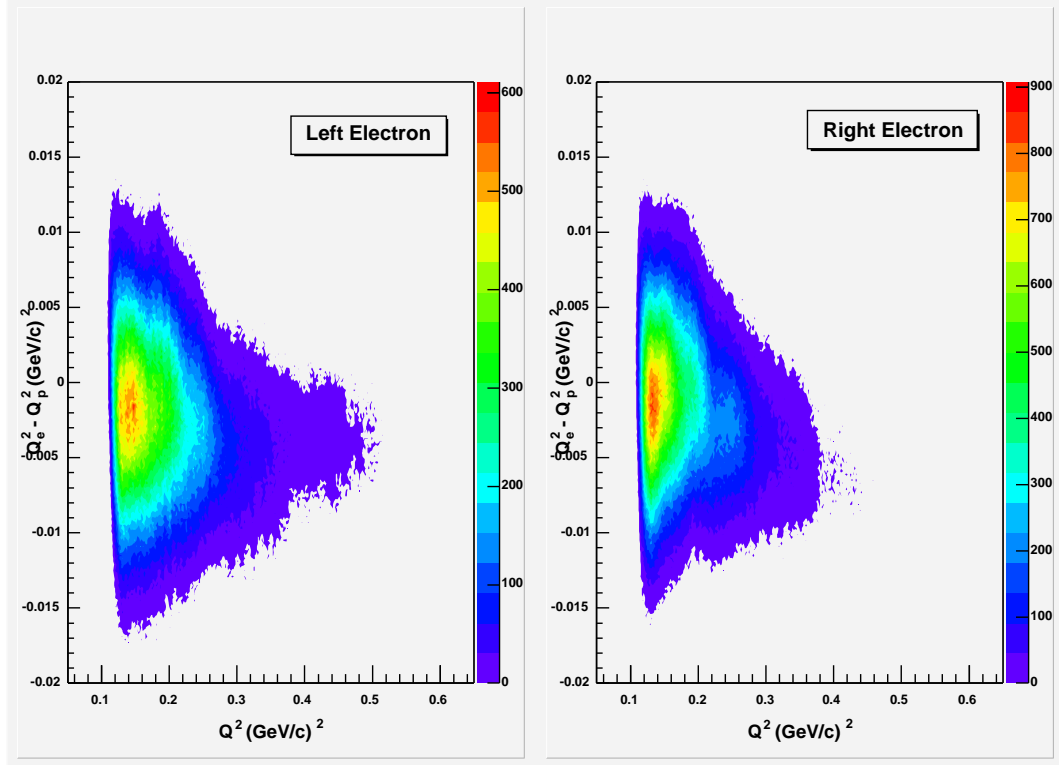


Figure 5-6: The difference in the determination of Q^2 from the electron or proton polar angles

using each of the above two determinations (θ_e or θ_p) of Q^2 . Table 5.3 shows the systematic errors caused by this Q^2 discrepancy. The largest error is obtained for the second Q^2 point and is conservatively assigned to all other data points when calculating the total systematic errors. At the time of writing this thesis, it is believed that small deviations from the nominal values of the wire chambers is the root cause of this effect. This is under investigation and the discrepancies will be further reduced after the error is corrected and an updated Data Summary Tape is created.

5.3.2 Target Spin Angle

A careful map of the target holding field was done using a 3-D Hall probe after the hydrogen production run. In our analysis, although physically dependent on the target spin angle, the asymmetries and super ratio are extracted without any assumed knowledge of it. The target spin angle only enters our analysis in the determination of $\mu G_E^p/G_M^p$ through the angles θ^* and ϕ^* (see equation 5.16). Since the target spin angle has no dependence on Q^2 (it only depends on target position z) the average target spin angle (47.1°) of the target holding field map over the vertex distribution was used in all Q^2 bins. The very good agreement of the beam-target polarization product obtained by the Hoehler fits to the asymmetries in the two sectors (see Figure 5-1) also increases our confidence in the average value of the target spin angle we used.

Due to geometric restrictions, the uncertainty in the target spin angle is estimated at 0.8° . At the time of writing this thesis, preparations are under way to redo the target holding field mapping to a precision of 0.1° by a new method used at JLab based on a compass principle, where the field angle is measured directly, as opposed to the previously used method of measuring longitudinal and transverse field amplitudes. The compass device is a magnetic probe (permanent magnet or magnetized iron) that sits on an air pillow and that can be sled along the z axis. A mirror is attached to the probe and the angle of the probe orientation is measured by the direction of the reflected light from a laser that sits on the axis. Through this method, our systematic errors will be greatly reduced. Table 5.3 shows the most important systematic error contributions to the form factor ratio $\frac{\mu G_E^p}{G_M^p}$.

$Q^2 \left[\frac{GeV}{c} \right]^2$	$\delta \left(\frac{\mu_{G_M^p}^{G_E^p}}{G_M^p} \right)_{spin \text{ angle and tracking}}^{syst}$	$\delta \left(\frac{\mu_{G_M^p}^{G_E^p}}{G_M^p} \right)_{e-p \text{ } Q^2 \text{ discrepancy}}^{syst}$	$\delta \left(\frac{\mu_{G_M^p}^{G_E^p}}{G_M^p} \right)_{total}^{syst}$
0.162	0.009	0.003	0.017
0.191	0.009	0.015	0.017
0.232	0.008	0.004	0.017
0.282	0.008	0.009	0.017
0.344	0.008	0.002	0.017
0.420	0.008	0.003	0.017
0.498	0.009	0.002	0.017
0.586	0.009	0.003	0.017
0.836	0.015	N/A	0.021

Table 5.3: The difference in the determination of Q^2 from the electron or proton polar angles for the left and right sectors of BLAST. The largest error is obtained for the second Q^2 point and is conservatively assigned to all other data points when calculating the total systematic errors. The last Q^2 point was only determined from the proton track information, as the BATs are outside wire chamber coverage

5.3.3 Tracking

Systematic shifts in the polar and azimuthal angles θ_e and ϕ_e are estimated to be of the order of 0.5° , as can be seen in Figures 4-10 and 4-11. Their contribution to the kinematic factors needed to determine the form factor ratio comes through the angles θ^* and ϕ^* which are defined as the polar and azimuthal angles between the target polarization vector and the direction of the three-momentum transfer \mathbf{q} and are described by equations 5.14 and 5.15.

The tracking contribution to the systematic errors is relatively small compared to the ones of the Q^2 discrepancy and target spin uncertainty. Tracking contribution is shown added in quadrature with the target spin contribution in Table 5.3.

5.3.4 False Asymmetries

Besides the beam-target asymmetry A_{ep} , one can form either beam or target single spin asymmetries from the four possible cross sections $\sigma(b, t)$:

$Q^2 \left[\frac{\text{GeV}}{c} \right]^2$	A_{LEFT}^{beam}	$\delta A_{LEFT}^{beam} (stat.)$	A_{RIGHT}^{beam}	$\delta A_{RIGHT}^{beam} (stat.)$
0.162	0.00638309	0.00157112	0.00382512	0.00140683
0.191	0.00588682	0.00146313	0.00709245	0.00146186
0.232	0.00662241	0.00170185	0.00461731	0.00169302
0.282	0.00467658	0.00223779	0.01217370	0.00203468
0.344	0.00638250	0.00271449	0.00968209	0.00257011
0.420	0.00476858	0.00325242	0.00468392	0.00336054
0.498	0.01062780	0.00411521	0.00773073	0.00418761
0.586	0.01425560	0.00612664	0.00961428	0.00576595
0.836	-0.0228452	0.03073560	-0.00805758	0.02679230

Table 5.4: Single spin beam asymmetry A^{beam} : $\theta_T = 47.1^\circ$, $P_b P_t = 0.52$, Charge = 294 kC

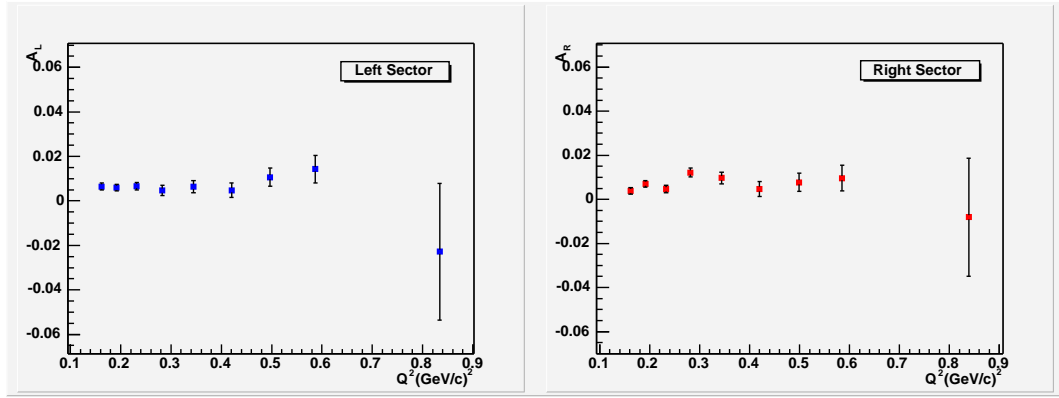


Figure 5-7: Beam single spin asymmetries

$$A_{beam} = \frac{\sigma(+,+) - \sigma(-,+) + \sigma(+,-) - \sigma(-,-)}{\sigma_0} \quad (5.17)$$

and

$$A_{target} = \frac{\sigma(+,+) + \sigma(-,+) - \sigma(+,-) - \sigma(-,-)}{\sigma_0} \quad (5.18)$$

where

$$\sigma_0 = \sigma(+,+) + \sigma(-,+) + \sigma(+,-) + \sigma(-,-) \quad (5.19)$$

The above two single spin asymmetries are independent measurements of false asymmetries. They could suggest undesired asymmetries in the polarizations of the two beam

or target states. Tables 5.4 and 5.5 show the values of the beam and target single spin asymmetries respectively. Figure 5-7 shows the single spin beam asymmetry, whereas Figure 5-8 depicts the single spin target asymmetry.

Both beam and target single-spin asymmetries are very small. Furthermore, they cancel to first order in the physics asymmetry and so have negligible systematic errors.

$Q^2 \left[\frac{\text{GeV}}{c} \right]^2$	A_{LEFT}^{target}	$\delta A_{LEFT}^{target} (stat.)$	A_{RIGHT}^{target}	$\delta A_{RIGHT}^{target} (stat.)$
0.162	-0.00346922	0.00157114	-0.003949060	0.00140682
0.191	-0.00474578	0.00146313	-0.002609510	0.00146188
0.232	-0.00658699	0.00170183	-0.000919145	0.00169304
0.282	-0.00274869	0.00223780	-0.002115410	0.00203482
0.344	-0.00648799	0.00271447	-0.008033470	0.00257012
0.420	-0.00730367	0.00325233	-0.006803320	0.00336046
0.498	-0.00128658	0.00411543	-0.007223780	0.00418758
0.586	-0.01464660	0.00612646	0.001286180	0.00576622
0.836	-0.00339710	0.03074350	-0.033809500	0.02677650

Table 5.5: Single spin target asymmetry A^{target} : $\theta_T = 47.1^\circ$, $P_b P_t = 0.52$, Charge = 294 kC

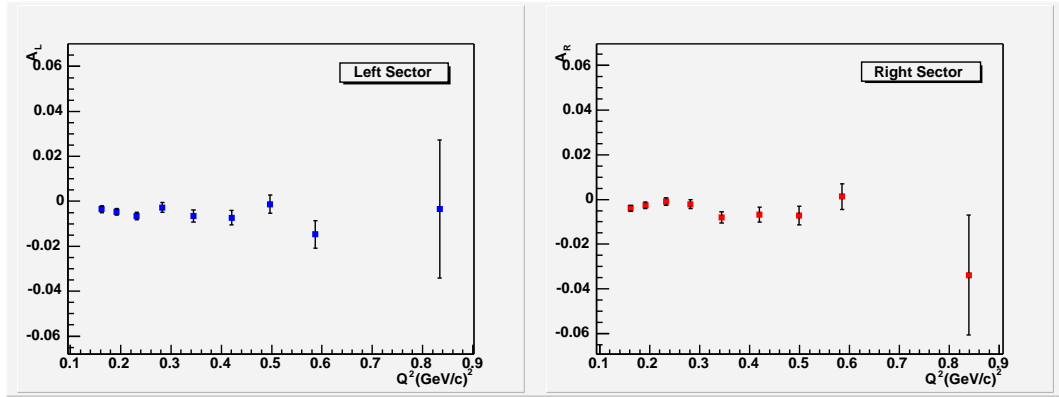


Figure 5-8: Target single spin asymmetries

5.3.5 Background Measurement

Since it is helicity independent, background can enter our asymmetries only as dilution. Background was measured under the same conditions as real data, but with an empty target instead of hydrogen (ABS gas flow turned off). The total integrated beam charge under empty target conditions that we used in our calculations was 14,882 kC. Only 2,323 events passed our elastic cuts (all in the region covered by the wire chambers). When scaled by the ratio of integrated charge between the two datasets of hydrogen data and empty target, this meant less than 0.9%. Furthermore, background cancels in the first order in the super ratio, so its effect on the extraction of $\frac{\mu G_E^p}{G_M^p}$ is negligible.

5.3.6 Radiative Corrections

A study of the radiative effects on the spin-dependent asymmetries was conducted by comparing the reconstructed unradiated Monte Carlo asymmetries with the reconstructed radiated Monte Carlo asymmetries. The radiated asymmetries were calculated by the code *MASCARAD* [91]. This code was chosen because it calculates spin-dependent radiative corrections.

Due to the finite energy resolution of particle detectors, any soft ($E_\gamma < \delta E_{detector}$) photons emitted by the incident or the scattered electron will not be detected. Furthermore, the virtual photons of vertex corrections can not be observed even by a detector with perfect resolution. Thus, true elastic scattering is not what is observed and the measured cross section is the elastic cross section scaled by some factor representing these radiative corrections.

Figure 5-9 shows a comparison between yields as a function of Q^2 for the three cases of real data (black), unradiated Monte Carlo (blue) and radiated Monte Carlo (red). 8M events were generated for each Monte Carlo case (unradiated and radiated). The yields

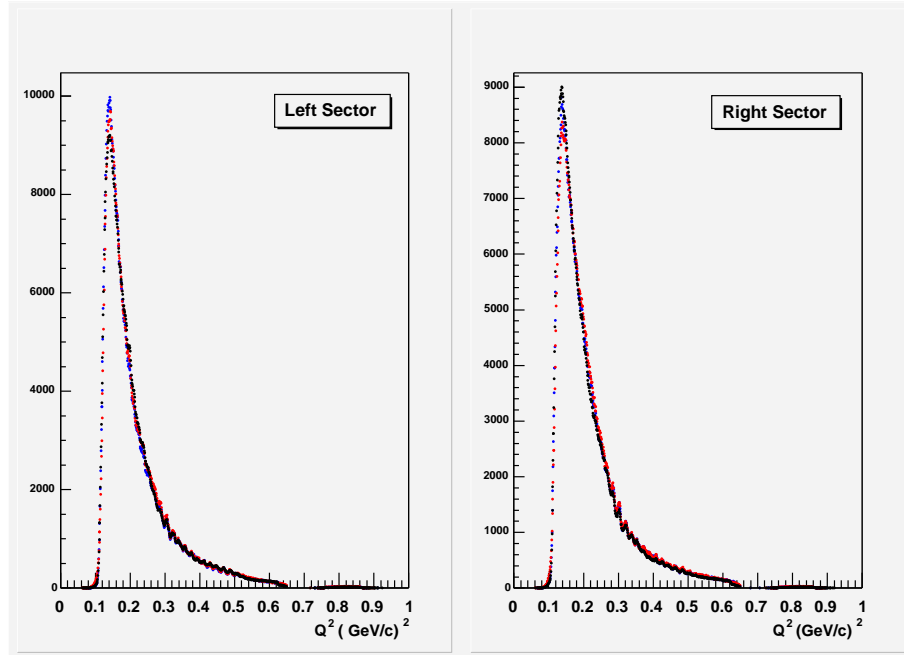


Figure 5-9: Comparison between yields as a function of Q^2 for the three cases of real data (black), unradiated Monte Carlo (blue) and radiated Monte Carlo (red)

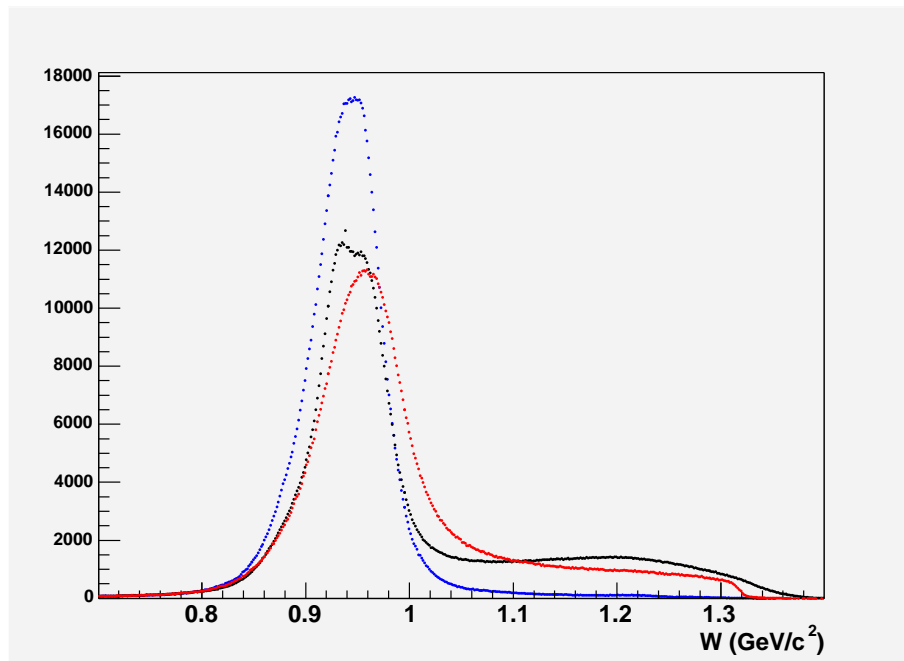


Figure 5-10: Invariant mass W spectrum for the three cases of real data (black), unradiated Monte Carlo (blue) and radiated Monte Carlo (red). No cuts are applied here, so there are some inelastic events in the real data spectrum. No momentum corrections are applied to the real data either

were normalized to the integral of counts. Note the excellent agreement of the three yield shapes.

Figure 5-10 shows the same comparison between yields as a function of the invariant

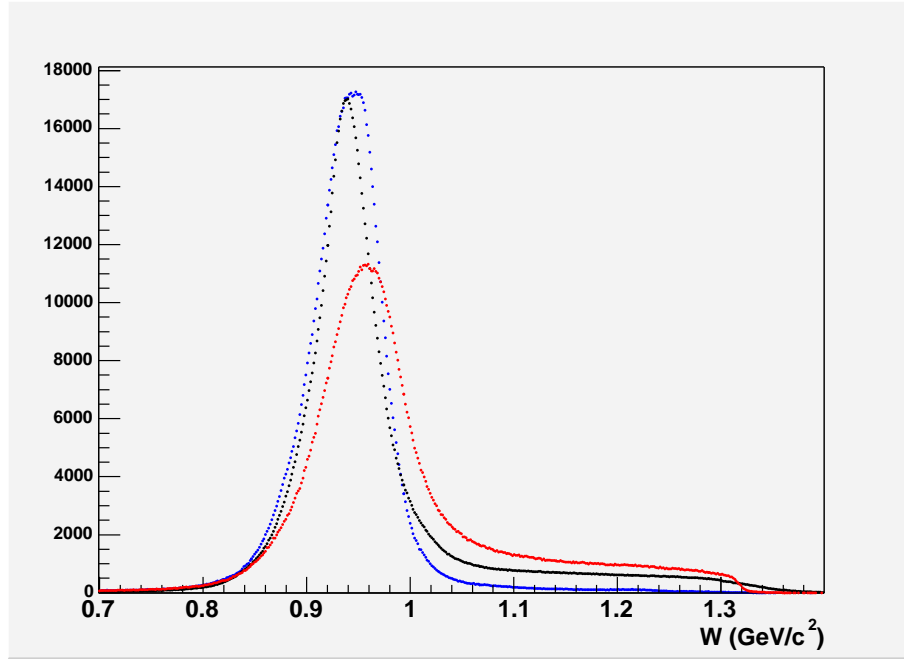


Figure 5-11: Invariant mass W spectrum for the three cases of real data (black), unradiated Monte Carlo (blue) and radiated Monte Carlo (red). Simple acceptance and vertex cuts, as well as momentum corrections, were applied to the real data

mass W for the three cases of real data (black), unradiated Monte Carlo (blue) and radiated Monte Carlo (red). The yields were normalized to the integral of counts. While the shift in W is expected for the radiated Monte Carlo case, momentum corrections can be applied to the real data spectrum. Figure 5-11 shows the same plots after these momentum corrections were applied. Figure 5-12 and Figure 5-13 show the difference between reconstructed momenta and momenta calculated from kinematic relations before (blue) and after (red) momentum corrections for electrons and protons respectively.

These corrections depend heavily on the improvement in wire chamber calibrations

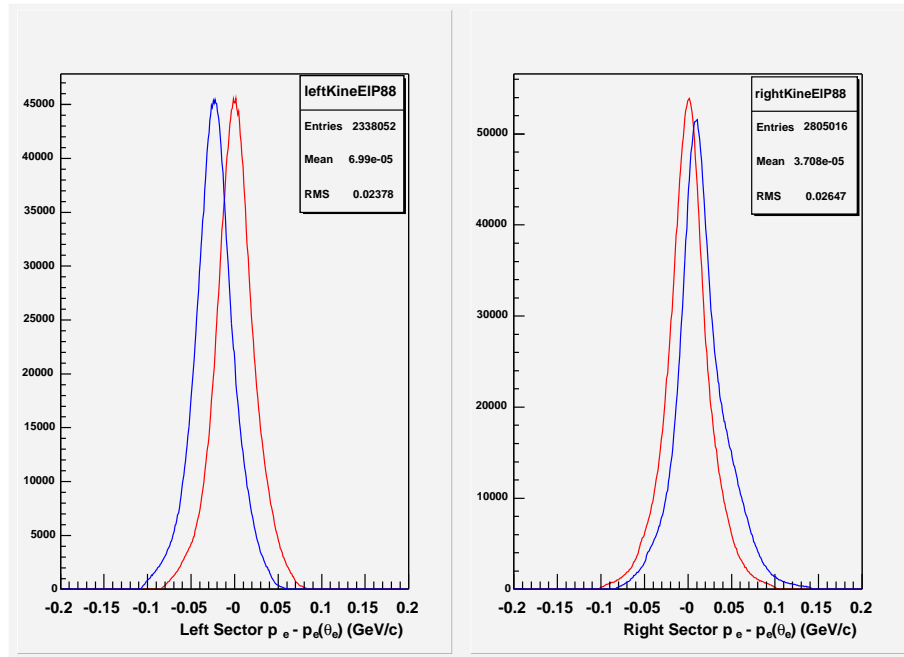


Figure 5-12: Difference between p_e and p_e as calculated from θ_e before (blue) and after (red) momentum corrections

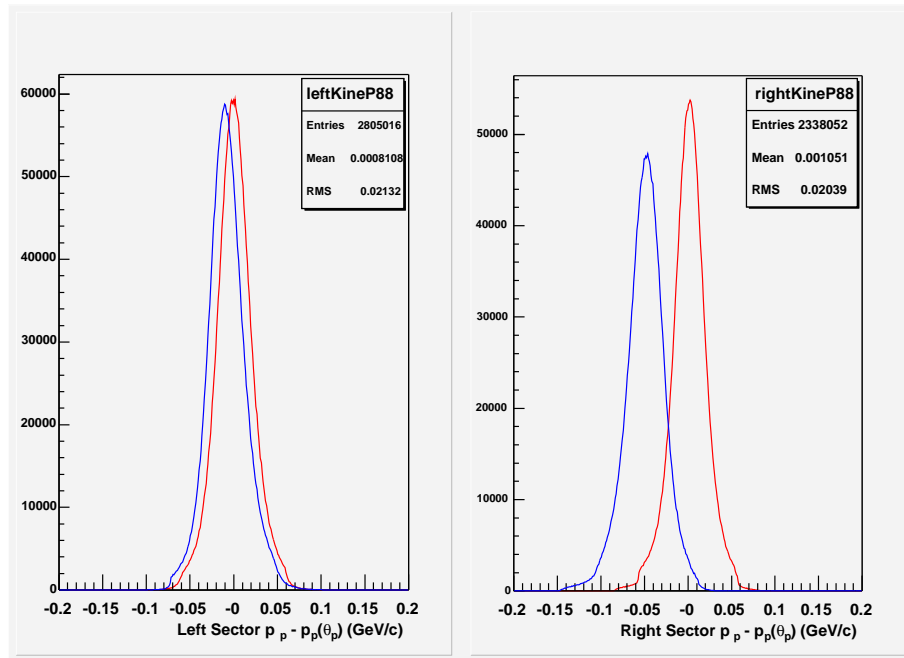


Figure 5-13: Difference between p_p and p_p as calculated from θ_p before (blue) and after (red) momentum corrections

$Q^2 \left[\frac{\text{GeV}}{c} \right]^2$	A_{LEFT}^{ep}	$\delta A_{LEFT} (stat.)$	A_{RIGHT}^{ep}	$\delta A_{RIGHT} (stat.)$
0.162	-0.0836882	0.00143418	-0.102828	0.00148802
0.191	-0.0953499	0.00149727	-0.117898	0.00144562
0.232	-0.1161910	0.00170563	-0.141309	0.00160629
0.282	-0.1386730	0.00202020	-0.170225	0.00195440
0.344	-0.1651270	0.00250757	-0.203938	0.00246249
0.417	-0.1994770	0.00310736	-0.239759	0.00305346
0.500	-0.2269780	0.00390360	-0.273313	0.00382162
0.592	-0.2666590	0.00523568	-0.305286	0.00502808
0.823	-0.3216480	0.01272820	-0.341988	0.01308050

Table 5.6: Unradiated Monte Carlo asymmetries A_{ep} : $\theta_T = 47^\circ$, $P_b P_t = 0.52$. 8M events were generated and reconstructed

that will also help eliminate the Q^2 discrepancy mentioned at the beginning of this section. At the time of writing this thesis, these wire chambers recalibrations are being performed.

Radiative effects are expected to cancel to first order [91] when measuring polariza-

$Q^2 \left[\frac{\text{GeV}}{c} \right]^2$	A_{LEFT}^{ep}	$\delta A_{LEFT} (stat.)$	A_{RIGHT}^{ep}	$\delta A_{RIGHT} (stat.)$
0.162	-0.0852723	0.00166111	-0.102093	0.00170986
0.191	-0.0953024	0.00172442	-0.119402	0.00164554
0.232	-0.1155730	0.00196626	-0.141367	0.00182773
0.282	-0.1414650	0.00230470	-0.167196	0.00224536
0.344	-0.1678950	0.00291635	-0.201464	0.00287755
0.418	-0.1953650	0.00361061	-0.238099	0.00353132
0.500	-0.2400490	0.00440618	-0.269276	0.00435125
0.592	-0.2753690	0.00614202	-0.295319	0.00577062
0.814	-0.3185660	0.01345120	-0.373165	0.01333980

Table 5.7: Radiated Monte Carlo asymmetries A_{ep} : $\theta_T = 47^\circ$, $P_b P_t = 0.52$. 8M events were generated and reconstructed

tion asymmetries by taking ratios of the cross sections. This is indeed confirmed by our

comparison of the unradiated Monte Carlo asymmetries with the radiated Monte Carlo asymmetries. A 2σ cut on the invariant mass W was applied on the radiated Monte Carlo. This cut was used instead of cuts on the five overdetermined wire chamber variables or cuts on BAT timing.

The unradiated Monte Carlo beam-target asymmetries for the left and right BLAST sectors are shown in Table 5.6. The radiated Monte Carlo beam-target asymmetries for the left and right BLAST sectors are shown in Table 5.7. Figure 5-14 shows this comparison in the left and the right sectors of BLAST respectively. Figure 5-15 shows the the quantity $(A_{radiativeMC} - A_{MC})/A_{MC}$ in the two sectors of BLAST. Note that the differences are very small and centered around zero, so the systematic errors caused by radiative effects are negligible in comparison with the other effects described in this section.

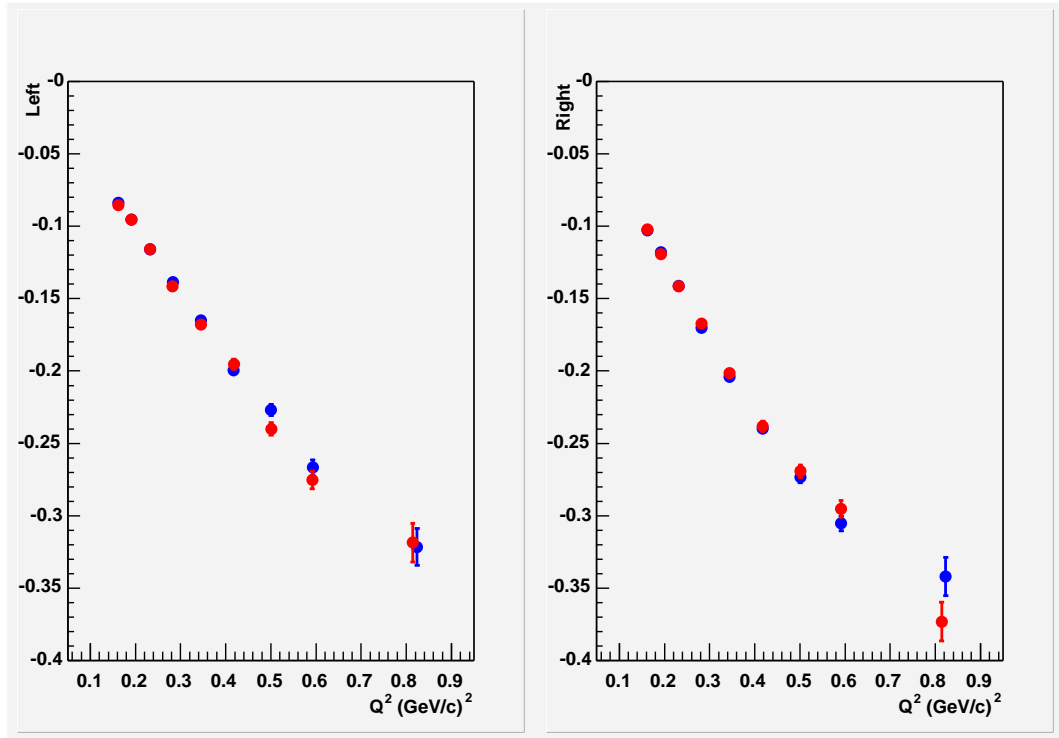


Figure 5-14: Comparison between the unradiated Monte Carlo asymmetries (blue) and the radiated Monte Carlo asymmetries (red)

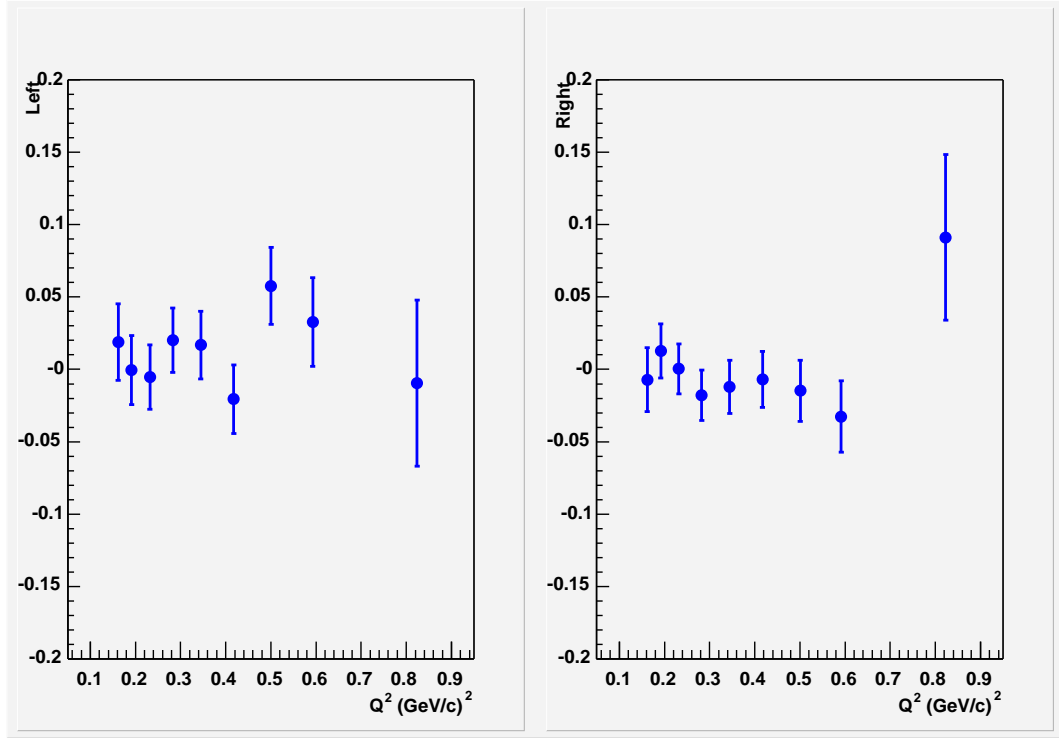


Figure 5-15: $(A_{radiativeMC} - A_{MC})/A_{MC}$

5.4 Results Discussion and Outlook

Figure 5-16 shows the final BLAST results of $\frac{\mu G_E^p}{G_M^p}$ with systematic errors. Figure 5-17 shows the BLAST results of $\frac{\mu G_E^p}{G_M^p}$ with the world polarization data and theoretical models that more closely reproduce these higher Q^2 data obtained at JLab through the Focal Plane Polarimeter method. Our results complement the polarized results from JLab down to $Q^2 = 0.1$ (GeV/c)² with comparable precision.

A small dip is observed in $\frac{\mu G_E^p}{G_M^p}$ for our fourth data point at $Q^2 = 0.282$ (GeV/c)², but it can be argued it is within the statistical uncertainties of the experiment. None of the models predicts such a dip, although there is a somewhat consistent trend in previous data. In Figure 1-3 one can see that Hoehler *et al.* also observe a small dip in the Q^2

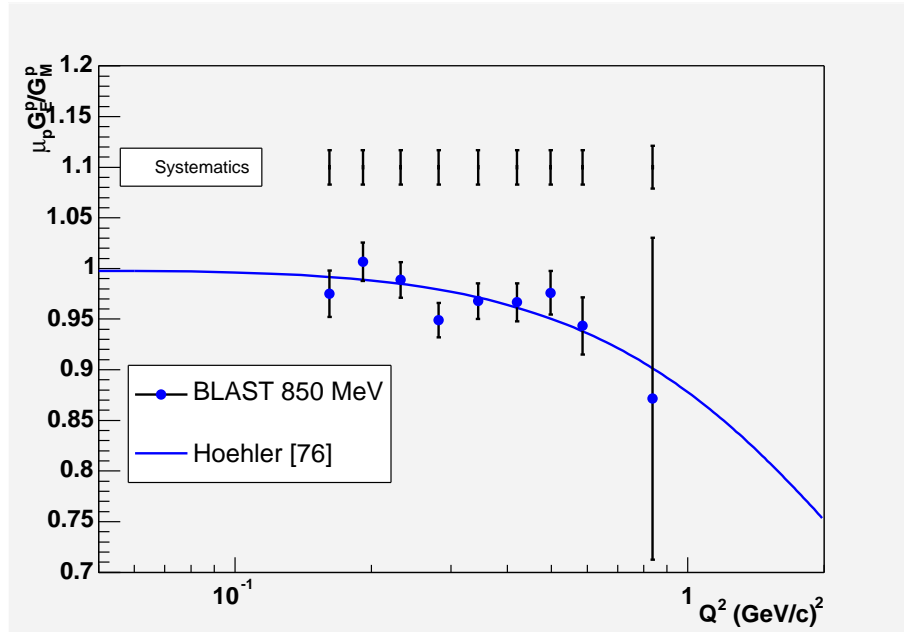


Figure 5-16: The BLAST results of $\frac{\mu_p G_E^p}{G_M^p}$ with systematic errors. The curve is Hoehler's parametrization

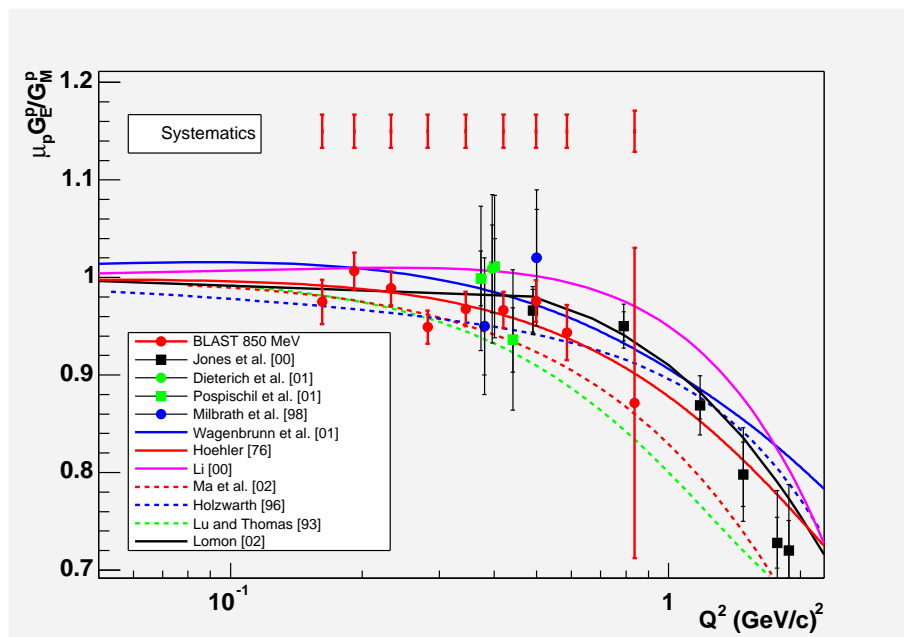


Figure 5-17: The BLAST results of $\frac{\mu_p G_E^p}{G_M^p}$. Also shown are the world's polarization transfer data and models that reproduce these higher Q^2 data obtained at JLab through the Focal Plane Polarimeter method

region between 0.2 and 0.3 (GeV/c)². The same trend seems to show in the polarized data of Gayou *et al.*, as it can be seen in Figure 1-4. The old FPP results from MIT-Bates of Milbrath *et al.* also seem to indicate a dip structure, but they do not extend beyond the dip and their error bars are too large for the magnitude of this effect.

From the theoretical models, the VMD model of Lomon and the dispersion model of Hoehler follow our data very well, with the point form dynamics calculation of Wagenbrunn and the soliton model of Holzwarth being the closest of the CQM models. However, none of these models predicts a dip structure, so it is important to understand the sources of systematic errors and how they might affect our measurement.

The most significant contributions to the systematic errors come from the discrepancy between Q^2 as determined from either the electron or the proton track information. The false asymmetries, background contribution and radiative effects are all very small and expected to cancel out in first order in the super ratio method so they would not explain the dip. The same is true for the systematic error contributions coming from the target spin angle. An error in the estimation of the spin angle would move all points up or down, acting like an overall normalization uncertainty.

So the only systematic error which could cause the dip is the determination of Q^2 , as non-uniform, sector-dependent deviations could explain such a structure. The difference between the determinations using the electron or the proton track information provides an estimate of this source of systematic errors.

The Q^2 region of the possible dip structure in $\frac{\mu G_E^p}{G_M^p}$ in both unpolarized and polarized older data as described above might be related to the ansatz of Friederich and Walcher [29] who based their fit shown in Figure 1-5 on a conjecture motivated by a bump in the electric form factor of the neutron. The BLAST data on G_E^n [75] measured in the deuterium program complementary to our hydrogen experiment agree well with their conjecture as seen in Figure 5-18 and seem to show the contribution of the nucleon's pion cloud.

The pion cloud was used even before the realization of the quark-gluon structure of

the nucleon in order to explain the Yukawa interaction between the nucleons. After early pure quark models of the nucleon like the MIT bag, the pion cloud was introduced in the “cloudy bag” models in order to preserve chiral symmetry at the nucleon surface [29]. The chiral perturbation theory has shown through many experimental tests that, besides the quarks and gluons, the pion is an important constituent of the nucleon [29]. The simple ansatz of Friederich and Walcher needs a more thorough theoretical discussion that could include next-to-leading contributions like the pion-Delta component in the nucleon wave function, which was already included by Mergell [57] in a dispersion analysis enhancing Hoehler’s model.

It would be interesting to extend polarization measurements on the proton to lower

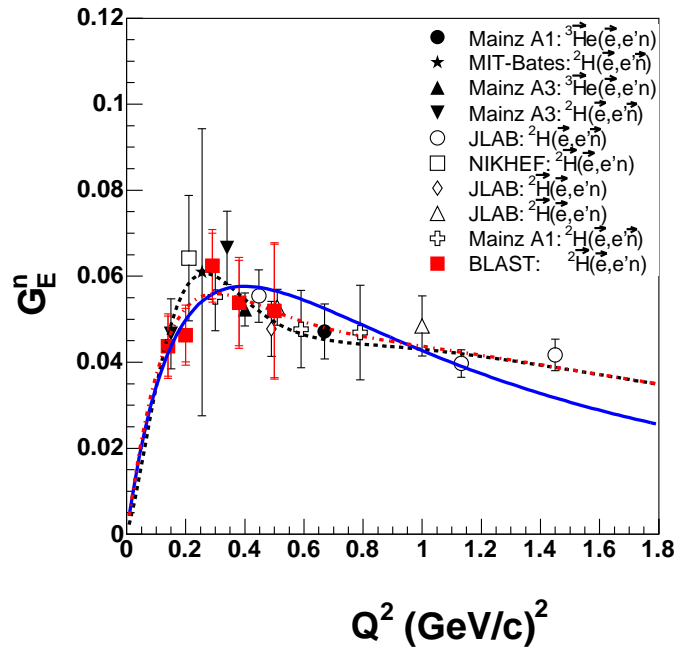


Figure 5-18: The BLAST results of G_E^n . The solid blue curve is Platchkov’s fit, the dashed black and red curves are Friederich and Walcher’s fit without and with BLAST data on G_E^n respectively

Q^2 . The proposal by Gao and Calarco [92] for a precision measurement of the proton charge radius was conditionally approved with high priority but could not be performed before the BLAST project ran out of funding. There is also a deferred proposal by Zheng, Calarco *et al.* [37] to measure $\mu G_E^p/G_M^p$ from elastic $\vec{p}(\vec{e}, e'p)$ at JLab in Hall C which would allow a direct comparison between the FPP method and the double-polarization method at higher Q^2 .

For our current experiment, it is important to resolve the Q^2 discrepancy as this is the only possible source of error that could create the dip structure. An absolute wire chamber calibration is essential in order to do this and it is being performed at the time of writing this thesis. All available information from the detector surveys, cosmic ray and experimental ep elastic data taking is being used in order to get a consistent calibration of the wire chambers.

As of now, preparations are under way to redo the target holding field mapping to a precision of 0.1° by a new method based on a compass principle. Together with the wire chambers calibrations, this will greatly reduce our systematic errors.

After the above mentioned recalibrations, the BLAST reconstruction code will produce a more accurate data summary tape, which will also include better timing calibrations for the BATs (already in place as of now, but not included in the DST used for this thesis), resulting in an improved event selection when compared to the present work. In the best case scenario, our statistics could be improved by a factor of four in the high Q^2 region of the BATs by eliminating the need for Čerenkov cuts which drastically reduce our number of events in this region. This could result in a factor of two reduction of the statistical error bars for our last data point at $Q^2 = 0.836 \text{ (GeV/c)}^2$.

Our current experiment has shown that double-spin asymmetries are an effective method for unraveling the mysteries of the nucleon structure. Our results show improvements in the determination of the proton form factor ratio, with a clear reduction in uncertainties even in a region where unpolarized experiments are still effective. With the likely dip

structure still waiting to be confirmed after the present recalibrations, these results could soon be tested against new models and calculations of lattice QCD.

LIST OF REFERENCES

- [1] H. Gao. *nucl-ex/0301002*, 2003.
- [2] R. Hofstadter. *Rev. Mod. Phys.*, 28:214, 1956.
- [3] R. Hofstadter and R.W. McAllister. *Phys. Rev.*, 98:217–218, 1955.
- [4] R. Frisch; O.Stern. *Z. Phys.*, 85:4, 1933.
- [5] M.K. Jones et al. *Phys. Rev. Lett.*, 84:1398–1402, 2000.
- [6] O. Gayou et al. *Phys. Rev. Lett.*, 88:092301, 2002.
- [7] M.N. Rosenbluth. *Phys. Rev.*, 79:615–619, 1950.
- [8] W. Albrecht et al. *Phys. Rev. Lett.*, 17:1192, 1966.
- [9] L. E. Price et al. *Phys. Rev. D*, 4:45, 1971.
- [10] P. N. Kirk et al. *Phys. Rev. D*, 8:63, 1973.
- [11] I.J. Murphy et al. *Phys. Rev. C*, 9:2444, 1974.
- [12] F. Borkowski et al. *Nucl. Phys.*, A222:269, 1974.
- [13] G.G. Simon et al. *Nucl. Phys.*, A333:381, 1980.
- [14] L. Andivahis et al. *Phys. Rev. D*, 50:5491, 1994.
- [15] I. A. Qattan et al. *nucl-ex/0410010*, 2004.
- [16] R. C. Walker et al. *Phys. Rev. D*, 49:5671, 1994.
- [17] C. Berger et al. *Phys. Lett. B*, 35:87, 1971.
- [18] W. Bartel et al. *Nucl. Phys. B*, 58:429, 1973.
- [19] T. Janssens et al. *Phys. Rev.*, 142:922, 1966.
- [20] J. Litt et al. *Phys. Lett. B*, 31:40, 1970.
- [21] B. D. Milbrath et al. *Phys. Rev. Lett.*, 80:452–455, 1998.
- [22] T. Popischil et al. *Eur. Phys. J*, page 125, 2001.
- [23] S. Dieterich et al. *Phys. Lett.*, page 47, 2001.
- [24] J. Arrington. *Phys. Rev. C*, 68:034325, 2003.

- [25] J. Arrington. *Phys. Rev. C*, 69:022201, 2004.
- [26] D. Dutta et al. *Phys. Rev. C*, 68:064603, 2003.
- [27] M. E. Christy et al. *Phys. Rev. C*, 70:015206, 2004.
- [28] J. J. Kelly. *Phys. Rev. C*, 70:068202, 2004.
- [29] J. Friedrich and T. Walcher. *hep-ph/0303054*, 2003.
- [30] L. W. Mo and Y.-S. Tsai. *Rev. Mod. Phys.*, 41:205, 1969.
- [31] P. A. M. Guichon and M. Vanderhaeghen. *Phys. Rev. Lett.*, 91:142303, 2003.
- [32] W. Melnitchouk P. G. Blunden and J. A. Tijon. *Phys. Rev. Lett.*, 91:142304, 2003.
- [33] Y. C. Chen et al. *Phys. Rev. Lett.*, 93:122301, 2004.
- [34] F. E. Maas et al. *Phys. Rev. Lett.*, 93:022002, 2004.
- [35] E. J. Beise et al. *nucl-ex/0412054*, 2005.
- [36] D. S. Armstrong et al. *Phys. Rev. Lett.*, 95:092001, 2005.
- [37] J. Calarco et al. X. Zheng. Measurements of g_E^p/g_M^p using elastic $\vec{p}(\vec{e}, e'p)$ up to $q^2 = 5.6$ (gev/c)², tech. rep., tjnaf, experiment proposal pr-04-111, 2004.
- [38] T.W. Donnelly and A.S. Raskin. *Ann. Phys.*, 169:247, 1986.
- [39] X. Ji. *Phys. Rev. Lett.*, 78:610, 1997.
- [40] A. V. Radyushkin. *Phys. Rev. D.*, 56:5524, 1997.
- [41] M. Breidenbach et al. E. D. Bloom et al. *Phys. Rev. Lett.*, 23:930–934, 1969.
- [42] R.P. Feynman. *Phys. Rev. Lett.*, 23:1415–1417, 1969.
- [43] J. D. Bjorken and E. A. Paschos. *Phys. Rev.*, 185:1975–1982, 1969.
- [44] B. Povh et al. *Particles and Nuclei : An Introduction to the Physical Concepts*. Springer Verlag, 1999.
- [45] S.J. Brodsky and G.R. Farrar. *Phys. Rev. D*, 11:1309–1330, 1975.
- [46] G. P. Lepage and S. J. Brodsky. *Phys. Lett. B*, 87:359, 1979.
- [47] X.-D. Ji A. V. Belitsky and F. Yuan. *Phys. Rev. D*, 69:074014, 2004.
- [48] J. P. Ralston and P. Jain. *hep-ph/0302043*, 2004.
- [49] G. A. Miller H. H. Matevosyan and A. Thomas. *nucl-th/0501044*, 2005.
- [50] J. D. Ashley et al. *hep-lat/0308024*, 2003.

- [51] G. V. Dunne et al. *hep-th/0110155*, 2002.
- [52] F. Iachello et al. *Phys. Lett. B*, 43:191, 1973.
- [53] M. Gari and W. Krumpelmann. *Z. Phys. A*, 322:689, 1985.
- [54] E. L. Lomon. *Phys. Rev. C*, 64:035204, 2001.
- [55] E. L. Lomon. *Phys. Rev. C*, 66:045501, 2002.
- [56] G. Hohler et al. *Nuclear Physics B*, 114:505, 1976.
- [57] P. Mergell et al. *hep-ph/9506375*, 1996.
- [58] H. W. Hammer et al. *hep-ph/9604294*, 1996.
- [59] A. P. Bakulev et al. *hep-ph/0005085*, 2000.
- [60] B. Kubis et al. *hep-ph/0007056*, 2001.
- [61] O. Gayou. PhD thesis, Univ. Blaise Pascal, 2002.
- [62] S. N. Yang D. H. Lu and A. W. Thomas. *Nucl. Phys. A*, 684:296, 2001.
- [63] B. K. Jennings M. R. Frank and G. A. Miller. *Phys. Rev. C*, 54:920–935, 1996.
- [64] G. A. Miller. *nucl-th/0207007*, 2002.
- [65] F. Cardarelli and S. Simula. *Phys. Rev. C*, 62:065201, 2000.
- [66] B.-Q. Ma et al. *hep-ph/0202015*, 2001.
- [67] R. F. Wagenbrunn et al. *nucl-th/0010048*, 2001.
- [68] B.-A. Li et al. *hep-ph/0004142*, 2001.
- [69] G. Holzwarth. *hep-ph/9606336*, 1996.
- [70] <http://mitbates.lns.mit.edu/bates/control/main> MIT-Bates Website, 2004.
- [71] The BLAST Collaboration, 1997.
- [72] W.A. Franklin. *BLAST Compton Polarimeter Website*, 2003.
- [73] Taylan Akdogan. (private communication), 2005.
- [74] Hauke Kolster. Conceptual design report for the atomic beam source of the blast polarized deuterium target, 2002.
- [75] V. Ziskin. PhD thesis, Massachusetts Institute of Technology, 2005.
- [76] K. Dow et al. *Magnetic Measurements of the BLAST Spectrometer*, 2005.
- [77] K. Dow. (private communication), 2005.

- [78] Bicron Saint-Gobain Detectors. Bc-408: Premium plastic scintillator, 2003.
- [79] P. Karpius. PhD thesis, University of New Hampshire, 2005.
- [80] R.T. Giles. *Nuclear Instruments and Methods in Physics Research*, A252, 1986.
- [81] A. Sindile. The time of flight scintillators for the blast detector - presented at the first joint meeting of the nuclear physicists of the american and japanese physical societies, 2001.
- [82] A. Sindile. The blast mysql database - presented at mit-bates for the blast collaboration, 2002.
- [83] C. Crawford. PhD thesis, Massachusetts Institute of Technology, 2005.
- [84] A. Maschinot. PhD thesis, Massachusetts Institute of Technology, 2005.
- [85] D. Hasell. Blast drift chamber report, the blast collaboration, 1998.
- [86] Frederick Tong uk Lee. (private communication), 2005.
- [87] O. Filoti. *The Čerenkov Counters for the BLAST Detectors*, APS-DNP Fall Meeting, Chicago, 2004.
- [88] R. Elmasri. *Fundamentals of Database Systems*. Addison-Wesley, 2000.
- [89] A. Sindile. Physics and computing for blast - presented at the fermilab computing division, 2005.
- [90] <http://root.cern.ch/root/> ROOT Website, 2005.
- [91] N. Merenkov A. Afanasev, I. Akushevich. *JETP*, 98:403–416, 2003.
- [92] J. Calarco H. Gao. Precision measurement of the proton charge radius, experiment proposal 00-02, 2000.

APPENDIX

Rosenbluth Cross Section and Proton Form Factors

The S-matrix that describes the transition from initial state i to final state f in the process of electron scattering at a fixed Coulomb potential is:

$$S_{fi} = -ie \int d^4x \bar{\psi}_f(x) \not{A} \Psi_i(x) \quad (f \neq i) \quad (\text{A-1})$$

where $e < 0$ is the charge of the electron and $\not{A} = \gamma^\mu A_\mu$ with γ^μ being the Dirac matrices and A_μ being the four-vector potential. In the lowest order of perturbation theory, $\Psi_i(x)$ is the incoming plane wave $\psi_i(x)$ of an electron with momentum p_i and spin s_i :

$$\psi_i(x) = \sqrt{\frac{m_0}{E_i V}} u(p_i, s_i) e^{-ip_i x} \quad (\text{A-2})$$

where V is the normalization volume, i.e. ψ_i is normalized to probability 1 in a box of volume V . Similarly,

$$\bar{\psi}_f(x) = \sqrt{\frac{m_0}{E_f V}} \bar{u}(p_f, s_f) e^{ip_f x} \quad (\text{A-3})$$

In the above formulas, $u(p_i, s_i)$ and $u(p_f, s_f)$ are the Dirac spinors and $\bar{u}(p_f, s_f) = u^\dagger(p_f, s_f) \gamma^0$. Since the process is Coulomb scattering:

$$A_0(x) = \frac{-Ze}{|x|}, \quad \vec{\mathbf{A}}(x) = 0. \quad (\text{A-4})$$

From Fermi's second golden rule, the reaction rate W per target particle and per beam particle is:

$$W = \frac{2\pi}{\hbar} |S_{fi}|^2 \rho(E_f) \quad (\text{A-5})$$

where $\rho(E_f)$ is the density of final states. We also know

$$W = \frac{\sigma v_a}{V} \quad (\text{A-6})$$

where v_a is the initial velocity of the beam particles and V is the volume occupied by them. Putting together the above we get the cross section

$$\sigma = \frac{2\pi}{\hbar v_a} |S_{fi}|^2 \rho(E_f) V \quad (\text{A-7})$$

For the simple process of Coulomb scattering, using the S-matrix formula we get the unpolarized differential cross section by averaging over the initial polarizations s_i and summing over the final polarizations s_f :

$$\frac{d\bar{\sigma}}{d\Omega} = \frac{4Z^2 \alpha^2 m_0^2}{q^4} \frac{1}{2} \sum_{s_f, s_i} |\bar{u}(p_f, s_f) \gamma^0 u(p_i, s_i)|^2 \quad (\text{A-8})$$

The above formula can also be written using matrix traces as

$$\frac{d\bar{\sigma}}{d\Omega} = \frac{4Z^2\alpha^2 m_0^2}{2q^4} \text{Tr} \left(\gamma^0 \frac{\not{p}_i + m_0}{2m_0} \gamma^0 \frac{\not{p}_f + m_0}{2m_0} \right) \quad (\text{A-9})$$

which yields, in the extreme relativistic limit (ERL)

$$\frac{d\bar{\sigma}}{d\Omega} = \frac{Z^2\alpha^2 \cos^2(\theta/2)}{4E_i^2 \sin^4(\theta/2)} \quad (\text{A-10})$$

which is just the Mott cross section, without the recoil factor (this makes sense since we have considered scattering on a Coulomb potential, not a target that might have recoil). If, instead of a Coulomb potential, we consider electron scattering off a structureless Dirac (spin-1/2) particle, we expect the above result to be different, since now recoil effects are present. In such a case, we need to calculate first the four-potential produced by the Dirac proton. If we denote the proton current by $J^\mu(x)$, the four-potential is given in the Lorentz gauge ($\partial_\mu A^\mu = 0$) by:

$$\square A^\mu(x) = 4\pi J^\mu(x) \quad (\text{A-11})$$

With the help of the photon propagator

$$D_F(x-y) = \int \frac{d^4q}{(2\pi)^4} \exp[-iq(x-y)] \left(\frac{-4\pi}{q^2 + i\epsilon} \right) \quad (\text{A-12})$$

which in the above formula is carefully treated for the singularity at $q^2 = 0$ and is defined as any Green's function by

$$\square D_F(x-y) = 4\pi \delta^4(x-y) \quad (\text{A-13})$$

we can write

$$A^\mu(x) = \int d^4y D_f(x-y) J^\mu(y) \quad (\text{A-14})$$

and the S-matrix element defining the transition in the process of electron scattering off a Dirac proton becomes

$$S_{fi} = -i \int d^4x d^4y [e\bar{\psi}_f(x)\gamma_\mu\psi_i(x)] D_f(x-y) J^\mu(y) \quad (\text{A-15})$$

The term inside the brackets represents the current of the electron. It is a matrix element of the current operator between an initial and final state and so it is called a *transition current*. Since the electron and proton play similar roles in the scattering process, the proton's current has to be of the same form as the electron's. So we can make the replacement

$$J^\mu(y) \rightarrow J_{fi}^\mu(y) = e_p \bar{\psi}_f^p(y) \gamma^\mu \psi_i^p(y) \quad (\text{A-16})$$

where

$$\psi_i^p(y) = \sqrt{\frac{M_0}{E_i^p V}} u(P_i, S_i) e^{-iP_i y} \quad (\text{A-17})$$

and

$$\psi_f^p(y) = \sqrt{\frac{M_0}{E_f^p V}} u(P_f, S_f) e^{-iP_f y} \quad (\text{A-18})$$

are the free initial and final states of the proton. Using the photon propagator and proton current formulas, we get the S-matrix element and so we arrive at the following result for the averaged squared matrix element:

$$|S_{fi}^-|^2 = \frac{1}{4} \sum_{S_f, S_i, s_f, s_i} |\bar{u}(p_f, s_f) \gamma^\mu u(p_i, s_i) \frac{e e_p (4\pi)}{q^2 + i\epsilon} \bar{u}(P_f, S_f) \gamma_\mu u(P_i, S_i)|^2 \quad (\text{A-19})$$

which can also be expressed using matrix traces as

$$|S_{fi}^-|^2 = \frac{1}{4} \frac{e^2 e_p^2 (4\pi)^2}{(q^2)^2} \text{Tr} \left(\frac{\not{p}_f + m_0}{2m_0} \gamma^\mu \frac{\not{p}_i + m_0}{2m_0} \gamma^\nu \right) \text{Tr} \left(\frac{\not{P}_f + M_0}{2M_0} \gamma_\mu \frac{\not{P}_i + M_0}{2M_0} \gamma_\nu \right) \quad (\text{A-20})$$

The above formula is often abbreviated as

$$|S_{fi}^-|^2 = \frac{e^2 e_p^2 (4\pi)^2}{(q^2)^2} L^{\mu\nu} H_{\mu\nu} \quad (\text{A-21})$$

where $L^{\mu\nu}$ is the *lepton* (i.e. electron) *tensor* and $H_{\mu\nu}$ is the *hadron* (i.e. proton) *tensor*:

$$L^{\mu\nu} = \frac{1}{2} \sum_{s_f, s_i} \bar{u}(p_f, s_f) \gamma^\mu u(p_i, s_i) \bar{u}(p_i, s_i) \gamma^\nu u(p_f, s_f) = \frac{1}{2} \text{Tr} \left(\frac{\not{p}_f + m_0}{2m_0} \gamma^\mu \frac{\not{p}_i + m_0}{2m_0} \gamma^\nu \right) \quad (\text{A-22})$$

and similarly

$$H_{\mu\nu} = \frac{1}{2} \text{Tr} \left(\frac{\not{P}_f + M_0}{2M_0} \gamma_\mu \frac{\not{P}_i + M_0}{2M_0} \gamma_\nu \right) \quad (\text{A-23})$$

In the extreme relativistic limit (ERL), using the above averaged squared matrix element, we obtain for the cross section

$$\frac{d\bar{\sigma}}{d\Omega} = \frac{\alpha^2}{4E_i^2} \frac{1}{\sin^4(\frac{\theta}{2})} \frac{\cos^2(\frac{\theta}{2}) - \frac{q^2}{2M_0^2} \sin^2(\frac{\theta}{2})}{1 + \frac{2E_i}{M_0} \sin^2(\frac{\theta}{2})} \quad (\text{A-24})$$

The above formula describes the cross section under the assumption that the proton behaves like a heavy electron with mass M_0 . In order to provide a realistic description of electron-proton scattering, we need to consider the internal structure and anomalous magnetic moment of the proton. To that end, we need to replace the transition current with the more general bilinear expression

$$\bar{u}(P_f) \gamma_\mu u(P_i) \rightarrow \bar{u}(P_f) \Gamma_\mu(P_f, P_i) u(P_i) \quad (\text{A-25})$$

The most general expression for a transition current that fulfills the conditions of Lorentz covariance, Hermiticity and gauge invariance can be written as

$$\bar{u}(P_f)\Gamma_\mu(P_f, P_i)u(P_i) = \bar{u}(P_f)\left(\gamma_\mu F_1(q^2) + i\frac{1}{2M_0}F_2(q^2)q^\nu\sigma_{\mu\nu}\right)u(P_i) \quad (\text{A-26})$$

where $q = P_f - P_i$ is the momentum transfer, $\sigma_{\mu\nu} = \frac{i}{2}[\gamma_\mu, \gamma_\nu]$, and $F_1(q^2), F_2(q^2)$ are unspecified real functions (“form factors”). Using the Gordon decomposition

$$\bar{u}\gamma_\mu u = \frac{1}{2M_0}(P_f + P_i)_\mu\bar{u}u + \frac{i}{2M_0}q^\nu\bar{u}\sigma_{\mu\nu}u \quad (\text{A-27})$$

we can rewrite the vertex function

$$\Gamma_\mu(P_f, P_i) = \gamma_\mu(F_1(q^2) + F_2(q^2)) - \frac{1}{2M_0}(P_f + P_i)_\mu F_2(q^2) \quad (\text{A-28})$$

and the squared spin-averaged transition matrix element becomes

$$|S_{fi}^-|^2 = \frac{1}{4} \sum_{spin} |\bar{u}(p_f, s_f)\gamma^\mu u(p_i, s_i) \frac{4\pi e e_p}{q^2} \bar{u}(P_f, S_f) \left[\gamma_\mu(F_1 + F_2) - \frac{1}{2M_0}(P_f + P_i)_\mu F_2 \right] u(P_i, S_i)|^2 \quad (\text{A-29})$$

which can be written as

$$|S_{fi}^-|^2 = \frac{e^2 e_p^2 (4\pi)^2}{(q^2)^2} L^{\mu\nu} H_{\mu\nu} \quad (\text{A-30})$$

where $L^{\mu\nu}$ is the *lepton tensor* and $H_{\mu\nu}$ is the *hadron tensor*:

$$L^{\mu\nu} = \frac{1}{2} Tr \left(\frac{\not{p}_f + m_0}{2m_0} \gamma^\mu \frac{\not{p}_i + m_0}{2m_0} \gamma^\nu \right) \quad (\text{A-31})$$

and

$$H_{\mu\nu} = \frac{1}{4M_0^2} \frac{1}{2} Tr K \quad (\text{A-32})$$

where the K matrix is:

$$K = \left[(\not{P}^i + M_0) \left(\gamma_\mu(F_1 + F_2) - \frac{F_2}{2M_0}(P_\mu^f + P_\mu^i) \right) (\not{P}^f + M_0) \left(\gamma_\nu(F_1 + F_2) - \frac{F_2}{2M_0}(P_\nu^f + P_\nu^i) \right) \right] \quad (\text{A-33})$$

Using the above leptonic and hadronic tensors, we obtain the spin-averaged cross section

$$\frac{d\bar{\sigma}}{d\Omega} = \frac{e^2 e_p^2}{4E_i^2 \sin^4\left(\frac{\theta}{2}\right) \left[1 + \frac{2E_i}{M_0} \sin^2\left(\frac{\theta}{2}\right)\right]} \left[\left(F_1^2 - \frac{q^2}{4M_0^2} F_2^2\right) \cos^2\left(\frac{\theta}{2}\right) - (F_1 + F_2)^2 \frac{q^2}{2M_0^2} \sin^2\left(\frac{\theta}{2}\right) \right] \quad (\text{A-34})$$

The above result is known as *Rosenbluth's formula* [7]. If instead of the functions $F_1(q^2)$ and $F_2(q^2)$ we introduce the so-called electric and magnetic “Sachs form factors”

$$G_E(q^2) = F_1(q^2) + \frac{q^2}{4M_0^2} F_2(q^2) \quad (\text{A-35})$$

and

$$G_M(q^2) = F_1(q^2) + F_2(q^2) \quad (\text{A-36})$$

then Rosenbluth's formula becomes

$$\left(\frac{d\bar{\sigma}}{d\Omega}\right)_{ep \rightarrow ep} = \left(\frac{d\bar{\sigma}}{d\Omega}\right)_{Mott} \left(\frac{G_E^2 + \tau G_M^2}{1 + \tau} + 2\tau G_M^2 \tan^2(\theta/2)\right) \quad (\text{A-37})$$

where $\tau = -q^2/4M_0^2 > 0$. The measured Q^2 -dependence of the form factors gives us information about the radial charge and magnetic distributions. The limiting case $Q^2 \rightarrow 0$ is particularly important. In this case G_E coincides with the electric charge of the target normalized to the elementary charge e and G_M is equal to the magnetic moment μ of the target, normalized to the nuclear magneton. The limiting values are:

$$G_E^p(Q^2 = 0) = 1 \quad (\text{A-38})$$

$$G_M^p(Q^2 = 0) \simeq 2.79 \quad (\text{A-39})$$